FUNCTIONAL CHARACTERIZATION AND SURFACE MAPPING OF FRATAXIN (FXN) INTERACTIONS WITH THE FE-S CLUSTER ASSEMBLY COMPLEX

A Thesis

by

MELISSA THORSTAD

Submitted to the Office of Graduate Studies of
Texas A&M University
in partial fulfillment of the requirements for the degree of

MASTER OF SCIENCE

Chair of Committee,	David P. Barondeau
Committee Members,	Marcetta Y. Darensbourg
	Abraham Clearfield
	James C. Sacchettini
Head of Department,	David H. Russell

August 2013

Major Subject: Chemistry

ABSTRACT

In 1996, scientists discovered a connection between the gene for the human
protein frataxin (FXN) and the neurodegenerative disease Friedreich's ataxia (FRDA).
Decreased FXN levels result in a variety of aberrant phenotypes including loss of
activity for iron-sulfur containing enzymes, mitochondrial iron accumulation, and
susceptibility to oxidative stress. These symptoms are the primary focus of current
therapeutic efforts. In contrast our group is pursuing an alternate strategy of first
defining FXN function at a molecular level then using this information to identify small
molecule functional replacements. Recently, our group has discovered that FXN
functions as an allosteric activator for the human Fe-S cluster assembly complex. The
work presented here helps to further define molecular details of FXN activation and
explain how FRDA missense mutants are functionally compromised. First, the FRDA
missense mutants L182H and L182F were investigated. Unlike other characterized
FRDA missense mutants, the L182F variant was not compromised in its ability to bind
and activate the Fe-S assembly complex. The L182H variant exhibited an altered
circular dichroism signature; suggesting a change in secondary structure relative to
native FXN, and rapidly degraded. Together these studies suggest that L182 variants are
less stable than native FXN and are likely prone to degradation in FRDA patients.
Second, as a regulatory role of FXN suggests that its function is likely controlled by
environmental stimuli, different maturation forms of FXN as well as post-translational
modification mimics were tested as mechanisms to control FXN regulation. Here

experiments were designed to test if a larger polypeptide form of FXN represents a functional form of the protein. Kinetic and analytical ultracentrifugation studies revealed a complex heterogeneous mixture of species some of which can activate the Fe-S assembly complex. A previously identified acetylation site was also tested using mutants that mimic acetylation. These mutants had little effect on the ability of FXN to bind and activate the assembly complex. Third, mutagenesis experiments were designed in which the FXN surface residues were replaced with alanine and the resulting variants were tested in binding and activity assays. These experiments revealed a localized "hot-spot" on the surface of FXN that suggests small cyclic peptide mimics might be able to replace FXN and function as FRDA therapeutics. Unexpectedly, one of the FXN variants exhibited significantly tighter binding and could have relevance for therapeutic development.

DEDICATION

I would like to thank my undergraduate chemistry professors and mentors who ignited my interest in chemistry, and inspired and supported my pursuits. Without your guidance, I would never have come this far or felt the support that the scientific community has to offer its members.

Over the course of my life I have been blessed with a loving and supportive family and loyal friends. This work is dedicated to each of them, for the specific roles they have played in my life and their never failing faith in me.

ACKNOWLEDGEMENTS

NOMENCLATURE

DTT   Dithiothreitol

E. coli   *Escherichia coli*

EXAFS   Extended X-ray absorption fine structure spectroscopy

FRDA   Friederich's Ataxia

FXN   Frataxin (also referred to as Fxn, Yfh1 (yeast frataxin), and CyaY (*E. coli* frataxin)

HEPES   N-2-hydroxyethylpiperazine-N'-2-ethanesulfonic acid

IPTG   Isopropyl β-D-thiogalactopyranoside

ISC   Iron sulfur cluster system

ISCU   Human scaffold protein (also referred to as Isu2 and ISCU2)

ISD11   Auxiliary protein to the human cysteine desulfurase

NFS1   Human cysteine desulfurase (also referred to as Nfs1)

PAGE   Polyacrylamide gel electrophoresis

PLP   Pyridoxal-5'-phosphate

ROS   Reactive oxygen species

SD   Human NFS1-ISD11 protein complex

SDU   Human NFS1-ISD11-ISCU protein complex

SDUF   Human NFS1-ISD11-ISCU-FXN protein complex

Tris   Tris(hydroxymethyl) aminomethane

TABLE OF CONTENTS

LIST OF FIGURES

LIST OF TABLES

CHAPTER I

INTRODUCTION

As suggested by Wächtershäuser iron-sulfur (Fe-S) clusters are a vital

component of life and likely played a role in the origins of life on Earth [1]. Despite this

vital role, it was not until the early 1960s that Fe-S clusters were discovered by scientists

[2-7]. Initial characterization of these newly discovered bioinorganic cofactors in the

mid-1960s, paved the way for future investigation of these structures both within the

proteinaceous environment and using synthetic model compounds [2-3, 5, 8]. Today Fe-

S clusters are known to be a vital component of all life forms, with more than 200

enzyme and protein families containing these ubiquitous cofactors [2-4, 6-10].
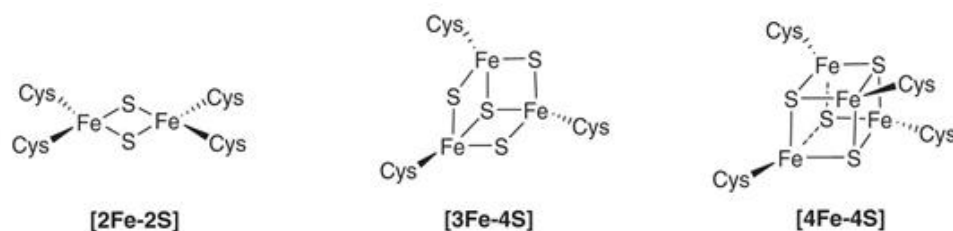
Figure 1-1. Structures of [2Fe-2S], [3Fe-4S], and [4Fe-4S] clusters. Reprinted with
permission from *Nature Chemical Biology*, 2(4): 171-174. Copyright 2006 Nature
Publishing Group.

Although Fe-S clusters exist in several forms, the three most common are the

[2Fe-2S] rhombic cluster, [3Fe-4S] cluster, and [4Fe-4S]cubane cluster (Figure 1-1) [3].

Each of these clusters is characterized by a relatively simple composition of iron

($Fe^{2+/3+}$) and inorganic sulfide (S^{2-}), with a tetrahedral coordination of sulfur atoms to the

iron sites [4-6]. Since both iron and sulfur can exist in multiple redox states they can serve as both electron acceptors and donors [4-5, 7, 10]. This accounts for the wide use of Fe-S clusters in electron transfer; as seen in bacterial ferrodoxins, one of the first Fe-S cluster proteins to be discovered. Although Fe-S clusters are typically coordinated to the protein scaffold through thiolate ligands, such as cysteine sulfurs, other coordination environments, such as histidine, aspartate, glutamine, arginine, serine, and tyrosine are possible [3-5, 8]. The combination of these variable ligation environments with the chemical properties of iron and sulfur allow for fine tuning of the redox potential of individual Fe-S clusters from +300 mV to -500 mV [3, 5]. These seemingly simple, yet vast properties of Fe-S clusters that have afforded them a ubiquitous role in biological systems, with functions ranging from enzyme catalysis, DNA repair, and gene regulation to structural support and environmental sensors of small molecules to iron or sulfur donation and sequestration and delivery agents for cofactor assembly [2-5, 7, 10-11].
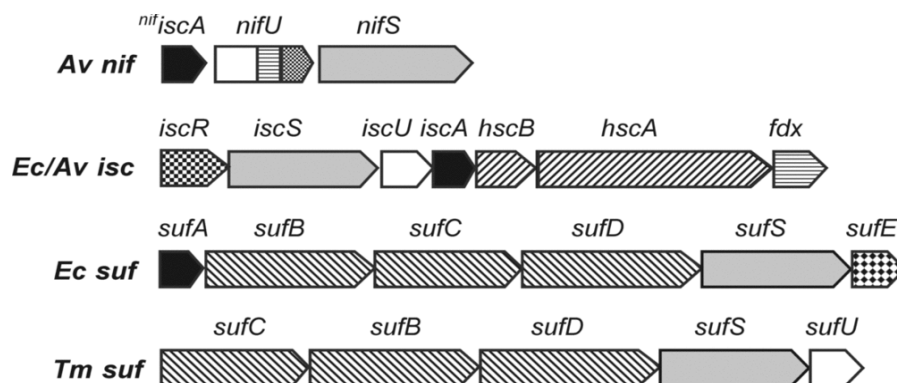
Figure 1-2. Organization of genes in the *NIF*, *ISC*, and *SUF* operons of *Azotobacter vinelandii* (Av), *Escherichia coli* (Ec), and *Thermatoga maritima* (Tm). Reprinted with permission from *Biochemical Society Transactions*, 36: 1112-1119. Copyright 2008 Biochemical Society.

Although Fe-S clusters can freely assemble from ferrous iron and sulfide in solution, the concentrations needed to facilitate such assembly would be detrimental or toxic to biological systems; thus, organisms have developed *in vivo* assembly systems for *de novo* cluster synthesis [4]. The pioneering work by the Dean and Tokumoto groups identified the three Fe-S cluster biosynthesis systems of bacteria (Figure 1-2) [12-14]. The first system to be discovered was the NIF or nitrogen fixation system, which serves primarily in nitrogen-fixing bacteria as the Fe-S cluster assembly system of nitrogenases [5-6, 9]. In contrast the iron sulfur cluster (ISC) and sulfur mobilization (SUF) systems can play a general housekeeping role in the iron sulfur cluster assembly of bacteria, with the SUF system also specialized for conditions of oxidative stress or iron limitation in some organisms. Regardless of the assembly system(s) used, Fe-S cluster biosynthesis can be simplified into three major steps (Figure 1-3) [5-6]:

1. Conversion of cysteine to alanine and sulfane sulfur by a cysteine desulfurase

2. *De novo* cluster assembly on a scaffold protein

3. Transfer of the cluster from the scaffold protein to apoprotein targets

Although some controversy surrounds the mechanism for cluster assembly on the scaffold protein (Figure 1-4), all three assembly systems require multiple protein components to facilitate cluster assembly [5, 15]. Specifically, iron-first and sulfur-first mechanism have been proposed that invoke dimerization of the scaffold protein. The order of substrate addition and oligomeric state of the scaffold protein for cluster synthesis remain unresolved.
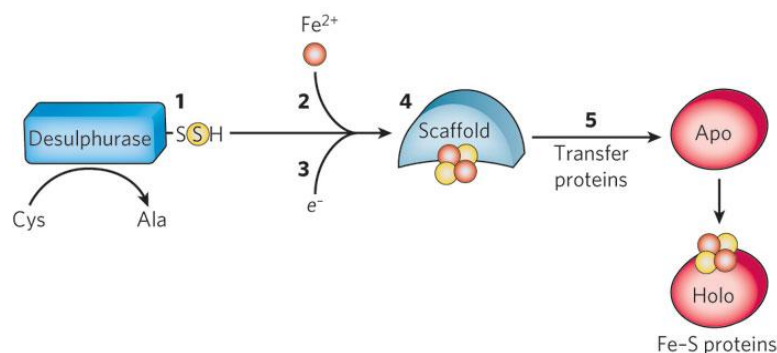
Figure 1-3. General pathway for Fe-S cluster biosynthesis and transfer to apo target proteins. A persulfide forms on the cysteine desulfurase (1), which is then transferred to the scaffold protein along with ferrous iron (2) and electrons (3) to build a cluster on the scaffold protein (4). Once the cluster is assembled on the scaffold protein it can be transferred to apo protein targets (5). Reprinted with permission from *Nature*, 460(7257): 831-838. Copyright 2009 Nature Publishing Group.
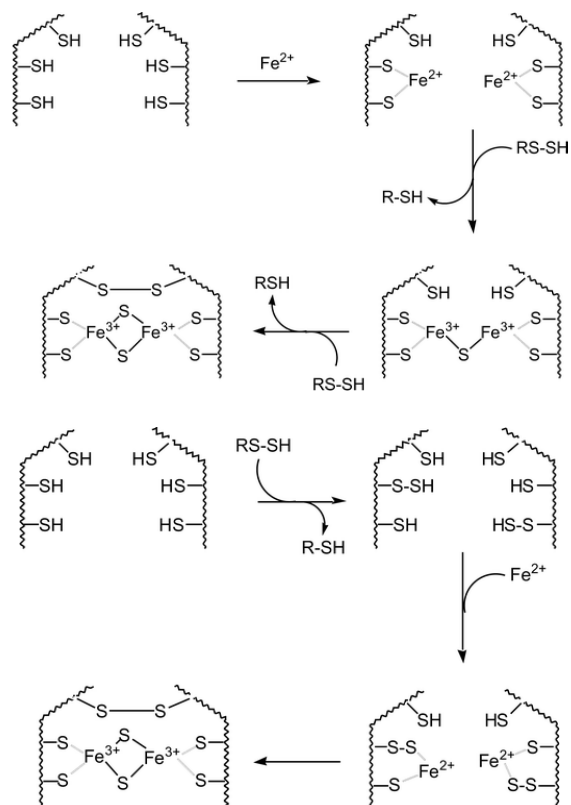
Figure 1-4. The two models, "Fe first, S second" (top) and "S first, Fe second" (bottom), for cluster assembly on the scaffold protein. Reprinted with permission from *Journal of Biological Inorganic Chemistry*, 10(7): 713-721. Copyright 2005 Springer Publishing Group.

While many prokaryotic systems have been shown to contain two of the three Fe-S cluster assembly systems, a mitochondrial form of the ISC system is the primary Fe-S cluster biosynthesis machinery of eukaryotes [6, 12-14]. In prokaryotes, Fe-S cluster assembly components are made in the cytosol and are regulated at the DNA, RNA, and protein levels. In eukaryotes, the genes for Fe-S biosynthesis are nuclear encoded, the polypeptides (typically with cleavable targeting sequences) are synthesized in the cytosol, and the polypeptides are imported into the mitochondria where the targeting sequence is removed to generate the mature proteins [4-6]. The resulting Fe-S biosynthetic protein components, which have strong homology to the bacterial ISC system, serve the roles of sulfur donor, iron donor, electron source, scaffold protein, and accessory/chaperone proteins for cluster transfer. Defects in many of these eukaryotic proteins have been linked to disruption of cellular iron homeostasis, oxidative stress, and human disease (Figure 1-5) [7, 16-18].
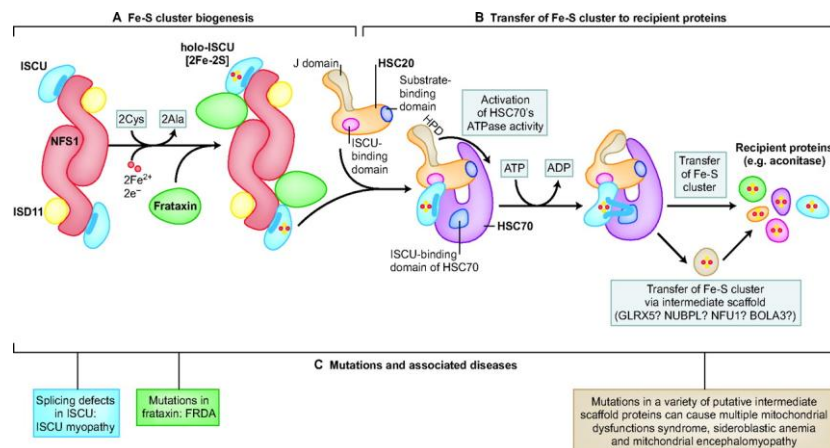
Figure 1-5. Model for iron-sulfur cluster biosynthesis (A) and transfer (B) in the human system, with associated diseases and mutations (C). Reprinted with permission from *Disease Models & Mechanisms*, 5(2): 155-164. Copyright 2012 The Company of Biologists.

In vivo cysteine desulfurase enzymes mobilize sulfur from cysteine, serving as the sulfur source for multiple biological pathways [19]. The sulfur donor for cluster assembly in humans and eukaryotes is a unique 150 kDa complex, termed SD, of the cysteine desulfurase, NFS1, with its 11 kDa auxiliary protein, ISD11, with the sulfur for cluster synthesis being produced through the pyridoxal-5'-phosphate (PLP) dependent cleavage of L-cysteine to L-alanine (Figure 1-6) [5-6, 20-24]. In contrast to bacterial systems where no ISD11 homologue is found, eukaryotes require the presence of this auxiliary protein to facilitate the stability and activity of its cysteine desulfurase and other ISC components. Although the crystal structure of human SD has not been determined, cysteine desulfurase structures of several homologous proteins from prokaryotes have been determined [25-26]. Based on these structures, human NFS1 is expected to be a homodimer composed of two domains, with the larger domain containing the PLP cofactor and active site and the smaller domain containing the catalytic cysteine residue. Each NFS1 monomer is proposed to form the relevant *in vivo* complex by binding one to two ISD11 per NFS1 monomer [27-28]. The mechanism for sulfur release and delivery is initiated by formation of a Schiff base intermediate between the cysteine sulfide atom of the substrate cysteine and the PLP cofactor, followed by nucleophilic attack of the active site cysteine (C328) on the cysteine-PLP ketimine adduct forming a persulfide on C328 and alanine (Figure 1-7) [6, 29].
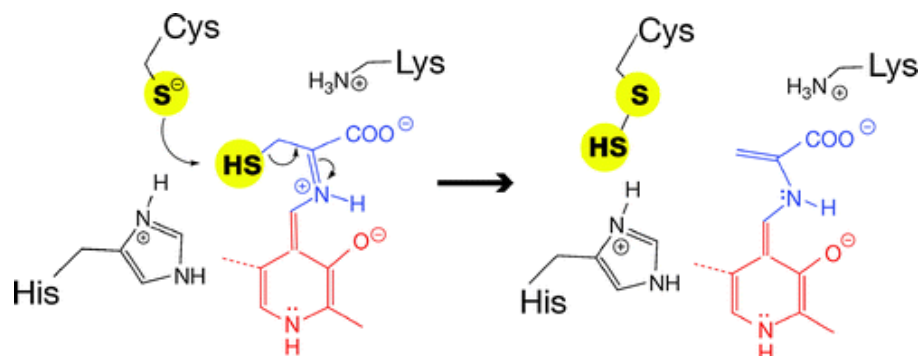
Figure 1-6. Sulfur-carbon bond cleavage mechanism for the cysteine desulfurase. An enzyme-bound persulfide is formed by nucleophilic attack of the thiolate anion by the mobile loop cysteine on the sulfur of the substrate cysteine-PLP adduct. The cysteine is shown in blue and the PLP is shown in red. Reprinted with permission from *Annual Review of Biochemistry*, 74: 247-281. Copyright 2005 Annual Reviews Publishing Group.
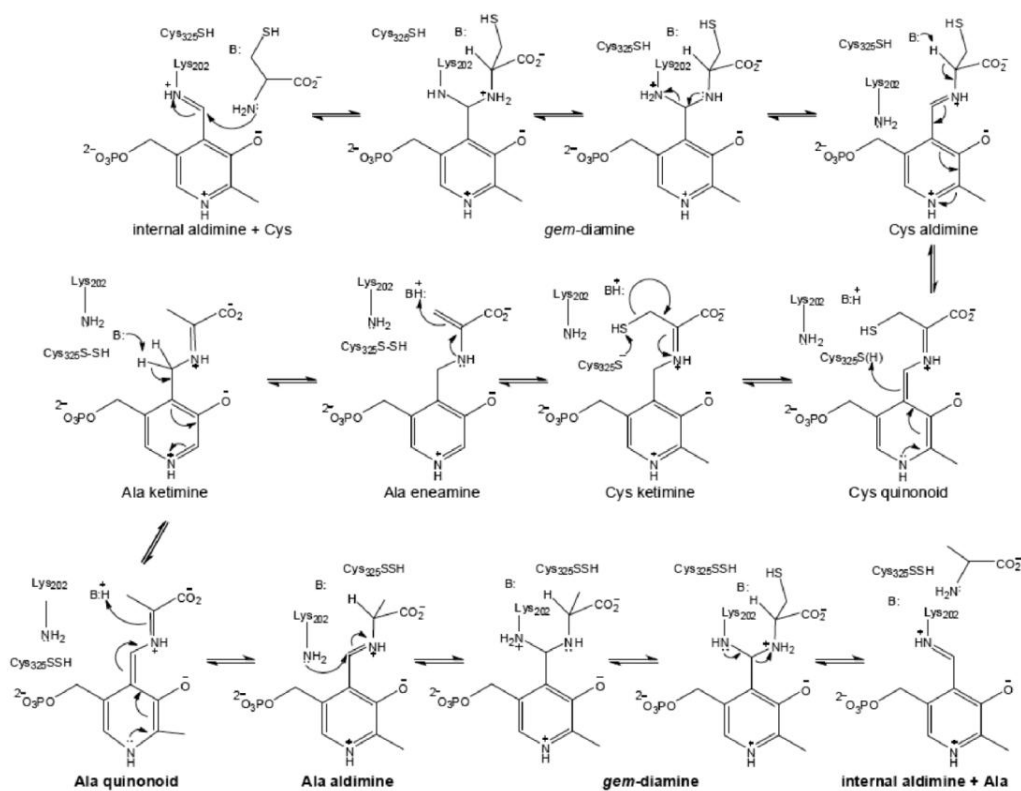
Figure 1-7. Mechanism of PLP catalyzed conversion of the cysteine to alanine with persulfide formation on the catalytic cysteine of the cysteine desulfurase. Adapted from Zheng *et al.*, Biochemistry 1994 33, 4714-4720.

7

Extensive biochemical and structural interrogation of the scaffold protein and cluster assembly have been performed. From this the SD complex has been shown to directly interact with the scaffold protein ISCU (U) to form a 170 kDa complex, denoted SDU [22]. Formation of a covalent interaction between the terminal sulfane atom of the NFS1 persulfide with one of the conserved cysteine residues (C104) of ISCU facilitates sulfur transfer to the scaffold protein [5-6, 30-32]. Based on structural data from several homologues human ISCU is expected to be a highly flexible molten globule-type protein, with this flexibility aiding in the multiple protein-protein interactions necessary for cluster assembly and transfer [33-38]. As one of the most highly conserved proteins in nature ISCU has several invariably conserved residues, including the three cysteine residues (C35, C61, and C104) involved in cluster binding. Based on crystallographic and spectroscopic data three residues, the semi-conserved cysteine (C96) and histidine (H112) and the invariably conserved aspartate (D37), have been proposed to serve the role of the fourth cluster ligand [34-35, 37, 39]. Unpublished data from Barondeau *et al* indicates that Cys96 is dispensable *in vitro*, thus it is unlikely that this residue serves as the fourth cluster ligand [32]. Additionally, mutagenesis data by Cowan *et al* suggests a role for His112 in iron binding and delivery, rather than cluster ligation [40]. Thus the D37 aspartate residue, with its proposed role in labilizing the cluster for cluster transfer, is likely the fourth cluster ligand [9, 35]. Based on *in vitro* studies of the *A. vinelandii* ISCU homologue the scaffold protein can assemble both [2Fe-2S] and [4Fe-4S] clusters, with the cubane cluster resulting from reductive coupling of two [2Fe-2S] clusters [41-42]. Such versatility allows ISCU to serve as a scaffold for multiple types of cluster

assemblies and could enable it to sense and mediate the cluster distribution of biological systems, switching between production of [2Fe-2S] and [4Fe-4S] clusters as needed.

Completion of cluster assembly requires two final components, an iron donor and an electron source. Once sulfur transfer is complete, the iron donor can supply the ferrous iron necessary to complete cluster assembly [5-6]. Although this role was initially proposed to belong to the protein frataxin (FXN, F), much dispute remains as to the identity of the iron donor (See below for further discussion of frataxin). More recently ISCA has been proposed to serve this function for cluster assembly. Ferredoxin and ferredoxin reductase are proposed to provide the two electrons needed to reduce the cysteine sulfane sulfur (S^0) to a sulfide (S^{2-}).

Upon completion of cluster assembly the human HSCA/HSCB ATP-dependent proteins, GRP75/HSP70/mortalin and HSC20, respectively; interact with the ISC specific LPPVK binding motif of ISCU to facilitate cluster transfer to apo-protein targets [43-46]. In addition to the proteins mentioned above, several other proteins have been suggested to serve a role in cluster assembly or transfer; including the glutaredoxin GRX5 which has been implicated in the reduction of disulfide bonds within or between proteins or as a chaperone for cluster transfer, the alternative scaffold proteins NFU1 and ISA, and the HSP70 escort protein HEP1 which has been shown to activate and solubilize GRP75 [4, 6, 9, 47-48]. Further investigation will shed more light on the specific role of these proteins in human Fe-S cluster biosynthesis.

Initial interest in the protein frataxin (FXN, F) was sparked in the mid-1980s, when it was identified as the protein responsible for the neurodegenerative disease

Friedreich's ataxia or FRDA (See further discussion of FRDA below) [49-50]. As part

of the human genome sequencing initiative, expression of frataxin was linked to the

FRDA or χ25 gene located on chromosome 9q. Further sequence analysis revealed that

homologues of human FXN are present in all living organisms, suggesting a vital role

for this protein [51-52]. Despite this ubiquitous role, wide variability of the protein

sequence, especially at the N- and C-terminus, and lack of structural data posed

challenges to elucidating the role of FXN and its homologues.

Much needed structural data was obtained in the early 2000s when the human

FXN and homologous *E. coli* CyaY structures were determined (Figure 1-8) [51-54].

Despite having only 25% sequence identity, the structures for the two homologues are

relatively well conserved and revealed a unique and previously uncharacterized protein

fold. The overall tertiary structure of FXN is a compact αβ sandwich with the

hydrophobic core of the protein being formed from an unique five strand anti-parallel β

sheet (β_1- β_5) that packs against two parallel α helices (α_1 & α_2). The hydrophobic core

of the protein is further stabilized by the C-terminal loop of the protein, which fills the

grove between the two α helices. Based on structural and biochemical data two unique

features were identified; the first, an acidic ridge on the α_1 helix composed of 12 semi-

conserved acidic residues were proposed as an iron binding site and the second, several

conserved residues (N146, Q148, Q153, W155, & R165) on the β sheet were suggested

as a possible location for protein-protein interactions [27, 51-56].
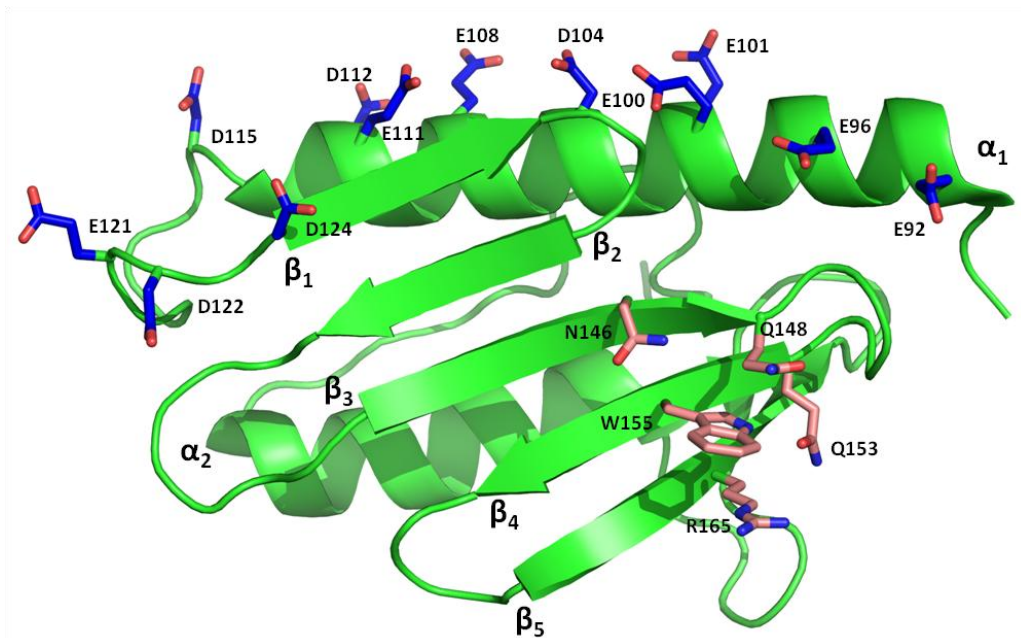
Figure 1-8. Crystal structure of human FXN residues 89-209 (PDB code 3S4M). Blue residues are the 12 semi-conserved acidic residues of FXN. Pink residues are β-sheet residues of FXN proposed to participate in protein-protein interactions.
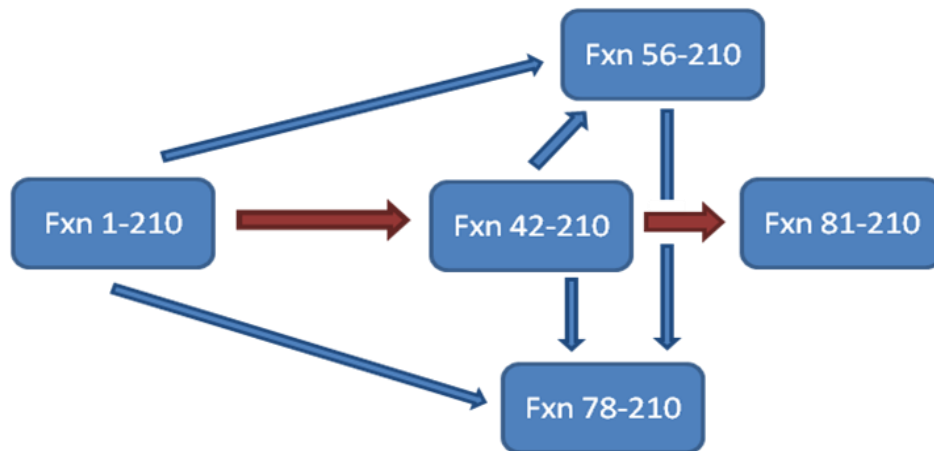
Figure 1-9. Primary (red) and alternative (blue) processing routes for maturation of human FXN. The numbers indicate the residues present in that form of FXN.

Characterization of FXN was further complicated by the discovery of multiple FXN variants and isoforms [57-63]. Frataxin is initially synthesized as a 210 amino acid precursor (amino acids 1-210, 23 kDa) which can then be processed via the mitochondrial processing peptidase (MPP) or self-proteolysis into one of four forms, FXN^{42-210}, FXN^{56-210}, FXN^{78-210}, and FXN^{81-210}. All four forms have been shown to exist in human cells; with FXN^{81-210}, FXN^{56-210}, and FXN^{78-210} having the ability to replenish aconitase activity in frataxin depleted cells. Additionally while Fxn^{81-210} and Fxn^{78-210} have been shown to exist solely as monomers, both Fxn^{42-210} and Fxn^{56-210} have been shown to exist in both monomeric and oliogmeric forms. Although several processing routes have been proposed (Figure 1-9), it is now widely accepted that mitochondrial processing of FXN occurs in two steps. The first step is cleavage of the mitochondrial targeting sequence (aa 1-41) upon transport of the preprotein (FXN^{1-210}) into the mitochondria, followed by further processing to produce the mature form, Fxn^{81-210} (14 kDa).

Over the past 30 years several roles have been assigned to FXN: (1) iron storage, (2) reactive oxygen species (ROS) control, (3) iron chaperone, (4) metabolic switch, and (5) iron sensor (Figure 1-10) [64-75].
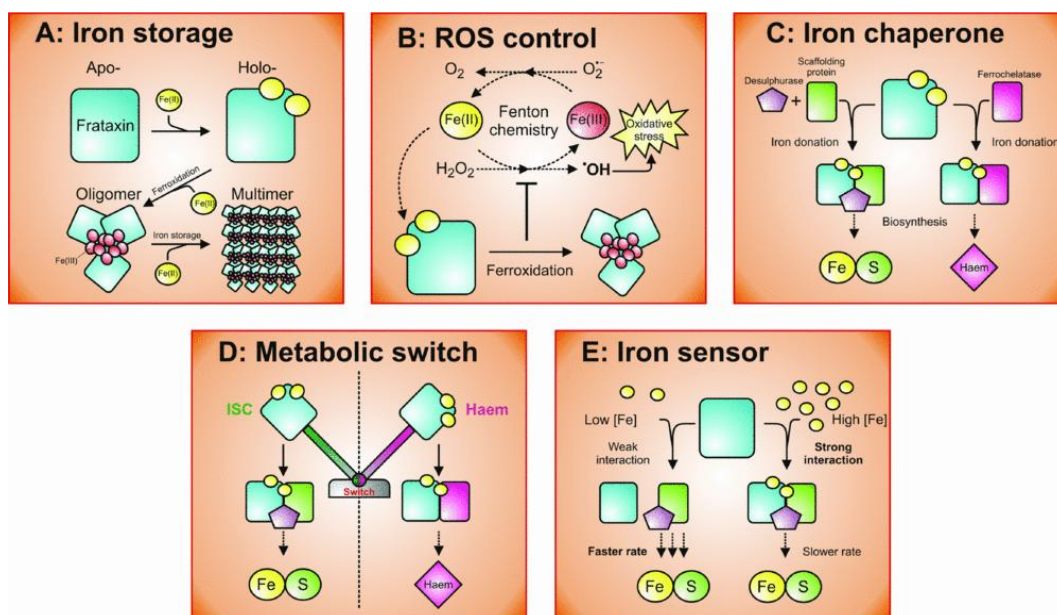
Figure 1-10. Proposed functions of the frataxin protein family. Reprinted with permission from *Biochemical Journal*, 426(2): e1-e3. Copyright 2010 Biochemical Society Publishing Group.

Both the iron storage and ROS control roles are attributed to oligomeric states of the FXN protein family [69-71, 73-75]. The iron storage role was suggested based on the formation of ferrihydrite mineral cores within oligomeric forms of yeast (Yfh1), *E. coli* (CyaY), and human (FXN) frataxin homologues, similar to those seen in the iron storage protein ferritin [69-71, 73]. Despite this observation, growing experimental evidence contradicts the validity of this role *in vivo* [76-78]. The ROS control role is directly coupled to the iron storage role of FXN stemming from the ability of the ferrihydrite core to mediate reactive oxygen species, by employing these species in the reduction of Fe^{2+} to Fe^{3+} to form the ferrihydrite core [70, 74-75]. As with the role as an iron donor, this role has also been brought into question by findings that oligomerization is dispensable *in vivo* and evidence that FXN mediation of ROS causes extensive damage

to the protein (See below for further discussion of oligomeric FXN) [75-76]. Until

recently, the most widely accepted role for FXN was that of an iron chaperone [67-68,

72]. This role was initially assigned based on the work of Stemmler *et al* with yeast

Yfh1 and Cowan *et al* with human FXN which showed that both monomeric yeast and

human frataxin bind iron with micromolar affinity [68, 72]. These findings were further

strengthened when the Cowan group demonstrated that FXN bound iron could be

transferred to ISCU for *in vitro* cluster assembly [68]. This was shortly followed by

results from the Dancis group suggesting that yeast Yfh1 supplied iron for heme

synthesis [67]. A fourth, metabolic switch, role was proposed for FXN in which FXN

expression levels served as a switch to govern the flow of iron either for Fe-S cluster

assembly or for heme synthesis [65]. Frataxin has also been implicated by Pastore *et al*

as an iron sensor, based on findings that *E. coli* CyaY serves as a negative regulator of

Fe-S cluster biosynthesis in the *E. coli* system [64]. This regulation would allow CyaY

to finely tune the amount of Fe-S clusters produced based on the availability of apo

acceptor proteins. Finally a general role in iron homeostasis has also been proposed for

frataxin, due to the ubiquitous observation of increased iron import in the mitochondria

and decreased cytosolic iron levels upon depletion or deletion of the *FXN* gene in

prokaryotes and eukaryotes [79-81]. More recently, frataxin was found to interact with

both NFS1/ISD11 and ISCU to form a four protein complex, denoted SDUF [22].

Frataxin binding to SDU dramatically impacts the K_M for cysteine from 0.59 to 0.011

mM and increases the catalytic efficiency (k_{cat}/K_M) of Nsf1 more than 300 fold from 25

(SDU) to 7,900 $M^{-1}s^{-1}$ (SDUF). This rate (k_{cat}/K_M) is further stimulated to 10,500 $M^{-1}s^{-1}$

with the addition of ferrous iron. These results indicate that frataxin, in combination

with ferrous iron, acts as an allosteric activator of the SDU complex, suggesting a pre-

equilibrium model for stimulation of sulfur transfer and Fe-S cluster biosynthesis (Figure

1-11). These results have recently been confirmed for Fe-S cluster assembly in the

mouse system [28]. Additionally Pastore *et al* has also proposed a regulator role for the

bacterial frataxin homologue CyaY, with CyaY serving as an inhibitor for Fe-S cluster

biosynthesis in the bacterial system [64]. The use of human FXN as an allosteric

activator for Fe-S cluster biosynthesis is also supported by data from Barondeau *et al*

showing a role reversal between frataxin homologues in the prokaryotic and eukaryotic

systems [82].
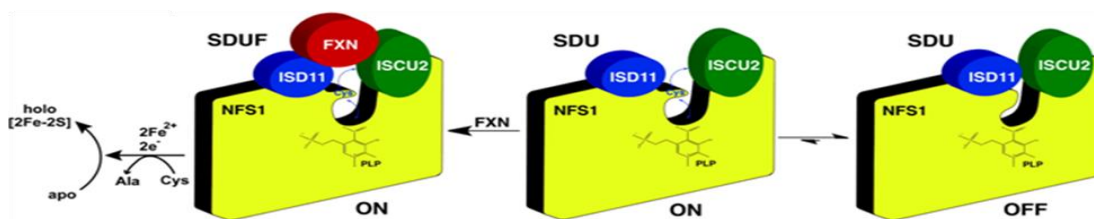
Figure 1-11. Pre-equilibrium model of FXN regulation of Fe-S cluster assembly. In the absence of FXN an "Off" conformation of SDU is favored, which limits the cysteine desulfurase and Fe-S cluster activity. Binding of FXN to SDU stabilizes the complex converting it to an "On" state, which promotes cysteine desulfurase activity and Fe-S cluster assembly. Reprinted with permission from *Biochemistry*, 51(12): 2506-2514. Copyright 2012 American Chemical Society.

The work presented here builds on the allosteric activator model for FXN,

providing a map of residues involved in the interaction with SDU. Additionally the

properties of FXN variants, including clinical mutant L182F and oligomeric FXN[56-210],

were interrogated. Taken together this data has implications for future development of

therapeutics for the disease Friedreich's ataxia.

CHAPTER II

KINETIC AND STRUCTURAL INTERROGATION OF THE

FRIEDREICH'S ATAXIA VARIANTS L182H & L182F AND

ACETYLATION MIMICS OF K197

INTRODUCTION

Several human diseases including sideroblastic anemia, mitochondrial

encephalomyopathy, and Friedreich's Ataxia (FRDA) have been linked to mutations in

Fe-S cluster biosynthesis proteins [6-7, 17, 83]. FRDA is an autosomal recessive

neurodegenerative disease [84-86]. As the most common form of hereditary ataxia,

FRDA has an estimated prevalence of 1 in 50,000 and an estimated carrier rate between

1:60 and 1:120 in the European population. The disease is characterized by limb and

gait ataxia (loss of coordination), dysathria (motor speech disorder resulting in poor

articulation), sensory loss, diabetes, and cardiomyopathy (most frequent cause of death

in patients). Onset of symptoms typically occurs before the age of 25 years, with most

patients presenting symptoms in their pre-teen to early teen years.

About 95% of FRDA patients are homozygous for an unstable GAA trinucleotide

repeat expansion on intron 1 of the *FXN* gene [86-88]. A strong correlation has been

determined been the GAA repeat length of the shorter allele of these patients and the age

of onset and disease progression [85]. These expanded GAA sequences range from 44

to 1,700 repeats, compared to the range of 6 to 36 repeats seen in unaffected individuals,

and result in non-B type "sticky" DNA structures [86-87, 89]. These sticky DNA

structures limit DNA replication and repair, *FXN* RNA levels, and protein expression. *In vivo* consequences of the decreased levels of FXN are the loss of Fe-S enzyme activity, iron accumulation in the mitochondria, and increased susceptibility to oxidative stress (Figure 2-1).
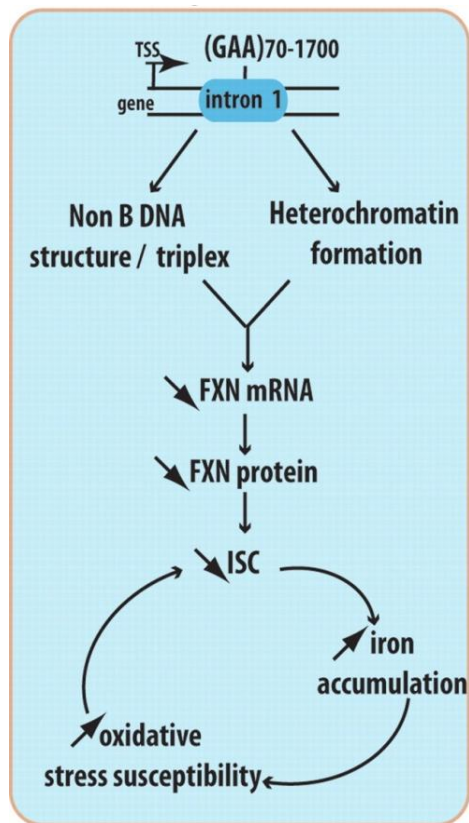
Figure 2-1. Model of the pathological mechanism of FRDA. Reprinted with permission from *Human Molecular Genetics*, 19 (R1): R103-R110. Copyright 2010 Oxford University Press.

The remaining ~5% of patients are heterozygous for a GAA expansion on one allele and one of 43 identified mutations on the other allele [86, 88]. Included in these mutations are 17 identified point mutants of the *FXN* gene (Figure 2-2) [86]. The

clinical phenotypes of these patients are more complex, lacking the correlation between

disease phenotype and GAA repeat length seen in homozygous patients [86, 90]. Some

patients demonstrate typical FRDA symptoms, consistent with those seen in the

homozygous population (GAA repeat expansion on both *FXN* alleles), whereas other

individuals exhibit milder or more severe neurodegenerative symptoms. Hypotheses to

define the function of FXN and correlate the point mutants on FXN with the clinical

phenotype for heterozygous patients is complicated by the inability to separate the

effects of the GAA expansion from those of the point mutation, which could alter the

stability and/or function of FXN.
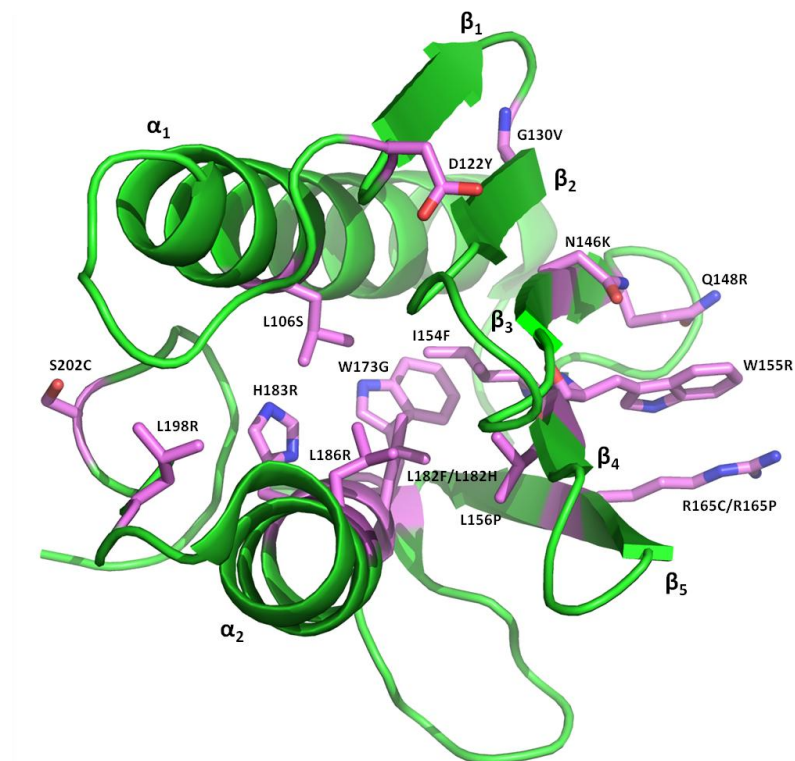
Figure 2-2. Crystal structure of human frataxin residues 89-209 (PDB code: 3S4M), with residues of identified FRDA mutants shown in purple. Residue labels indicate the FRDA point mutant(s) known to occur at each residue.

Coupling *in vivo* and *in vitro* characterization of FRDA point mutations (Table 2-1) will lead to an improved understanding of the function of FXN and may provide insight into new therapeutic approaches for FRDA [86-88, 90-100]. Three factors have been suggested to play a role in the *in vivo* phenotypes of FRDA point mutations: 1.) processing defects, 2.) kinetic impairment, and 3.) loss of protein stability [54, 57, 86, 92-94, 99]. *In vivo* work has identified five mutants (R40C, G130V, I154F, L156P, & W173G) with apparent processing defects, resulting in reduced levels of the mature FXN$^{81-210}$ protein [54, 57, 86]. Findings by Barondeau *et al* suggest an allosteric activator role for human FXN with the Fe-S cluster assembly complex (SDU) [22]. This role is further supported by findings from the Barondeau group showing kinetic impairment of FRDA mutants from the conserved β-sheet region of FXN [92, 99]. All five clinical mutants (N146K, Q148R, I154F, W155R & R165C) were found to have either defects in binding and/or activation of the cysteine desulfurase and Fe-S cluster biosynthesis of the SDU complex. Finally significant protein instability has been demonstrated for three FRDA clinical mutants (D122Y, G130V, & I154F) [93-94].

More recently several post-translational modifications, including lysine acetylation, carbonylation, nitration, and ubiquitination, have been identified on FXN [103-106]. These modifications present additional aspects of FXN for investigation, as they likely modulate *in vivo* functions of FXN such as protein-protein interactions and could play a role in disease. One such post-translational modification was identified by Denu *et al* in a calorie restricted mouse model deleted of the mitochondrial deacetylase SIRT3 [104]. Based on these results mouse K194 (K197 in human) is acetylated and is

proposed to play an *in vivo* role in ubiquitin/acetylation cross talk for FXN. This work interrogates the stability and function of FRDA clinical mutants and the function of acetylation mimics in the context of the SDU complex.

Table 2-1. *In vivo* and *in vitro* characterization of Friedreich's ataxia point mutants.

FXN Isoform 1 Mutants	Disease Phenotype [b]	GAA Expansion Size of Other Allele	*In vivo* Frataxin Levels (%)	*In vivo* Processing Defects	T_m Values (°C)	Cysteine Desulfurase Activity (units/min^{-1})	Fe-S Cluster Formation (units/min^{-1})	FXN K_d (μM)	k_{cat} (min^{-1})	K_M^{Cys} (mM)	k_{cat}/K_M (M^{-1}s^{-1})
Wild-type	None	6-36	100%		66.3 [n-o], 62 [p++]	8.25±0.90 [s]	12.3±0.4 [s]	0.22±0.05 [s]	8.5±0.3 [s]	0.014±0.002 [s]	9800±1700 [s]
R40C+	Typical	normal expansion [c]		mutates MPP cleavage site FXN$^{1-210}$ accumulation [b,c]							
L106S	Atypical (mild)	832 [d], 840 [e]	5.9 [d], ND [e]								
D122Y	Atypical (mild)	750 [f]			50.4 [n]						
G130V	Atypical (mild)	800 [f], 840(2) [d], 866(3) [f], 986 [d], 994 [g], 1000 [f], 1033 [f], 1080 [h], 1330 [h]	ND [f], 14.5 [d], 12.4 [d], ND(3) [f], 6.6 [d], ND [g], ND [f], ND [f], ND [h], ND [h]	reduced FXN$^{81-210}$ levels slower processing rate [b]	43.2 [n]						
N146K	Atypical (mild)	820 [i]				1.08±0.08 [q]	2.8±0.3 [q]	6.25±1.40 [q]	4.0±0.1 [q]	0.019±0.004 [q]	3500±700 [q]
Q148R	Typical					1.29±0.20 [q]	2.9±0.2 [q]	0.85±0.15 [q]	2.0±0.1 [q]	0.019±0.004 [q]	1800±300 [q]
I154F	Typical	625 [b], 633 [d], 700 [f], 800 [f], 920(2) [f], 960 [f], 1010 [j]	ND [b], 17.6 [d], ND [f], ND [f], ND [f], ND [f], ND [j]	reduced FXN$^{81-210}$ levels slower processing rate [b]	50.7 [o], 50 [p++]	4.14±0.20 [r]	7.6±0.5 [r]	0.63±0.14 [r]	6.6±0.4 [r]	0.025±0.004 [r]	4400±800 [r]
W155R	Typical (early onset)	734 [d], 750 [b]	17.9 [d], ND [b]		61.4 [o], 55 [p++]	0.60±0.07 [r]	0.9±0.1 [r]	6.73±1.28 [r]	1.8±0.1 [r]	0.013±0.003 [r]	2300±500 [r]
L156P	Typical	366 [f]		reduced FXN$^{81-210}$ levels [b]							
R165C	Atypical (mild)	380 [h], 1000 [k], 1000 [d]	ND [h], ND [k], 46.4 [d]			1.26±0.10 [q]	4.1±0.9 [q]	10.40±2.26 [q]	8.1±0.1 [q]	0.012±0.001 [q]	11000±1400 [q]
R165P	Typical (early onset)	940 [j], 1100 [j]									
W173G	Typical	530 [j], 570 [j], 620 [j], 720 [f], 820 [j]	6.9 [j], ND [j], 18.9 [j], ND [f], 14.3 [j]	Inhibits 2nd cleavage step FXN$^{42-210}$ accumulation [b, m]							
L182F	Atypical (mild)	730 [h]									
L182H	Typical	800 [f]									
H183R	Typical	1000 [f]									
L186R	Typical	920 [i]									
L198R	Typical										
S202C [a]	Typical										

\+ Mutation identified in a patient with hypertrophic cardiomyopathy containing normal GAA repeat lengths on the FXN gene. [100]
++ Used FXN construct containing residues 63-210. [54]
a.) Roman & Santos, *PLoS ONE*, 2012. [101]
b.) Santos & Lesuisse, *Antioxidants & Redox Signaling*, 2010. [86]
c.) Van Driest & Acerman, *Molecular Genetics and Metabolism*, 2005. [100]
d.) Deutsch & Lynch, *Molecular Genetics & Metabolism*, 2010. [102]
e.) Bartolo & Prior, *American Journal of Medical Genetics*, 1998. [91]
f.) Cossée & Pandolfo, *Annals of Neurology*, 1999. [87]
g.) Diehl & Natowicz, *Neurogenetics*, 2010. [95]
h.) Forrest & Nicholson, *Neurogenetics*, 1998. [96]
i.) Zuhlke & Schwinger, *European Journal of Human Genetics*, 2004. [88]
j.) Gellera & Taroni, *Neurogenetics*, 2007. [97]
k.) McCormack & Lynch, *Journal of Neurology, Neurosurgery, & Psychiatry*, 2000. [98]
m.) Cavadini & Isaya, *The Journal of Biological Chemistry*, 2000. [57]
n.) Correia & Gomes, *FEBS Journal*, 2008. [94]
o.) Correia & Gomes, *Biochemistry Journal*, 2006. [93]
p.) Musco & Pastore, *Structure*, 2000. [54]
q.) Bridwell-Rabb & Barondeau, *Biochemistry*, 2011. [92]
r.) Tsai & Barondeau, *Biochemistry*, 2011. [99]
s.) Tsai & Barondeau, *Biochemistry*, 2010. [22]

EXPERIMENTAL PROCEDURES

Protein Preparation. The point mutations (L182H, L182F, K197A, K197Q, K197R, and K197C) were introduced into a pET11a plasmid containing a codon optimized human *FXN* gene (FXN Δ1-55), lacking the first 55 amino acids, using the QuikChange method (Stratagene) [22]. The individual mutations were confirmed by DNA sequencing (Texas A&M University Gene Technology Laboratory). The plasmids containing each mutant were transformed into *E. coli* BL21(DE3) competent cells and grown at 37 °C, until an OD_{600} of ~0.7 was obtained. Protein expression was then induced with 0.5 mM isopropyl β-D-1-thiogalactopyranoside (IPTG), and cells were incubated at 16 °C for 16 hours. The cells were then harvested by centrifugation and lysed by sonication (Branson Sonifier 450) in 50 mM Tris pH 7.5. The supernatant for the soluble variants (L182F, K197A, K197Q, K197C) was loaded onto an anion exchange column (26/20 POROS 60HQ, Applied Biosystems) and eluted with a linear gradient from 0 to 800 mM NaCl in 50 mM Tris pH 7.5. The fractions corresponding to monomeric frataxin were collected, concentrated, and loaded onto either a Sephacryl S100 or S300 (26/60, GE Healthcare) size exclusion column equilibrated with 50 mM HEPES, 150 mM NaCl pH 7.5. The L182H FXN mutant was isolated using the guanidine hydrochloride refolding procedure from Palmer and Wingfield [107]. The L182H protein extract was then refolded using the Pierce Protein Refolding Kit protocol and dialyzed into 50 mM Tris pH 7.5. Protein refolding was initially analyzed by monitoring the UV-vis absorbance ratio between 260 nm, 270 nm, and 280 nm of each refolding condition, and the secondary structure of identified conditions was analyzed by

circular dichroism. Protein concentrations for each mutant were calculated using their absorbance at 280 nm using an extinction coefficient of 26030 $M^{-1}cm^{-1}$ [108]. The ISCU2 and NFS1/ISD11 proteins were purified as previously described and their protein concentrations determined using extinction coefficients of 10,900 $M^{-1}cm^{-1}$ (PLP) and 8250 $M^{-1}cm^{-1}$ based on their absorbance at 420 nm and 280 nm, respectively [22, 108].

Cysteine Desulfurase Activity Measurements. Reactions were performed as previously described using a total volume of 800 μL [22, 109-110]. The initial reaction mixtures containing 0.5 μM NF$\underline{S}$1/IS$\underline{D}$11 (SD), 1.5 uM ISCU2, 1.5 μM FXN (or FXN point mutant), 10 μM pyridoxal-5'-phosphate (PLP), 2 mM dithiothreitol (DTT), 5 μM Fe$(NH_4)_2(SO_4)_2$, and 50 mM Tris, 250 mM NaCl pH 8.0 were incubated for 30 minutes in an anaerobic glovebox at ~14 °C [22]. The cysteine desulfurase reaction was initiated with the addition of 100 μM L-cysteine at 37 °C, and quenched with 100 μL each of 20 mM *N,N*-dimethyl-*p*-phenylenediamine in 7.2 N HCl and 30 mM $FeCl_3$ in 1.2 N HCl. Following 20 minute incubation at 37 °C and centrifugation for 5 minutes at 12,000 rpm, the methylene blue formation was measured at 670 nm and converted to sulfide production using a Na_2S standard curve. The rate is expressed in units of mol sulfide per mol SD per minute at 37 °C. The cysteine desulfurase reaction rates were also determined for increasing concentrations of FXN and FXN mutants, in order to determine the number of equivalents of each variant required to saturate the cysteine desulfurase activity.

Michaelis-Menten Kinetics for Frataxin Variants in SDUF Complex. Saturating amounts of the FXN mutants were added to a standard reaction mixture of 0.5 μM (SD),

1.5 uM ISCU2, 10 μM pyridoxal-5'-phosphate (PLP), 2 mM dithiothreitol (DTT), 5 μM

Fe(NH$_4$)$_2$(SO$_4$)$_2$, and 50 mM Tris, 250 mM NaCl pH 8.0 [92, 99]. Reactions were

incubated for 30 minutes in an anaerobic glovebox before being initiated with the

addition of 12.5 - 600 μM L-cysteine. The rate of cysteine desulfurase activity was

analyzed as above. The reaction rates were plotted verses L-cysteine concentration and

fit with the Michaelis-Menten equation in KaleidaGraph. The k_{cat} was determined at

varying FXN concentrations and used to determine the binding constant of FXN to the

SDU complex. These results were fit as a type II allosteric activator using Eq. 2-1 in

KaleidaGraph, where the [SDUF] is calculated as shown in Eq. 2-2 [32].

$$k_{obs} = \frac{k_{SDU}([SDU]_{total} - [SDUF]) + k_{SDUF}^{\infty}[SDUF]}{[SDU]_{total}}$$

(Eq. 2-1)

$$[SDUF] = \frac{[SDU]_{total} + [FXN]_{total} + K_d - \sqrt{([SDU]_{total} + [FXN]_{total} + K_d)^2 - 4[SDU]_{total}[FXN]_{total}}}{2}$$

(Eq. 2-2)

RESULTS

Clinical Mutant and Acetylation Mimics have Little Effect on Fe-S Assembly Complex Activity. The L182F, K197A, K197C, K197Q, & K197R mutants were expressed in *E. coli* and purified to >95% homogeneity. During the protein purification process the Δ1-55 FXN construct spontaneously truncated to produce the mature (FXN$^{81-210}$) form of the protein [32, 111]. The ability of the clinical mutant (L182F) and acetylation mimics (K197A, K197Q, K197R) to stimulate the cysteine desulfurase activity of the SDU complex was investigated. In order to approximate *in vivo* cellular conditions 100 μM L-cysteine and equal amounts of the FXN variants were used [22]. All four mutants showed similar cysteine desulfurase activities to that of the wild-type protein, with the activity of the K197R variant slightly elevated compared to that with the addition of wild-type FXN (Figure. 2-3).

Michaelis-Menten Kinetic Parameters for Assembly Complexes with Frataxin Variants. Michaelis-Menten parameters for the cysteine desulfurase reaction were determined after the addition of the FXN FRDA L182F variant and the acetylation mimicking K197 mutants. First, the cysteine desulfurase activity was measured as a function of added FXN variant to determine the number of equivalents necessary to saturate the enzymatic activity and overcome any differences in the ability of the FXN variants to bind to the SDU complex and activate the cysteine desulfurase. The cysteine desulfurase activity saturated after the addition of 3eq for FXN, 5eq of the L182F variant, and 10 eq for the K197A, K197Q, and K197R variants (data not shown). Second, Michaelis-Menten parameters k_{cat} and K_M were determined by monitoring the

cysteine desulfurase activity as a function of L-cysteine using the previously determined saturating amounts of FXN (Table 2-2 & Figure 2-4). Third, the FXN binding constants (K_d) to the SDU complex for the L182F and K197Q FXN variants were determined by measuring the k_{cat} as a function of FXN concentration (Figure 2-5 & Table 2-2).
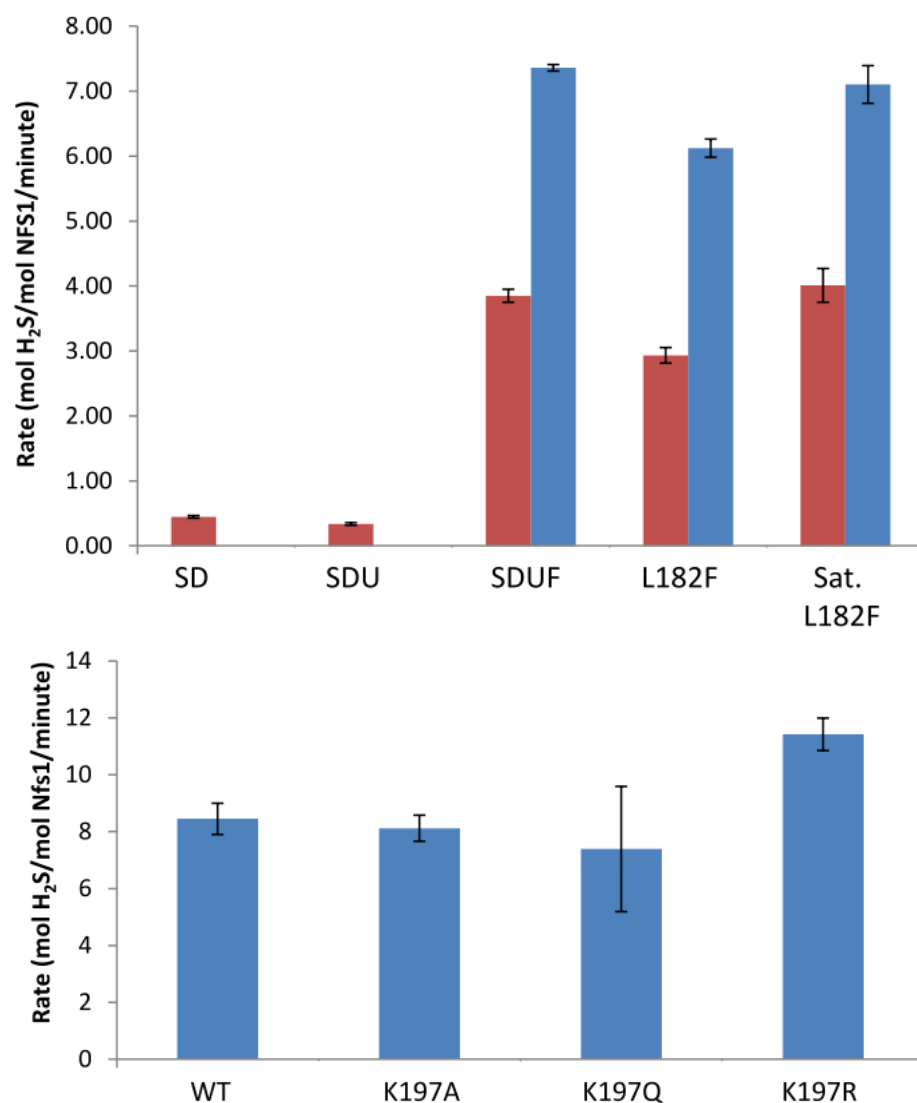
Figure 2-3. Bar charts of the cysteine desulfurase activity of the L182F mutant (top) and the acetylation mutants K197A, K197Q, and K197R (bottom). Red bars represent samples without ferrous iron and blue bars are samples with ferrous iron.
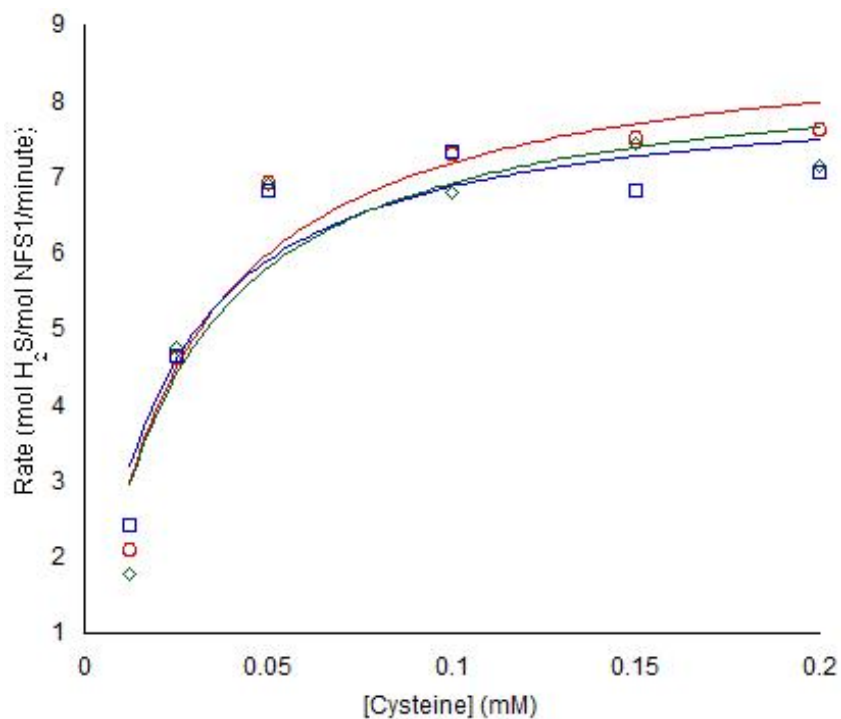
Figure 2-4. Determination of the Michaelis-Menten parameters k_{cat} and K_M for FXN variants L182F and K197Q. The methylene blue assay rates were determined at saturating concentrations of FXN variants and varied cysteine concentrations. The data points and fit to the Michaelis-Menten equation are displayed in red (WT), blue (L182F), and green (K197Q). The R^2 values are 0.92 (WT), 0.89 (L182F), and 0.87 (K197Q).

Table 2-2. Kinetic parameters for SDU with FXN variants L182F & K197Q

Complex	FXN K_d (μM)	k_{cat} (min^{-1})	K_M^{Cys} (mM)	k_{cat}/K_M (M^{-1}/s^{-1})
SDU + FXN	0.07 ± 0.04	9.0 ± 0.7	0.025 ± 0.008	6000 ± 1900
SDU + L182F	0.05 ± 0.02	8.2 ± 0.7	0.020 ± 0.007	6900 ± 2400
SDU + K197Q	0.03 ± 0.01	8.6 ± 0.9	0.024 ± 0.010	6000 ± 2500
SDU	NA	0.37 ± 0.05	0.514 ± 0.212	12 ± 5
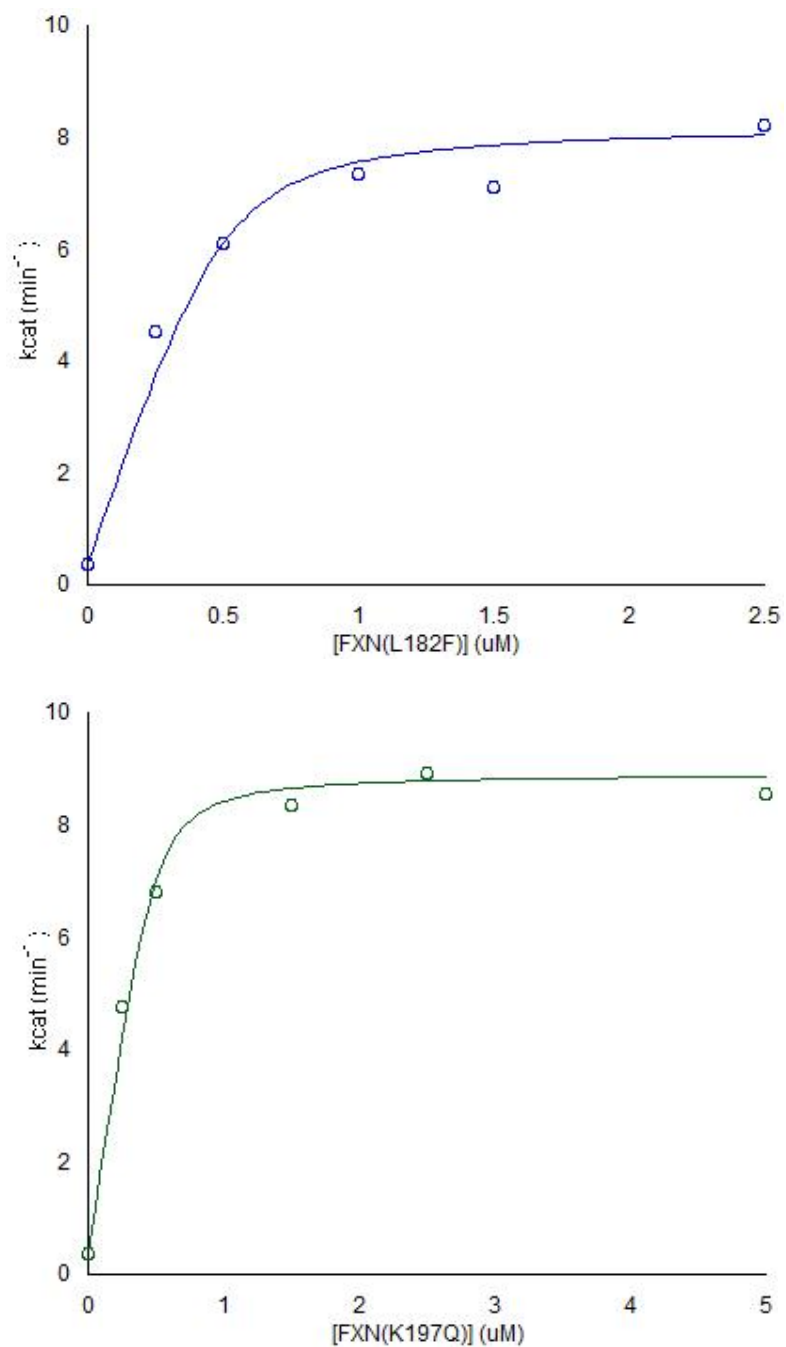
Figure 2-5. Determination of binding constants for FXN variants L182F (blue, top) and K197Q (green, bottom). The k_{cat} values were determined at varying FXN concentrations. The data is fit as a type II allosteric activator using Eq. 2-1. The R^2 values are 0.97 (L182F) and 0.99 (K197Q).

Circular Dichroism Analysis of the L182H FXN Variant. As the L182H variant

expressed in the insoluble fraction, analysis of protein refolding was required. Initial

analysis of the refolding conditions through comparison of the UV-vis absorbance ratios

at 260 nm, 270 nm, and 280 nm was performed. Folded samples should have a higher

absorbance level at 280 nm, while unfolded samples will have a higher absorbance level

at 260 nm. Based on this, three possible refolding conditions (3, 7, & 8) from the Pierce

Protein Refolding Kit protocol were identified. Circular dichroism (CD) analysis of the

secondary structure of the L182H mutant in all three conditions, determined that only

condition 8 (55 mM Tris pH 8.2, 21 mM NaCl, 0.88 mM KCl, 1.1 M guanidine

hydrochloride, and 0.44 M arginine) resulted in folded protein. When assessing the

secondary structure of a protein by CD, three distinct features are used. Within the CD

spectrum of a folded protein α helices exhibit peaks at about 208 nm and 222 nm, while

β-sheets show a single peak at about 212 nm. In contrast proteins completely lacking

secondary structural elements (random coil), are missing these features. Instead they

demonstrate a sharp peak around 200 nm and an essentially baseline spectrum from 210-

250 nm. Analysis of the secondary structural elements of wild-type FXN, are in good

agreement with the expected spectral features for a well folded protein containing α

helices and β-sheets. Comparison of the spectra of the L182H variant and wild-type

FXN shows similarities in the overall spectral shape; however the L182H spectrum is

much broader than that of wild-type FXN. Although the mutant appears to regain

secondary structure, the broadened spectrum suggests that a slight difference in overall

fold is present within the L182H variant (Figure 2-6). An instability or disruption of the

protein fold is further supported by CD analysis revealing loss of the protein fold after

two days, as evidenced by a CD spectrum corresponding to a random coil structure.
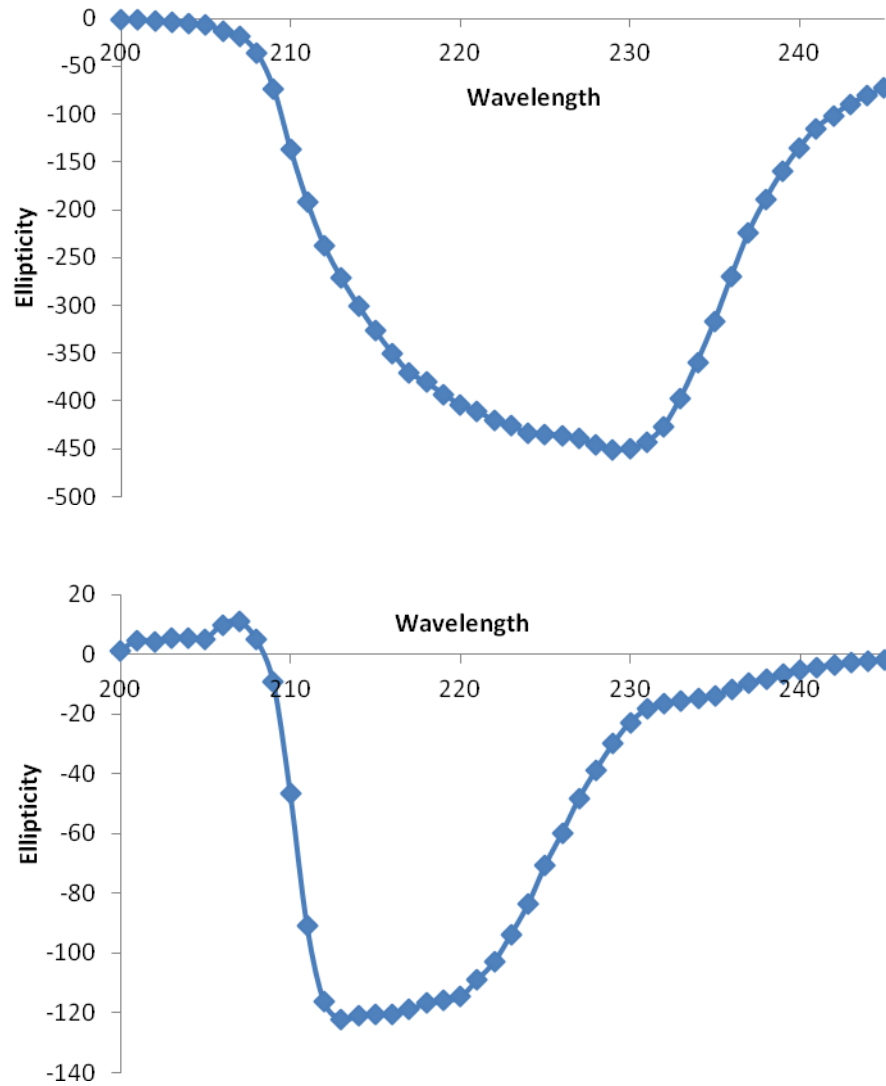
Figure 2-6. Circular dichroism spectra for refolding condition 8 with L182H (top) and wild-type FXN (bottom).

DISCUSSION

The clinical Friedreich's ataxia (FRDA) mutants N146K, Q148R, I154F, W155R, and R165C have previously been shown to exhibit compromised binding to the SDU complex and defects in the ability to activate the cysteine desulfurase [92, 99]. Based on the available biochemical data, four different classifications of FXN mutants have been proposed. The Class I variants are characterized by both a significant binding and activation defect of the cysteine desulfurase; with W155R exhibiting a 78-fold weaker binding and about 20% of the activity of wild-type FXN. Class II variants, including R165C and N146K, demonstrate weak binding interactions (decreased 144-fold and 85-fold, respectively), but only modest impairment of activity (95% and 53% activity of wild-type, respectively). In contrast the Class III variant Q148R has only a modest 10-fold decrease in binding, but significantly reduced activation of the cysteine desulfurase (about 20% of wild-type activity). Finally the Class IV variants have only modest defects in binding and activation of the cysteine desulfurase, where I154F shows a 6-fold decrease in binding and 75% of wild-type activity. Given these classifications the FRDA L182F mutant, which exhibits wild-type binding and 91% activation of the cysteine desulfurase, belongs to the Class IV FXN mutants.

Although the results of Barondeau *et al* suggest that kinetic parameters play a primary role in the FRDA disease phenotype, two other factors have also been identified [57, 86, 92-94, 99-100]. The first involves disruption of the processing route of frataxin, either at the precursor (FXN^{1-210}) or intermediate (FXN^{42-210}) steps [57, 86, 100]. Impairment of this process has been demonstrated in several FRDA mutants, including

I154F, and is proposed to affect disease phenotype through reduced levels of mature protein. Additionally work by Gomes *et al* demonstrates that protein stability could play a role in the FRDA phenotype [93-94]. Although a difference of only 5 °C is observed between the melting temperature of wild-type FXN and W155R, a difference of more than 15 °C is observed for the D122Y, G130V, and I154F clinical mutants. Location of FXN residue L182 inside the protein core suggests that mutation of a hydrophobic leucine to a bulkier hydrophobic phenylalanine residue could have an impact on the overall protein stability [54, 101]. While this conservative mutation would not disrupt the hydrophobic nature of the protein core it could cause local distortion or rearrangement of the structure, which could alter the function of FXN. Furthermore despite eukaryotic conservation of a leucine at residue 182, in prokaryotes this residue is typically replaced by a phenylalanine which forms a π-π stacking interaction with a neighboring tryptophan [96]. The presence of W173 near the L182F mutation site could facilitate a similar π-π stacking interaction in this group of FRDA patients (Figure 2-7). Such an interaction in human FXN would require movement of the loop region connecting β_5 and α_2, which would disrupt the secondary structure of the protein.
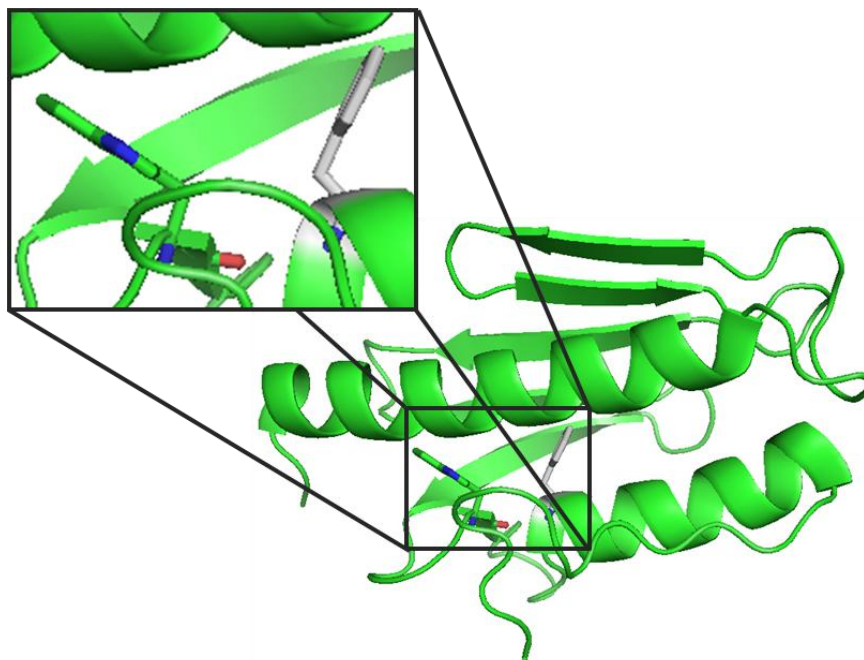
Figure 2-7. Structural model of the proposed π-π stacking interaction between tryptophan 173 and phenylalanine 182 in the FRDA L182F mutant. Model was made using the human FXN crystal structure residues 89-209 (PDB code: 3S4M).

Further investigation of the overall protein stability and secondary structure of all FRDA clinical mutants is required to fully assess the role of protein stability verses kinetic inhibition in disease phenotype. Initial extraction and refolding work with the insoluble L182H mutant shows promise for this technique for other FRDA mutants (G130V, W173G, and L156P) expressed as inclusion bodies with the Barondeau *et al* FXN construct [22]. However use of a His-tagged FXN construct (residues 91-210) should also been considered for these mutants, as soluble expression of the G130V mutant has been shown under these conditions [94]. Soluble, truncated expression of these mutations would allow for investigation of their protein stability and secondary structure, as well as their kinetic properties.

Initial work with the lysine acetylation mimics of K197 suggests that this residue does not impact interactions with the SDU complex. However the mouse frataxin homologue only contains three C-terminal lysine residues, while human FXN contains four (K192, K195, K197, and K208), suggesting the possibility that this post-translational modification is located at one of the other sites in the human system (Figure 2-8). As a result additional *in vitro* work is warranted to determine if lysine acetylation mimics, at these sites, perturb the FXN/SDU interaction or the interaction of FXN with the cluster transfer chaperones. Analysis of the alanine(A), arginine (R), and glutamine (Q) point mutations along with conversion of the cysteine mutant to an acetyl lysine mimic using previously published methods will allow for more in-depth analysis of the role of this post-translational modification [112-115].
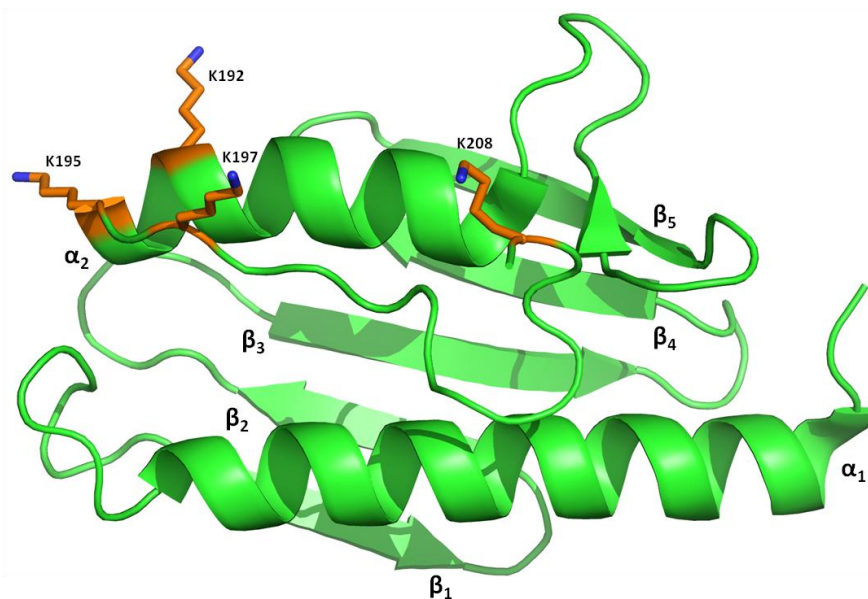
Figure 2-8. Crystal structure of human frataxin residues 89-209 (PDB code: 3S4M), with the four C-terminal lysine residues shown in orange.

CHAPTER III

ALANINE SCANNING OF THE FRATAXIN (FXN) SURFACE IDENTIFIES A

HOTSPOT FOR BINDING AND ACTIVATION WITH THE SDU COMPLEX

INTRODUCTION

Defects in the frataxin (FXN) protein have been shown to cause the

neurodegenerative disease Friedreich's Ataxia (FRDA), a progressive degenerative

disease of children and adolescents that ultimately leads to premature death [49-50, 84].

Large research efforts to define the function of FXN and develop therapeutic approaches

for the treatment of FRDA have been launched since the discovery of the link between

FRDA and the *FXN* gene in 1996. Unfortunately, these efforts have not resulted in an

effective FRDA therapy and the disease symptoms are often simply managed through

chelation therapy to restrict mitochondrial iron accumulation and antioxidant treatment

to limit ROS damage in patients [7, 16]. Although many roles have been proposed for

the frataxin family of proteins, emerging evidence suggests a regulatory role in Fe-S

cluster biosynthesis [22, 64, 82, 116]. FXN is required to interact with the Fe-S cluster

biosynthesis machinery to perform such a regulatory function. As mutations that

decrease these protein-protein interactions might be linked to FRDA, it is essential to

define these interactions both in terms of identifying frataxin binding partners and also

which residues on those proteins contribute to frataxin-based regulation.
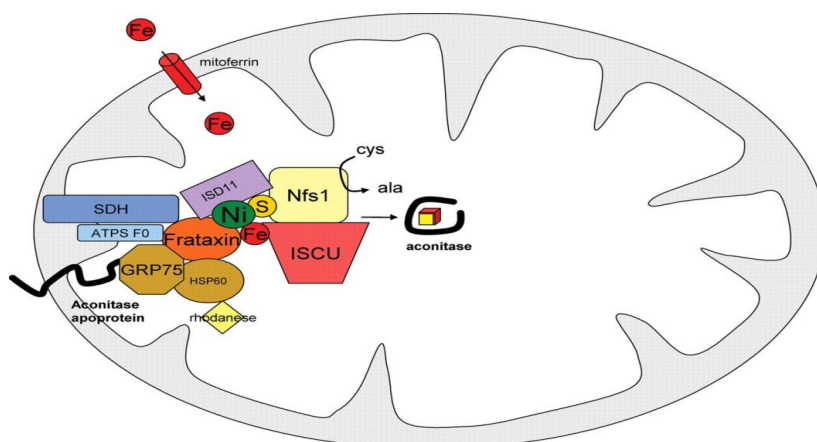
Figure 3-1. Cartoon representation of the protein-protein interactions between FXN and the components of the Fe-S cluster assembly system. Reprinted with permission from *Human Molecular Genetics*, 16(8): 929-941. Copyright 2007 Oxford University Press.

Immunoprecipitation and pull-down assays by Cortopassi and coworkers suggest FXN interacts with the core components of the human Fe-S cluster assembly system NFS1/ISD11 and ISCU; as well as with the chaperones GRP75, HSP60, and HSC20 (Figure 3-1) [45, 117]. Many of these protein-protein interactions have been confirmed by others in the yeast and *E. coli* Fe-S cluster assembly systems [55-56, 118]. This combined with the discovery by Barondeau *et al* and others of a functional four protein complex between FXN, NFS1/ISD11, and ISCU (named SDUF) provides validation to the role of frataxin in Fe-S cluster biosynthesis [22, 27-28]. Taken together these results suggest that FXN interacts with a preformed NFS1/ISD11/ISCU (SDU) complex, and interaction of FXN with this complex significantly increases the rate of the cysteine desulfurase and Fe-S cluster assembly on the scaffold protein. Small-angle X-ray scattering data and structural analysis of the analogous *E. coli* IscS/IscU/CyaY complex (IscS, IscU, and CyaY are homologs of human NFS1, ISCU, and FXN, respectively)

suggests that CyaY binds near the dimer interface of the cysteine desulfurase IscS, while

the scaffold protein IscU binds near the periphery of the IscS dimer (Figure 3-2) [119].

This arrangement not only allows for interaction of IscS with CyaY and IscU, but also

allows for interaction between IscU and CyaY.
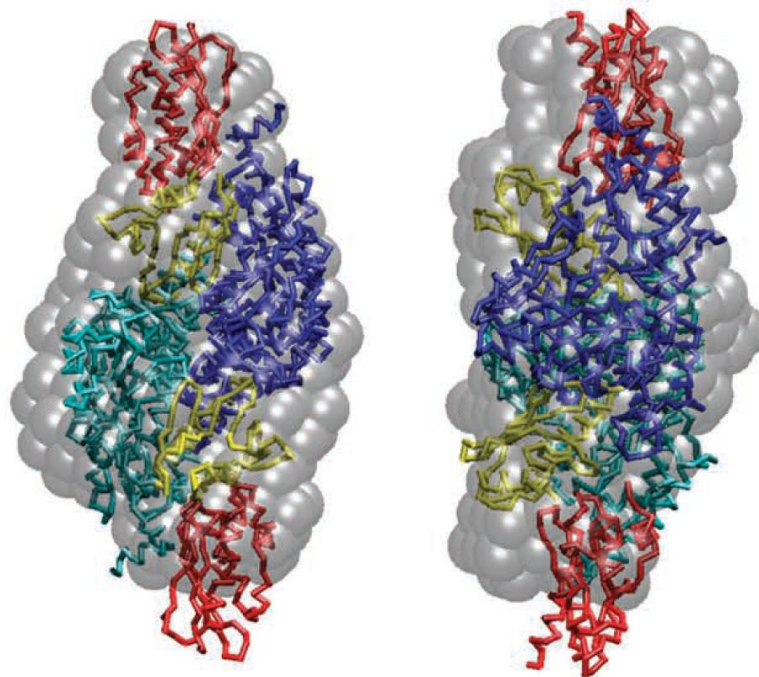
Figure 3-2. Molecular model of the CyaY/IscS/IscU complex from small-angle X-ray scattering data. Blue and green are the two halves of the IscS dimer, red is IscU, and yellow is CyaY. Reprinted with permission from *Nature Communications*, 1(7): 95-95. Copyright 2010 Nature Publishing Group.

Several attempts have been made to identify residues involved in the interaction

between FXN and either the intact SDU complex or components of the SDU complex.

Based on pull-down assays Cortopassi *et al* suggest an interaction between FXN and

ISD11 that is mediated through FXN residue I154 in the presence of nickel [117].

Mutation of the basic residues R220E/R223E/R225E on IscS or the acidic residues E18K/E19K/E22K on CyaY have been shown to disrupt the interaction of these two proteins, suggesting that the acidic ridge of the frataxin family serves as the binding surface for the cysteine desulfurase [119]. Further protein-protein interactions were observed by Stemmler *et al*, who demonstrated that several residues on yeast Yfh1 are perturbed upon addition of the yeast scaffold protein Isu1 (Figure 3-3) [120].

Figure 3-3. Residues perturbed by the addition of yeast Isu1 to apo-Yfh1. The structure of yeast Yfh1 is shown with labels for the corresponding human FXN residues. Reprinted with permission from *Biochemistry*, 49(40): 8756-8765. Copyright 2010 American Chemical Society Publications.

Pull-down assays of yeast Yfh1 mutants including N122K (human FXN_{N146K}), N122A/K123T/Q124A (human $FXN_{N146K/K147T/Q148A}$), and W131A (human FXN_{W155A}), suggest that the β-sheet region of the protein is involved in interactions with the yeast scaffold protein Isu1 and that W131 (human FXN_{W155}) is a hotspot for interaction [55-

56]. Furthermore *in vivo* studies of yeast Yfh1 by Foury *et al* suggest that Q129 (human FXN$_{Q153}$), W131 (human FXN$_{W155}$), and R141 (human FXN$_{R165}$) form a cluster of functionally important residues on the FXN surface, which could facilitate protein-protein interactions [55]. Pull-down assays by Puccio *et al* of 15 FXN mutants (Y95G, E96K, D104G, E108K, E111K, D115K, D122Y, D124K, G130V, N146A, N146K, I154F, W155A, W155R, & W173G) in the context of the SDU complex further confirmed and expanded upon the results seen in yeast and *E. coli*; identifying six mutants (E108K, E111K, D124K, N146K, W155A and W155R) that disrupted or abolished the FXN/SDU interaction (Figure 3-4) [27]. The negatively charged acidic patch residues E108, E111, and D124 are suggested to interact with the basic residues on NFS1/ISD11, while the N146 and W155 β-sheet residues are proposed to interact with ISCU. Furthermore the complete loss of interaction between SDU and the W155R mutant or the less severe W155A mutant support the findings in yeast that this residue is critical for interaction with ISCU. The available biochemical, structural, and pull-down assay data suggest regions of the FXN β-sheet and α$_1$ helix, which appear to be important in protein-protein interactions with SDU (Figure 3-4). Here we build upon these results to quantitate the FXN side-chain contributions for binding to the SDU complex and also establish the functional importance of FXN side-chains for the activation of the Fe-S assembly complex. These experiments provide vital information towards the design of peptidomimetics as a FXN replacement strategy and potential FRDA therapeutic.
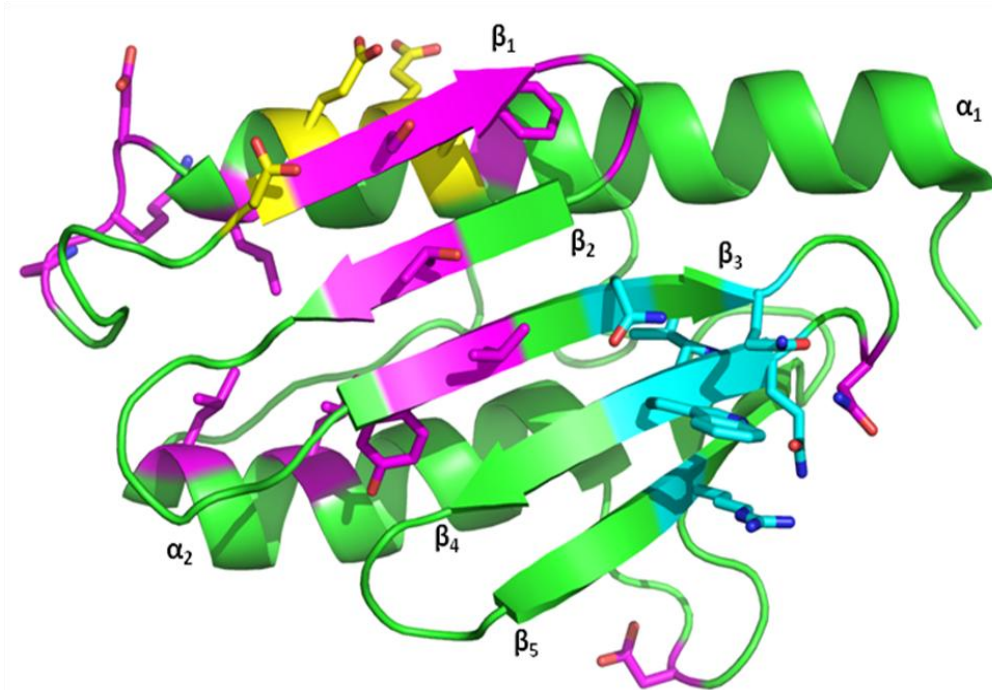
Figure 3-4. Crystal structure of human frataxin residues 89-209 (PDB code: 3S4M) showing residues proposed as the site for NFS1/ISD11 (yellow) and ISCU (cyan) binding and the residues perturbed in yeast Yfh1 upon addition of Isu1 (magenta).

EXPERIMENTAL PROCEDURES

Protein Preparation. The point mutations (S105A, L106A, D115A, K116A, P117G, Y118A, T119A, S126A, K135A, T142A, D178A, L190A, K195A) were introduced into a pET11a plasmid containing a codon optimized human *FXN* gene (FXN Δ1-55), lacking the first 55 amino acids, using the QuikChange method (Stratagene) [22]. Presence of the mutation was confirmed by DNA sequencing, performed by the Texas A&M University Gene Technology Laboratory. The plasmids containing each mutant were transformed into *E. coli* BL21(DE3) competent cells and grown at 37 °C, until an OD_{600} of ~0.7 was obtained. Protein expression was then induced with 0.5 mM isopropyl β-D-1-thiogalactopyranoside (IPTG), and cells were incubated at 16 °C for 16 hours. The cells were then harvested by centrifugation and lysed by sonication (Branson Sonifier 450) in 50 mM Tris pH 7.5. The supernatant was loaded onto an anion exchange column (26/20 POROS 60HQ, Applied Biosystems) and eluted with a linear gradient from 0 to 800 mM NaCl in 50 mM Tris pH 7.5. The fractions corresponding to monomeric frataxin were collected, concentrated, and loaded onto a Sepharcyl S100 (26/60, GE Healthcare) size exclusion column equilibrated with 50 mM HEPES, 150 mM NaCl pH 7.5. Protein concentrations for each mutant were calculated using their absorbance at 280 nm with an extinction coefficient of 26030 $M^{-1}cm^{-1}$ used for all mutants, except Y118A ($\varepsilon = 24750$ $M^{-1}cm^{-1}$) [108]. The ISCU2 and NFS1/ISD11 proteins were purified as previously described and their protein concentrations determined using extinction coefficients of 10,900 $M^{-1}cm^{-1}$ (PLP) and 8250 $M^{-1}cm^{-1}$ at wavelengths of 420 nm and 280 nm, respectively [22, 108].

Cysteine Desulfurase Activity Measurements. The number of equivalents of each

FXN variant required to saturate the cysteine desulfurase activity was determined by

titrating increasing amounts of each FXN variant into a standard reaction mixture, as

previously described with a final volume of 800 µL [22, 92, 99, 109-110]. Once the

saturating about of each variant was determined reaction mixtures containing 0.5 µM

NF$\underline{S}$1/IS$\underline{D}$11 (SD), 1.5 µM ISCU2, the saturating amount of FXN (or FXN point

mutant), 10 µM pyridoxal-5'-phosphate (PLP), 2 mM dithiothreitol (DTT), 5 µM

Fe(NH$_4$)$_2$(SO$_4$)$_2$, and 50 mM Tris, 250 mM NaCl pH 8.0 were incubated for 30 minutes

in an anaerobic glovebox at ~14 °C [22]. The cysteine desulfurase reaction was initiated

with the addition of 100 µM L-cysteine at 37 °C, and quenched with 100 µL each of 20

mM *N,N*-dimethyl-*p*-phenylenediamine in 7.2 N HCl and 30 mM FeCl$_3$ in 1.2 N HCl.

Following 20 minute incubation at 37 °C and centrifugation for 5 minutes at 12,000 rpm,

the methylene blue formation was measured at 670 nm and converted to sulfide

production using a Na$_2$S standard curve. The rate is expressed in units of mol sulfide per

mol SD per minute at 37 °C.

Michaelis-Menten Kinetics for Frataxin Variants in SDUF Complex. To a

standard reaction mixture of 0.5 µM (SD), 1.5 µM ISCU2, 10 µM pyridoxal-5'-

phosphate (PLP), 2 mM dithiothreitol (DTT), 5 µM Fe(NH$_4$)$_2$(SO$_4$)$_2$, and 50 mM Tris,

250 mM NaCl pH 8.0 was added the saturating amount of the FXN mutants [92, 99].

Reactions were incubated for 30 minutes in an anaerobic glovebox before being initiated

with the addition of 12.5 - 600 µM L-cysteine. The rate of cysteine desulfurase activity

was analyzed as above. The reaction rates were plotted verses L-cysteine concentration

and fit with the Michaelis-Menten equation in KaleidaGraph. The k_{cat} was determined at varying FXN concentrations and used to determine the binding constant of FXN to the SDU complex. These results were fit as a type II allosteric activator using Eq. 3-1 in KaleidaGraph, where the [SDUF] is calculated as shown in Eq. 3-2 [32].

$$k_{obs} = \frac{k_{SDU}([SDU]_{total} - [SDUF]) + k_{SDUF}^{\infty}[SDUF]}{[SDU]_{total}}$$

(Eq. 3-1)

$$[SDUF] = \frac{[SDU]_{total} + [FXN]_{total} + K_d - \sqrt{([SDU]_{total} + [FXN]_{total} + K_d)^2 - 4[SDU]_{total}[FXN]_{total}}}{2}$$

(Eq. 3-2)

Cysteine Desulfurase Activity of SDU in the Presence of Tryptophan. To a standard reaction mixture of 0.5 μM (SD), 1.5 μM ISCU2, 10 μM pyridoxal-5'-phosphate (PLP), 2 mM dithiothreitol (DTT), 5 μM Fe(NH$_4$)$_2$(SO$_4$)$_2$, and 50 mM Tris, 250 mM NaCl pH 8.0 was added 0 – 40 mM L-Tryptophan [22, 109-110]. Reactions were incubated for 30 minutes at 14 °C in an anaerobic glovebox before the reactions were initiated with the addition of 100 μM L-cysteine. The reactions were quenched and the cysteine desulfurase activity was analyzed as above. The rate is expressed in units of mol sulfide per mol SD per minute at 37 °C.

RESULTS

Residues of the β-sheet Impair Interactions with the Fe-S Cluster Assembly Complex. A total of 35 alanine or glycine (used for proline residues) point mutants; including S105A, L106A, D115A, K116A, P117G, Y118A, T119A, S126A, K135A, T142A, D178A, L190A, and K195A, were expressed in *E. coli* and purified to >95% homogeneity (Figure 3-5). During the protein purification process the Δ1-55 FXN construct spontaneously truncated to produce the mature (FXN$^{81-210}$) form of the protein [32, 111]. The number of equivalents necessary to saturate the cysteine desulfurase activity of each mutant was determined; with activity saturating at 3eq for WT, 10eq for S105A, 3eq for L106A, 25eq for D115A, 10eq for K116A, 5eq for P117G, 10eq for Y118A, 3eq for T119A, 3eq for S126A, 3eq for K135A, 10eq for T142A, 5eq for D178A, 5eq for L190A, and 10eq for K195A. The ability of the alanine scanning mutants to stimulate the cysteine desulfurase activity of the SDU complex was investigated using saturating amounts of each mutant and the physiologically relevant cysteine concentration of 100 μM [22]. The cysteine desulfurase activity of 32 mutants was determined through a collaborative effort by Melissa Thorstad, Nicholas Fox, and Jennifer Rabb (Figure 3-6).
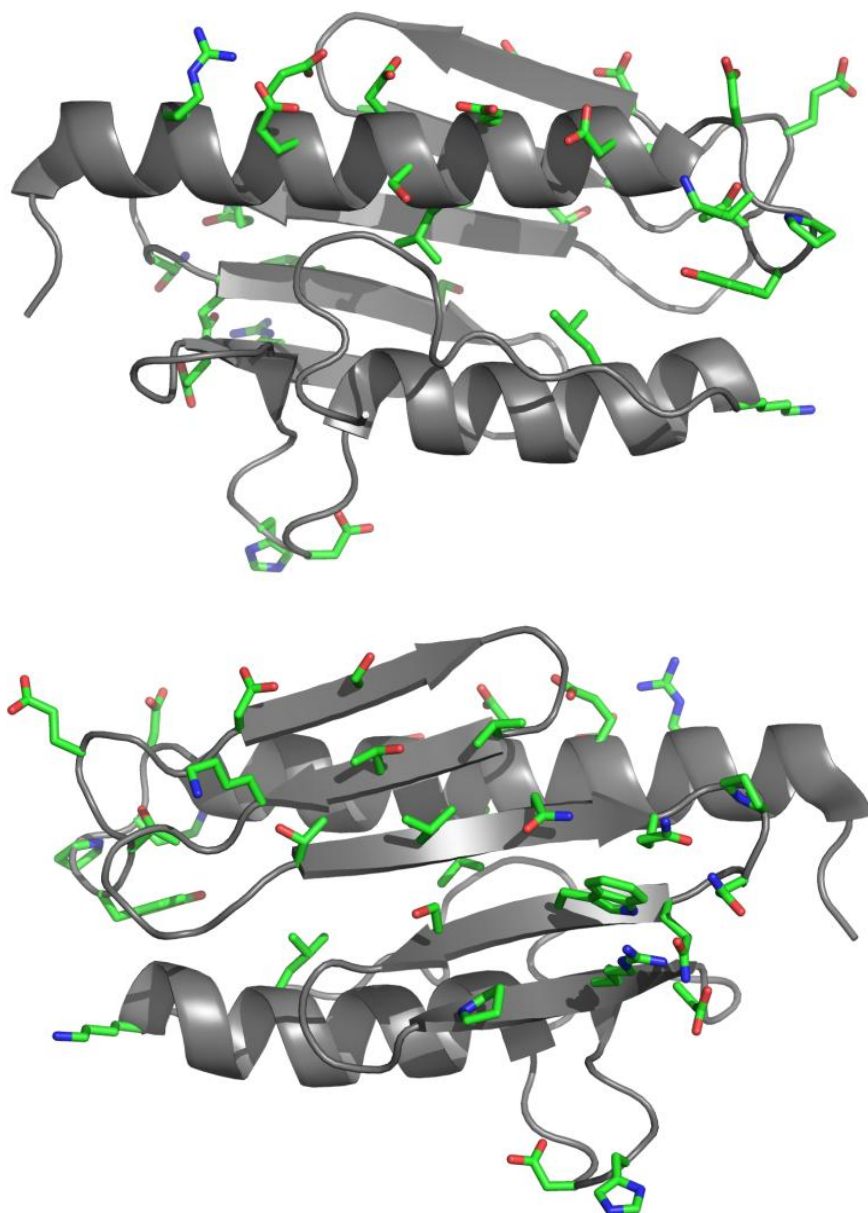
Figure 3-5. Crystal structure of human frataxin residues 89-209 (PDB code: 3S4M), viewed from the α-helices (top) and the β-sheet (bottom) regions. Residues mutated in the alanine scanning investigation are indicated as stick models.
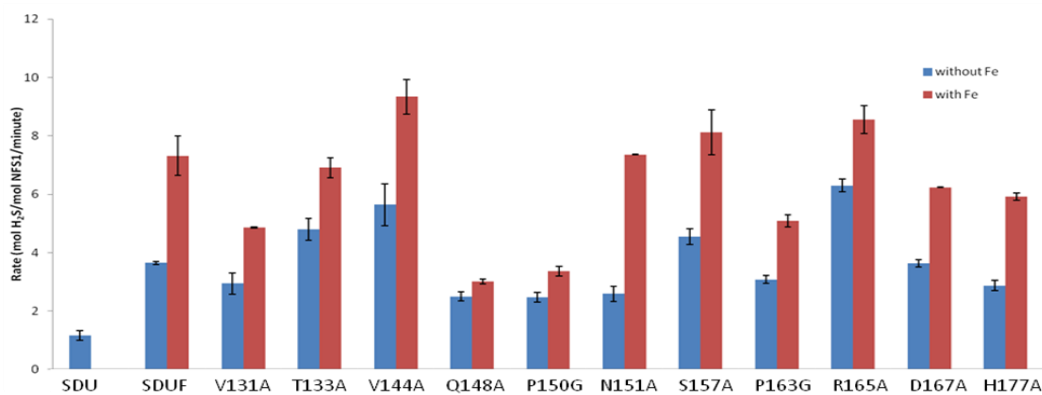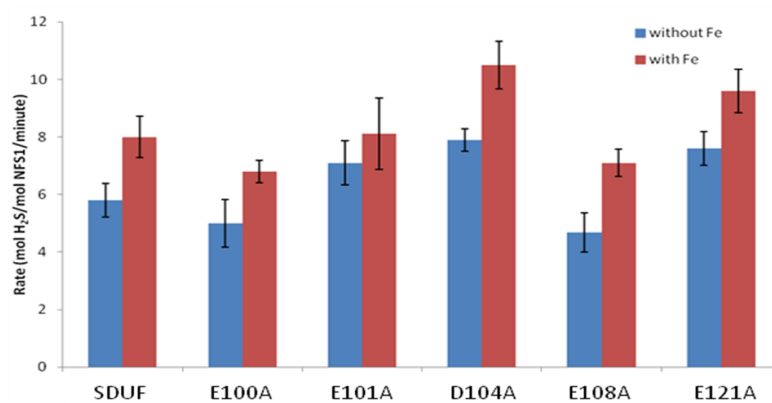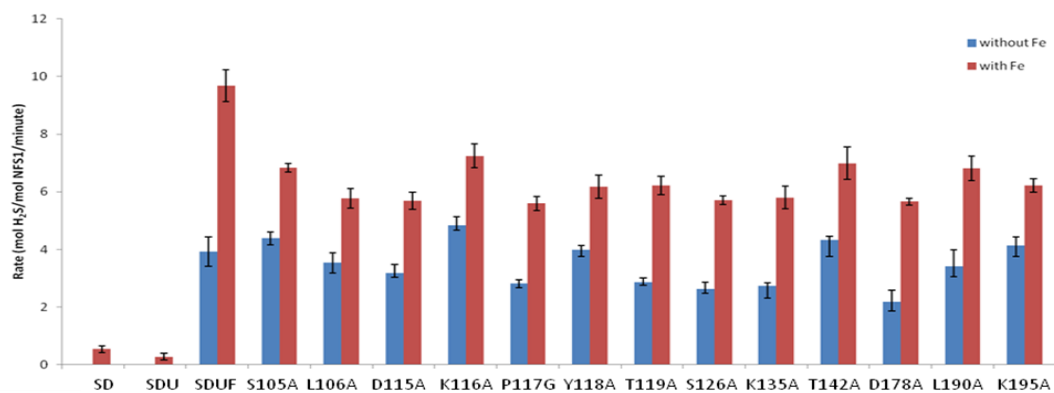
Figure 3-6. Bar charts of the cysteine desulfurase activity of the FXN alanine scanning mutants investigated by Melissa Thorstad (top), Nicholas Fox (middle), and Jennifer Rabb (bottom). Mutants with significantly impaired cysteine desulfurase rates are N146, Q148, P150, Q153, W155, and R165. Blue bars represent samples without ferrous iron and red bars are in the presence of ferrous iron.

Mapping Frataxin Binding & Activity Interactions with the Fe-S Cluster

Assembly Complex. Michaelis-Menten parameters for all 35 alanine scanning mutants

were determined through the collaborative efforts of Melissa Thorstad, Nicholas Fox,

and Jennifer Rabb (Table 3-1). The Michaelis-Menten parameters k_{cat} and K_M were

determined for all 35 mutants, using the cysteine desulfurase activity at saturating FXN

variant levels. The data was fit using KaleidaGraph, as shown for the 13 mutants studied

by Melissa Thorstad (Figure 3-7). The binding constants for all 35 alanine scanning

mutants were determined by plotting the k_{cat} verses FXN variant concentration and

fitting the data with Eq. 3-1 in KaleidaGraph. Data for the 13 mutants investigated by

Melissa Thorstad is provided (Figure 3-8).
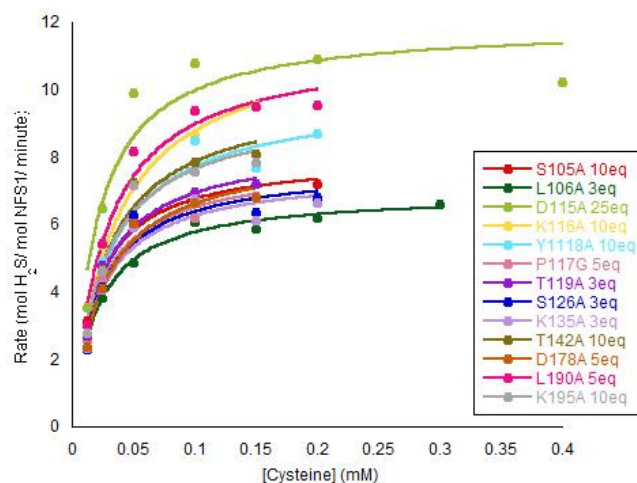
Figure 3-7. Determination of the Michaelis-Menten parameters k_{cat} and K_M for FXN variants: S105A(red), L106A(green), D115A(lime), K116A(yellow), Y118A(cyan), P117G(pink), T119A(purple), S126A(blue), K135A(lavender), T142A(olive), D178A(orange), L190A(magenta), K195A(gray). The methylene blue assay rates were determined at saturating FXN variant and varied cysteine concentrations. The data was fit in KaleidaGraph with the Michaelis-Menten equation. The R^2 values are 0.98 (S105A), 0.99 (L106A), 0.88 (D115A), 0.99 (K116A), 0.97 (P117G), 0.96 (Y118A), 0.98 (T119A), 0.92 (S126A), 0.92 (K135A), 0.96 (T142A), 0.96 (D178A), 0.96 (L190A), and 0.95 (K195A).

Table 3-1. Kinetic parameters for SDU with FXN alanine scanning variants.

FXN Variants	K_{cat} (min^{-1})	K_M (mM)	K_{cat}/K_M (M^{-1} s^{-1})	K_d (uM)
R97A[1]	10.3	0.018	9500	7.87
E100A[1]	7.8	0.014	9100	0.05
E101A[1]	9.1	0.025	6200	0.23
D104A[1]	11.3	0.026	7300	0.65
S105A	8.0	0.019	7100	0.03
L106A	6.9	0.020	5800	0.03
E108A[1]	8.7	0.020	7200	0.28
D112A[1]	12.6	0.030	7100	0.42
D115A	11.9	0.019	10000	0.22
K116A	11.6	0.032	6000	0.09
P117G	7.8	0.020	6400	0.14
Y118A	9.8	0.028	5900	0.20
T119A	8.4	0.021	6500	0.05
E121A[1]	7.0	0.010	12000	0.11
D124A[1]	7.0	0.016	7300	1.75
S126A	7.7	0.021	6100	0.0008
V131A[2]	6.4	0.023	4600	0.10
T133A[2]	9.2	0.021	7300	0.49
K135A	7.6	0.021	6000	0.06
T142A	9.9	0.026	6200	0.53
V144A[2]	8.1	0.021	6400	0.15
N146A[2]	4.0	0.019	4700	1.14
Q148A[2]	2.9	0.012	4000	0.46
P150G[2]	7.1	0.014	8500	0.75
N151A[2]	7.9	0.027	5000	1.06
Q153A[2]	2.4	0.014	2900	7.22
W155A[2]	3.9	0.012	5600	5.85
S157A[2]	7.6	0.018	7000	0.24
P163G[2]	7.5	0.018	6900	1.26
R165A[2]	7.9	0.020	6600	14.29
D167A[2]	8.1	0.020	6800	0.19
H177A[2]	7.3	0.020	6100	0.04
D178A	8.2	0.025	5500	0.14
L190A	11.3	0.026	7200	0.10
K195A	9.5	0.025	6400	0.05

Mutants investigated by Melissa Thorstad (no superscript), Nicholas Fox (1), Jennifer Rabb (2).
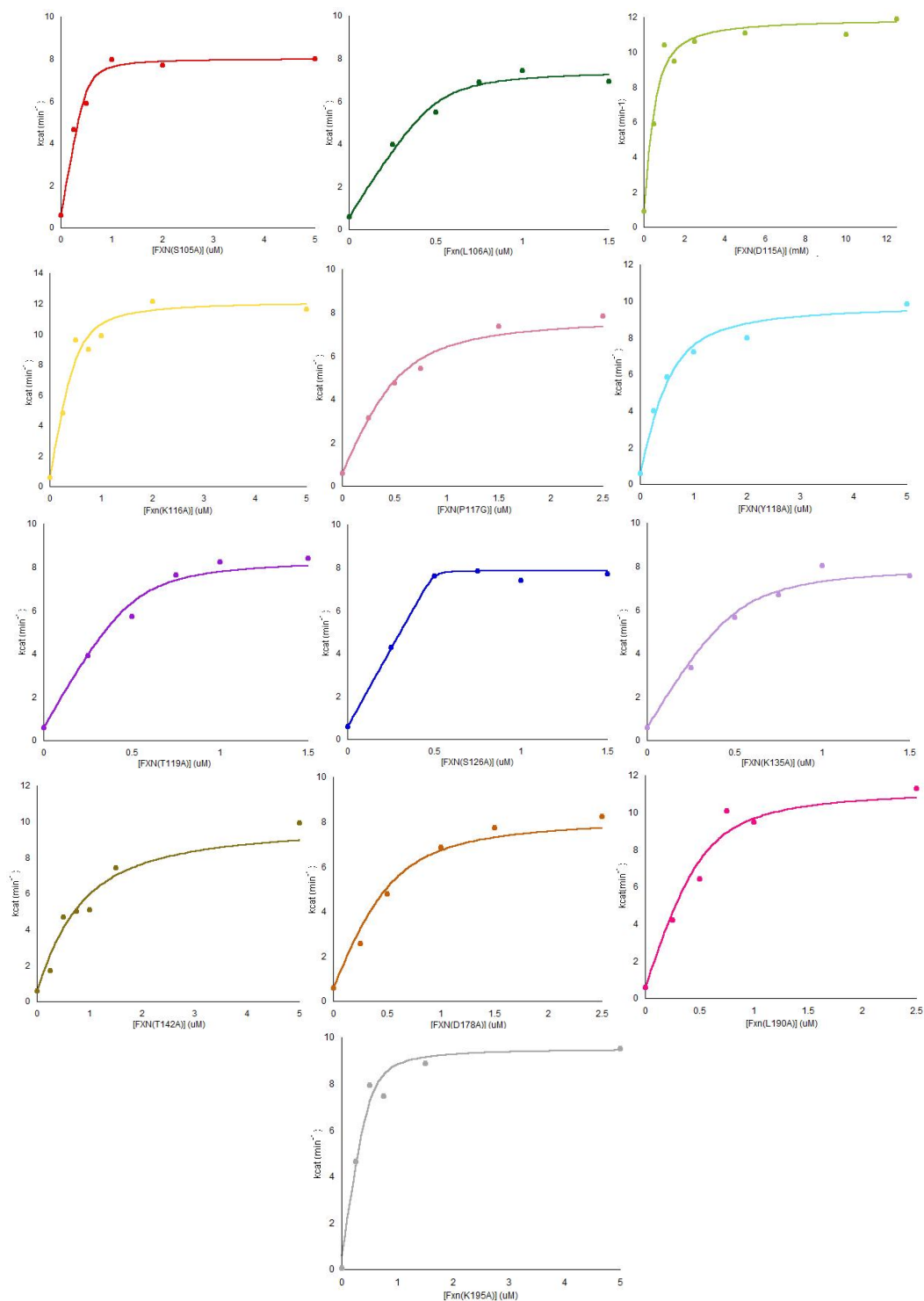
Figure 3-8. Determination of the binding constants for FXN variants: S105A (red), L106A (green), D115A (lime), K116A (yellow), P117G (pink), Y118A (cyan), T119A (purple), S126A (blue), K135A (lavender), T142A (olive), D178A (orange), L190A (magenta), and K195A (gray). Data was fit in KaleidaGraph using Eq. 3-1.

49

Tryptophan Alone Does Not Activate the SDU Complex. The cysteine

desulfurase activity of the SDU complex in the presence of L-Tryptophan was

determined to be equivalent to that of SDU (Figure 3-9).
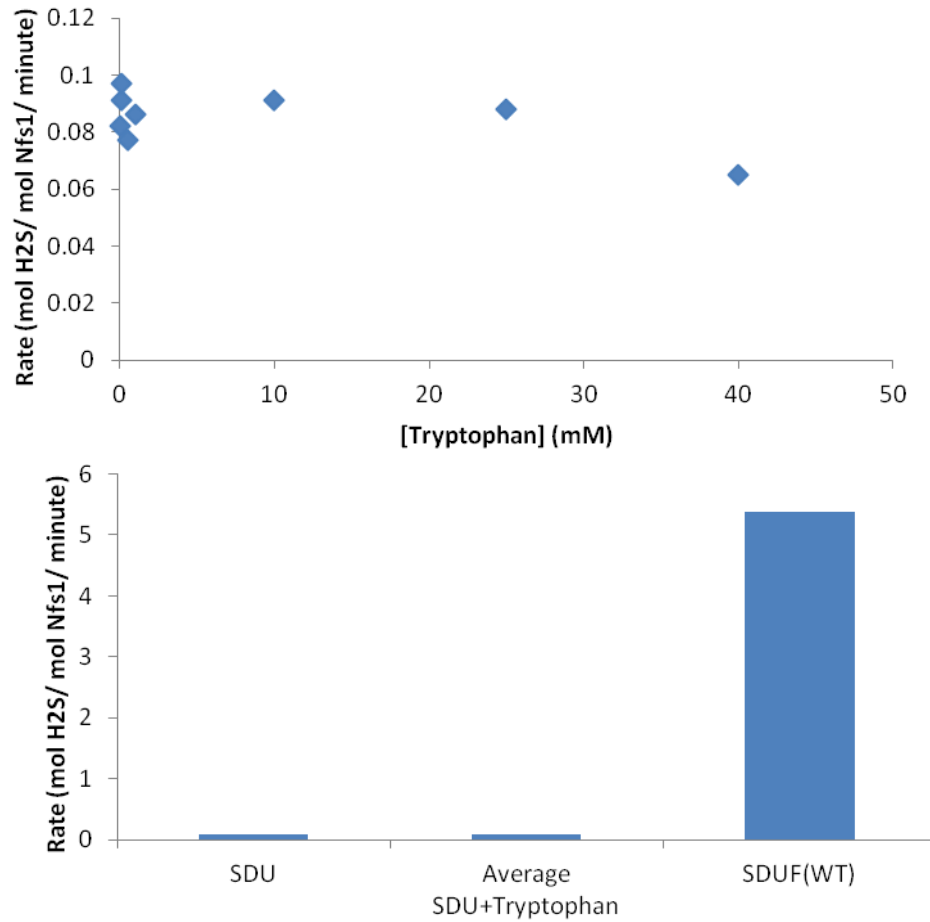
Figure 3-9. Titration of L-Tryptophan with SDU (top) and bar chart of the averaged
cysteine desulfurase activity of SDU with L-Tryptophan (bottom).

DISCUSSION

Protein-protein interactions between FXN and the SDU complex have been demonstrated in the yeast, *E. coli*, and human systems; where interactions with ISCU and NFS1/ISD11 are proposed to occur through the FXN β-sheet and α_1-helix, respectively [22, 27, 55-56, 92, 99, 117, 120-121]. However, only limited information is known about the specific residues of interaction and the kinetic implications of these interactions. While attempts have been made to identify residues involved in the FXN/SDU interaction through loss of SDU pull-down or NMR amide backbone perturbation analysis, to our knowledge this is the first attempt to assess the functional importance of individual FXN residues to map the surface of interaction using the SDU complex *in vitro*.

Examination of the kinetic parameters of the 35 point mutants suggests a hotspot for FXN interaction with SDU through the β_4 and β_5 sheets. Combination of alanine scanning with functional assessment through the cysteine desulfurase assay, identified 14 residues of the FXN α_1 helix and β-sheets with significantly to moderately inhibited SDU binding or activation. Comparison of the cysteine desulfurase activity at saturating amounts of frataxin, suggests that the β-sheet residues N146, Q148, P150, Q153, W155, and R165 are important for either activation or binding of SDU. Drastic binding defects were observed upon mutation of the FXN residues R97, Q153, W155, and R165 to alanine, while moderate impairment was seen for six FXN residues (D104, D124, N146, P150, N151, and P163) of the α_1 helix and β-sheet regions (Figure 3-10). Significant activation defects of the SDU complex were found upon mutation of four residues

51

(N146, Q148, Q153, and W155) of the FXN β-sheet, with five additional residues

(L106, E121, D124, V131, and P150) showing modest activation defects (Figure 3-10).
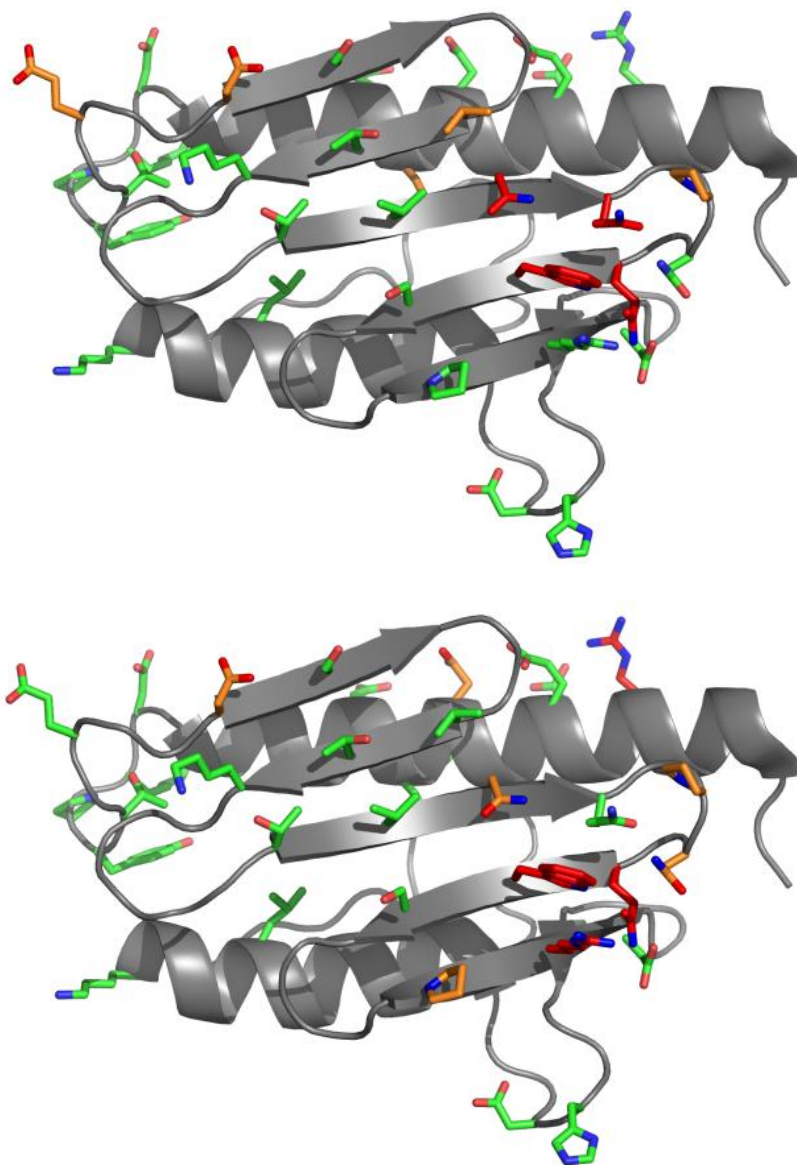
Figure 3-10. Plots of FXN residues involved in activation (top) or binding (bottom) of SDU. Residues shown in red and orange are significantly or moderately impaired, respectively. Green residues have essentially wild-type character.

Impairment of the binding and/or activation of the FXN residues N146, Q148, Q153, W155, and R165 is consistent with previous findings by Barondeau et al [82, 99]. Furthermore pull-down assays in the yeast and human system support the findings that W155 and N146 are important for SDU interaction [27, 55-56]. The NMR studies of Stemmler et al, showing perturbation of FXN residues Q148 and N151 in the presence of Isu1 support the role of these amino acids in SDU interactions [120]. Additionally the presence of FRDA clinical mutants at residues L106, N146, Q148, W155, and R165 provides further support for the importance of these residues in the proper in $vivo$ function of FXN [84]. While disruption of the protein secondary structure cannot be ruled out as a factor for the kinetic defects of the P150G and P163G mutants, lack of such effects with the other proline residue (P117) studied here suggests that these β-sheet residues play a role in the binding or activation of SDU. Despite the presence of modest binding or activation defects in three of the acidic patch residues (D104, E121, and D124), the level of impairment is significantly lower than expected for mutation of the iron binding site of an iron donor protein; thus further supporting the allosteric activator role of FXN previously proposed by Barondeau et al [22].

This improved understanding of FXN/SDU interactions must be considered in the development of new treatments for FRDA. Identification of the localized binding and activation hotspot on the β_4 and β_5 sheets of FXN (residues N146, Q148, Q153, W155, and R165), suggests that future drug design should be targeted to this region of the protein. In addition to the use of commercially available small molecule screening kits, the design of small cyclic peptides should be used to target the FXN hotspot. Since

W155 and R165 appear to be the most important residues for activating and binding SDU, respectively, they should be included in cyclic peptide design. However addition of tryptophan to SDU demonstrates that the activation process requires more than this single amino acid. Additionally further investigation of the FXN(S126A) mutant should be performed, as it appears to bind SDU about ~100-fold tighter than wild-type FXN. Finally this bank of FXN alanine scanning mutants should also be applied to elucidating the FXN residues involved in interactions with the cluster transfer proteins.

CHAPTER IV

INVESTIGATION OF OLIGOMERIC FXN[56-210]

INTRODUCTION

Over the course of the past 13 years, much work has been done to investigate the oligomerization properties of three members of the frataxin family yeast Yfh1, *E. coli* CyaY, and human FXN [122]. Initial characterization of the three homologues shows that although they are all composed of monomeric subunits with similar secondary structures, their oligomerization propensities and properties are vastly different (Table 4-1) [123].

Table 4-1. Oligomeric properties of ferritin, yeast Yfh1, *E. coli* CyaY, and human FXN.

	Ferritin	Yeast Yfh1	*E. coli* CyaY	Human FXN
Assembled during Protein Expression	Yes	No	No	Yes
Stepwise Assembly Process *In vitro* with Iron	No	Yes	Yes	No
Assembles under Aerobic Conditions	ND	Yes	Fe^{2+} - monomer, intermediate, & large oligomers / Fe^{3+} - monomer & large oligomers	ND
Assembles under Anaerobic Conditions	ND	No	Forms tetramer	ND
Assembly Reversible with Metal Chelators	No	Yes	Yes	No
Monomer Present upon Assembly Completion	ND	20%	Yes	Yes
Diameter of Oligomeric Assembly	12-13 nm	180-190 Å	ND	16 nm spheres & chains of these spheres
Oligomeric Building Block	monomer composed of H- & L-subunits	trimer	tetramer	monomer
Iron Binding Capacity per Monomer	ND	50-75 for 24mer	≤ 26 for dimer to pentamer species	6-10 for preassembled oligomer
Overall Iron Storage Capacity	≤ 4500 for 24mer	> 3000 for 24mer	ND	ND
Iron Core Chelatable with Metal Chelators	Yes	Requires reducing agents	Yes	Requires reducing agents
Ferroxidase Activity	Yes	For $\alpha \rightarrow \alpha_3$ step	First 6 iron atoms	Fe(II)/monomer ratios ≤ 0.75
Autoxidation Activity	Yes	For $\alpha_3 \rightarrow \alpha_6 \rightarrow \alpha_{12} \rightarrow \alpha_{24} \rightarrow \alpha_{48}$ steps	After addition of first 6 iron atoms	Fe(II)/monomer ratios > 0.75
Diameter of Mineral Core	7-8 nm	1-2 nm	ND	smaller than Yfh1 core
Involved in Fe-S Cluster Assembly	No	Using only Fe^{3+}	Yes	With both Fe^{2+} and Fe^{3+}

Properties of the iron-binding protein ferritin were obtained from a review by Arosio *et al* [124].

Due to the variability in the N-terminus of the frataxin family of proteins, this region has been suggested to play a role in mediating the oligomerization properties [111, 125]. Two primary roles have been suggested for oligomeric forms of the frataxin family [116, 122-123]. Initially a role as an iron storage protein, similar to that of the iron storage protein ferritin, was proposed. More recently due to findings that monomeric frataxin homologues interaction with components of the Fe-S cluster biosynthesis machinery, a similar role has also been proposed for the oligomeric variants.

Extensive work has been done by Isaya *et al* on the assembly process, ferroxidase activity, and particle structure of Yfh1 oligomers. Based on this Yfh1 assembly appears to occur through the stepwise assembly process $\alpha \rightarrow \alpha_3 \rightarrow \alpha_6 \rightarrow \alpha_{12} \rightarrow \alpha_{24} \rightarrow \alpha_{48}$, where the addition of Fe(II) to the monomeric species induces trimer formation and it is these trimers that serve as the building blocks for the formation of the larger order oligomers (heaxmers, dodecamers, 24-mers, and 48-mers), with α_{60} and α_{96} species also having been observed [69, 126-127]. Formation of a dimer-type intermediate (α^*) between the $\alpha \rightarrow \alpha_3$ transition has also been proposed, and possibly represents the rate limiting step for oligomer assembly in Yfh1(WT) [127]. Additionally Yfh1 oligomerization has been found to be inhibited under anaerobic conditions, suggesting that in addition to Fe(II), O_2 may also be essential for this process [75]. Furthermore, recent findings suggest that initiation of Yfh1 oligomerization can be facilitated by Co^{2+} and glycerol, where the addition of these to Yfh1 solution results in an increased level of dimers, trimers, and hexamer species [125]. Several iron-independent oligomeirization mutations in the N-terminus of the protein have been

identified; however recent findings suggest that these mutants have decreased stability and processing of Yfh1 *in vivo* [127-128]. The ferroxidase activity and structure and composition of the Yfh1 iron core have been investigated with electrode oximetry, EXAFS, and electron microscopy [66, 69, 73, 75, 125-130]. The ferroxidase activity has been suggested to occur around the 3-fold axis of the trimer and result in the formation of a ferrihydrite mineral similar to that seen in the iron storage protein ferritin [75, 129]. Yfh1 has been shown to bind between 50-75 iron atoms within its ferrihydrite core, with the larger oligomers capable of storing more than 3000 iron atoms [126, 129]. Several mutations have been identified which limit the ferroxidase activity, while still allowing for oligomerization; suggesting Yfh1 has an affinity for autoxidation of Fe(II) even in the absence of its ferroxidation sites [66, 131]. Furthermore, the ferrioxidase activity has been suggested to facilitate a role for Yfh1 in mediating ROS and oxidative damage [66]. Based on electron microscopy and Fe K near-edge X-ray absorption spectroscopy, the iron core of the Yfh1 oligomers appears to be about 1-2 nm in diameter and composed of a similar dinuclear bridging binding site to that seen in ferritin [73, 126]. Electrode oximetry suggests that the mineral core is formed in a two step process with ferroxidase activity occurring as a slower step during the conversion of monomer to trimer ($\alpha \rightarrow \alpha_3$), followed by a faster autoxidation step once the trimer is converted to larger order oligomers ($\alpha_3 \rightarrow \alpha_6 \rightarrow \alpha_{12} \rightarrow \alpha_{24} \rightarrow \alpha_{48}$) [75, 129]. Additionally regardless of the iron concentrations used, about 20% of the sample remains as monomer even upon completion of the assembly process. Finally electron microscopy and X-ray crystallography have been used to investigate the trimer and 24-mer structures [125, 128,

130-131]. Three crystal structures of the Yfh1 trimer have been determine, one apo and two holo, with one containing iron and the other cobalt in the proposed iron binding site at the 3-fold axis (Figure 4-1) [125, 128, 131].

Figure 4-1. Crystal structure of the Yfh1 trimer, viewed down the 3-fold axis (PDB code: 3OEQ).

Based on these structures, the Yfh1(Y73A) trimer is stabilized by interactions between the N-termini of the three monomeric subunits. Based on the electron microscopy reconstructions of the 24-mer, the trimer serves as the building block of this structure with the overall assembly having a diameter of 180-190 Å (Figure 4-2) [128, 130]. More recently, oligomeric Yfh1 has been suggested to interact with Nfs1/Isd11 and Isu1 of the yeast system forming a complex capable of producing Fe-S clusters on Isu1 [76, 127, 132]. Combining the evidence for an iron storage function for Yfh1 with its apparent role in Fe-S cluster biosynthesis, Isaya *et al* has proposed a dual iron storage/ ISC biosynthesis function for Yfh1.
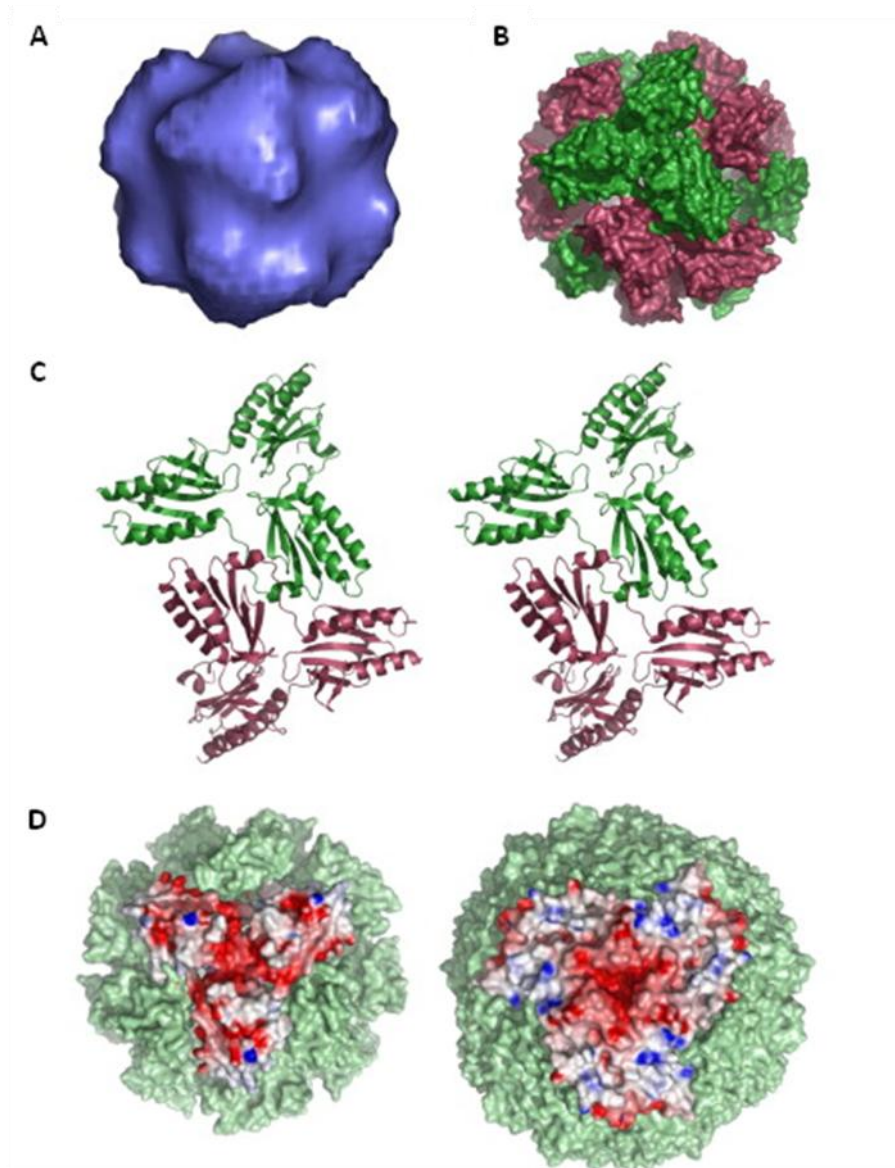
Figure 4-2. Electron microscopy (EM) model of Yfh1 24-mer. (A) EM reconstruction of Yfh1 24-mer viewed along the 2-fold axis of trimer. The oligomer is composed of eight trimer units. (B) Docking of trimer structure into the EM reconstruction with the trimers shown as surface representations (green and purple). (C) Stereoview of interactions between the N-termini of neighboring trimers in the 24-mer. (D) Surface representations of Yfh1 (left) and horse-spleen ferritin (right) 24-mers along the 3-fold axis. The trimer subunits are colored based on the electrostatic potentials of their surfaces. Reprinted with permission from *Structure*, 14(10): 1535-1546. Copyright 2006 Cell Press.

Similar to Yfh1 in the absence of iron CyaY exists as a single discrete monomeric species; however, in the presence of iron the assembly process of CyaY is much less complete than that of Yfh1 and appears to proceed through multiple mechanisms [70, 123]. In the presence of ferric iron, only monomeric and high molecular weight species were observed, with the high molecular weight species containing up to 8 iron atoms/monomer. Under anaerobic conditions in the presence of Fe(II), only a gradual shift from monomer to tetramer is observed, where the tetramer which binds two Fe^{2+}/protein has been proposed as the primary building block for assembly of larger order oligomers (Figure 4-3) [70, 123, 131]. In contrast size exclusion and analytical ultracentrifugation (AUC) data in the presence of Fe(II) and either O_2 or H_2O_2 indicate that CyaY assembles as a heterogeneous mixture of states primarily composed of monomer, intermediate dimer to pentamer, and larger oligomers with molecular weights above 600 kDa (Figure 4-4) [70, 123]. While the monomer is iron free, the intermediate form contains up to 26 iron atoms/monomer [70, 133]. The iron content of the larger oligomers could not be determined, as they precipitate after isolation [123]. Further analysis of this assembly mechanism revealed that much like Yfh1, the distribution of assembly species is dependent on the protein to iron ratio, with a mixture of monomer and intermediate present at a 1:1 ratio followed by increasing amounts of intermediate and high molecular weight oligomeric species, until protein precipitation occurs at a protein to iron ratio of 1:60.
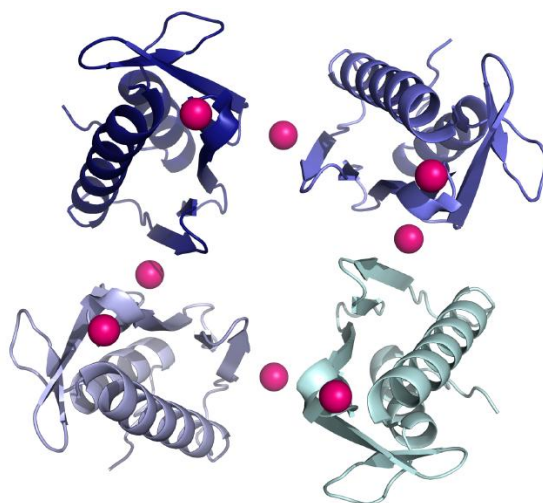
Figure 4-3. Ribbon diagram of the CyaY tetramer structure modeled from small-angle X-ray scattering (SAXS) data of CyaY after incubation with ferrous ammonium sulfate $[Fe(NH_4)_2(SO_4)_2]$. The Co^{2+} ions bound to the CyaY monomer crystal structure (PDB entry 2EFF) are shown in magenta. Reprinted with permission from *Journal of Biological Chemistry*. Copyright 2013 American Society for Biochemistry and Molecular Biology.
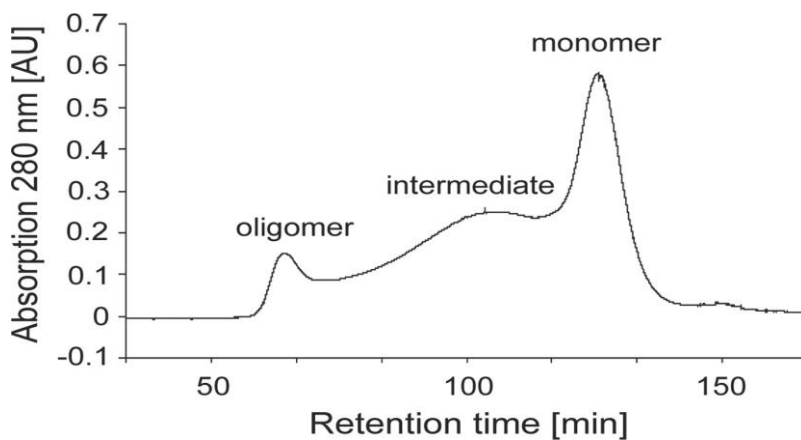
Figure 4-4. Oligomeric forms of iron-loaded CyaY. Apo CyaY was incubated with iron and the oligomeric species distribution was analyzed by Superdex 200 gel filtration chromatography. Reprinted with permission from *Journal of Biological Chemistry*, 281(24): 16256-16263. Copyright 2006 American Society for Biochemistry and Molecular Biology.

Furthermore oxidation of Fe(II) appears to be non-enzymatic, as the first six Fe(II) ions added had distinct reaction properties from those added subsequently [70]. This suggests that following the addition of the first six iron atoms, further mineralization proceeds not through ferroxidation but autoxidation. Investigation of the protein's ability to effectively manage Fenton chemistry upon incubation of H_2O_2 with iron-loaded CyaY indicates that CyaY decreases hydroxyl radical production; however, under aerobic conditions CyaY appears to be less effective at detoxifying iron than Yfh1, as it is devoid of ferroxidase activity in the presence of O_2. Upon treatment with metal chelators, such as ethylene diamine tetracetic acid (EDTA), ferrous iron can be removed from CyaY; whereas, ferric iron remained bound under these conditions and was only removed when treated with strong reducing agents, such as dithionite or dithiothreitol (DTT) [70, 123]. Thus CyaY binds ferric iron tighter than ferrous iron. Additionally, CyaY assembly was shown to be either reversible or preventable with the addition of metal chelators. Further investigation of the metal binding properties of CyaY, has revealed that other metal ions, such as calcium (Ca^{2+}), magnesium (Mg^{2+}), manganese (Mn^{2+}), cobalt (Co^{2+}), europium (Eu^{3+}), ytterbium (Yb^{3+}), gadolinium (Gd^{3+}), and lutetium (Lu^{3+}) can bind to CyaY in solution [134]. Additionally both Al^{3+} and Co^{2+} have been shown to induce CyaY assembly, although to a lesser degree than that seen with iron [123]. Both calcium and magnesium were found to compete with iron binding of CyaY, with aggregation completely reversible at high calcium or magnesium concentrations [123, 134]. Based on these results, CyaY appears to have a low binding specificity for iron and can accommodate almost any divalent or trivalent metal within

the iron binding site. Based on sedimentation velocity AUC experiments, aggregation is more pronounced in the presence of low salt concentrations (10 mM NaCl or KCl); whereas, at more physiologically relevant salt concentrations (150 mM) aggregation is decreased, with aggregation completely abolished at high ionic strengths [70]. Additionally, the negative residues Glu18, Glu19, Asp22, and Glu33 appear to be very important in the aggregation process, as mutation of these residues results in almost complete loss of aggregation [123]. More recently, a role for oligomeric CyaY as the iron donor in Fe-S cluster biosynthesis and heme synthesis has been suggested [133, 135]. *In vivo and in vitro* pull-down assays, suggest an interaction between iron-loaded CyaY oligomers and IscS [133]. These results were confirmed by gel filtration chromatography, where the iron-loaded CyaY intermediate species was found to interact with IscS, with a similar affinity to that of monomer. Additionally, the iron core of the protein could be reduced by cysteine and serve as the iron source for cluster assembly on IscU. Mössbauer spectroscopy of this IscU sample confirmed the presence of primarily [2Fe-2S] clusters with only a minimal amount of [4Fe-4S] clusters, when IscU was incubated in the presence of iron-loaded CyaY oligomer. These findings are further supported by *in vivo* data from Isaya *et al* showing that while the growth rate and cellular stress of ΔYfh1 cells could be rescued by the expression of CyaY, the ability to detoxify iron was significantly reduced [135]. Furthermore the CyaY ΔYfh1 strain was able to restore the aconitase and succinate dehydrogenase activity to within 80-85% of Yfh1(WT); as well as, restore heme synthesis and provide Fe(II) to ferrochelatase. This data suggests that CyaY may play a role in Fe-S cluster and heme synthesis, rather than

iron storage, and is consistent with recent findings suggesting a similar role for oligomeric Yfh1.

Initial characterization of human frataxin FXN[56-210] revealed that unlike yeast Yfh1 and *E. coli* CyaY, recombinately expressed human FXN was expressed as two forms [71]. The first, which was identified as FXN monomer, eluted in the low salt fractions of an ion exchange column, while the second eluted in the high salt fractions and correspond to the pre-assembled oligomeric species of human FXN. Furthermore, in contrast to both yeast Yfh1 and *E. coli* CyaY monomeric FXN was not found to assemble *in vitro* in the presence of iron, except under strong destabilizing conditions resulting in protein precipitation [123]. Based on SDS-PAGE gel and ESI-MS analysis, the pre-assembled FXN oligomer is composed of the ~17 kDa monomeric species, with small amounts of a 14 kDa species also present [71]. Upon incubation of assembled FXN with Fe(II), about 6–10 Fe/molecule FXN were bound [71, 74]. As a result, electrode oximetry was used to investigate the iron oxidation reaction of oligomeric FXN [74]. At Fe(II) to subunit ratios ≤ 0.75 the ferroxidation reaction dominates, while at higher Fe(II) to subunit ratios autoxidation occurred. Coupling the electrode oximetry results to those of Fe K Near-Edge X-ray Absorption spectra, oligomeric FXN has an iron storage capacity and ferrihydrite mineral core similar to that of ferritin; however autoxidation with FXN occurs at a much slower rate than that of ferritin [73-74]. Additionally the mineral cores of both human FXN and yeast Yfh1 share similar properties, with both resulting from aggregation of small ferrihydrite crystals producing a less ordered ferrihydrite core than that of ferritin. This is consistent with the different

modes of oligomerization between yeast (iron dependent) and human frataxin (iron independent). Since human FXN purifies as a pre-assembled oligomer, similar to ferritin, biomineralization would occur after the assembly process was complete. Although this mechanism of iron sequestration decreases the iron storage capacity, it allows for faster sequestration and storage of iron within the protein environment; thus providing the cellular environment with increased protection from ROS and oxidative stress (Figure 4-5). A role in attenuating Fenton chemistry and preventing oxidative damage is further suggested by the ability of oligomeric FXN to prevent supercoiled DNA degradation both in the presence of Fe(II) and Fe(II) with H_2O_2 [74]. Similar to Yfh,1 but in contrast to CyaY, the iron core of FXN cannot be chelated by EDTA and can only be mobilized in the presence of reducing agents [136]. However unlike its homologues, iron mobilization does not mediate oligomer disassembly. Structural characterization of iron-loaded or uranyl acetate stained oligomeric FXN by electron microscopy indicates the presence of spheres about 16 nm in diameter, both alone and as assembled polymer chains, with iron cores smaller than those of yeast Yfh1 (Figure 4-6) [71].
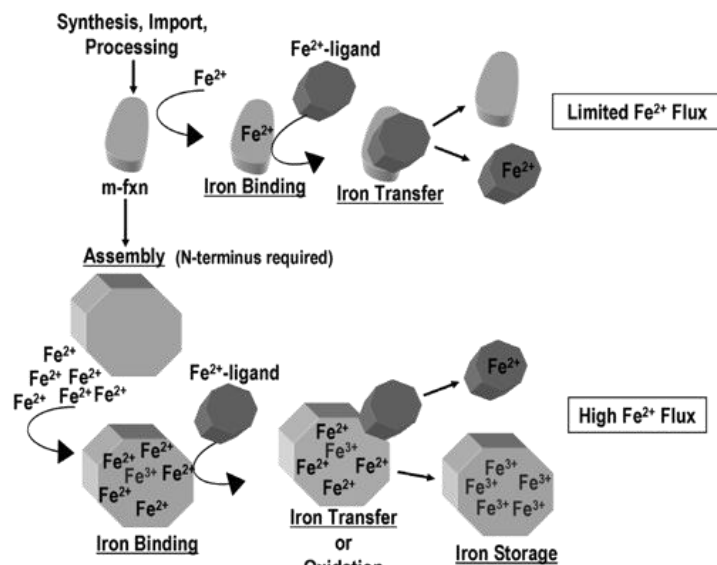
Figure 4-5. Proposed functions for the role of FXN[56-210] *in vivo*. Under conditions of low iron flux, Fe(II) bound to FXN monomer could be rapidly transferred to an iron-binding ligand, such as ISCU. However under high iron conditions the monomer would not be sufficient to prevent the solution chemistry of iron. In this case oligomeric FXN would sequester and store Fe(II) in a bioavailable form that could be transferred to ISCU. Reprinted with permission from *Biochemsitry*, 44(2): 537-545. Copyright 2005 American Chemical Society.
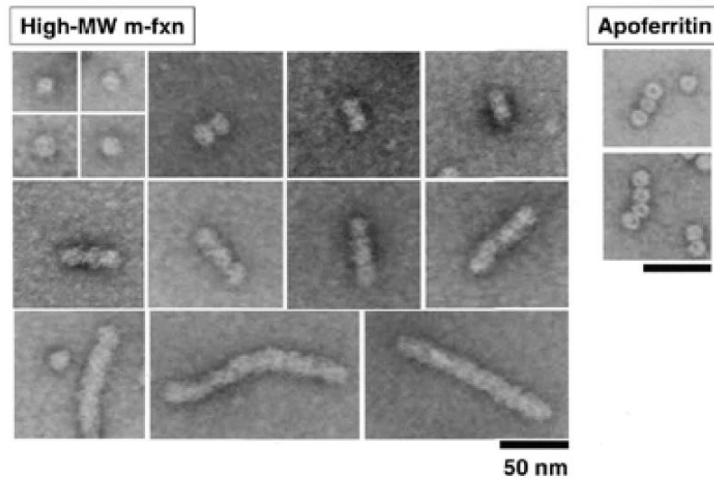
Figure 4-6. Electron microscopy images of oligomeric FXN[56-210] and apo ferritin. Samples of ~0.1 mg/mL of either oligomeric FXN or apo ferritin were stained with 2% uranyl acetate and imaged with an accelerating voltage of 80 kV and an initial magnification of 64,000x. Reprinted with permission from *Human Molecular Genetics*, 11(3): 217-227. Copyright 2002 Oxford University Press.

Size exclusion chromatography and Western blot analysis of these iron-loaded oligomers revealed the presence of two distinct species, a faster moving α, which contained more individual particles and some rods, and a slower moving β, which contained mostly rod shaped particles and few individual particles. These results are similar to the species distribution observed with ferritin and suggest that oligomeric FXN contains some sample heterogeneity in its iron-loaded form. Due to concerns that the oligomeric forms of FXN are simply the result of mechanical stress upon over-expression in recombinant *E. coli* systems, several *in vivo* experiments have been conducted [71, 76, 136]. *In vivo* assembly of oligomeric frataxin was investigated using both a yfh1Δ[FRDA] strain of yeast expressing the precursor form of human frataxin and mouse heart samples [71]. Analysis of whole cell extracts by size exclusion chromatography revealed the presence of both monomeric and oligomeric species, as seen with recombinant over expression of human frataxin in *E. coli*. Additionally expression of human FXN in yeast was able to compensate for the lack of Yfh1 in the knockout strain. Further analysis of the *in vivo* FXN distribution in human heart samples supports the findings in yeast and mouse heart cells, with a heterogeneous population of species ranging from monomer to >1 MDa oligomers present [136]. This suggests that frataxin assembly is not simply a consequence of over expression in *E. coli*, but occurs endogenously. These oligomeric species were also shown to interact with IscU and possibly IscS .

Characterization of the oligomeric species of FXN[42-210] in the context of the monomeric FXN[81-210] form has also been performed to further establish a role for oligomeric FXN species *in vivo* [111]. The FXN[42-210] species distribution from

lymphoblastoid cells revealed the presence of monomers to large oligomers, similar to that seen with the FXN^{56-210} variant. Additionally when comparing the levels of FXN^{42-210} between FRDA patients, carriers, and controls a significant increase in the amount of this species was observed, suggesting the affinity of FXN^{42-210} increases when the levels of FXN^{81-210} decrease below a certain level *in vivo*. While the monomeric form of FXN^{42-210} has only low levels of iron binding, oligomeric FXN^{42-210} showed an iron binding capacity similar to ferritin. Additionally, oligomeric FXN^{42-210} was shown to interact with both NFS1/ISD11 and ISCU either alone or together, suggesting that the oligomer forms extensive and stable interactions with these proteins. The ability of monomeric FXN^{81-210} and monomeric & oligomeric FXN^{42-210} to serve as iron donors for Fe-S cluster assembly was assessed by UV-vis. In the presence of Fe(II), the rate of cluster assembly was essentially the same for all three FXN forms; however, when Fe(III) was used oligomeric FXN^{42-210} had a significantly increased rate of cluster assembly compared to those of monomeric FXN^{81-210} and FXN^{42-210}. Based on this data a dual role is proposed for the FXN^{81-210} and FXN^{42-210} forms depending on the cellular conditions (Figure 4-7).
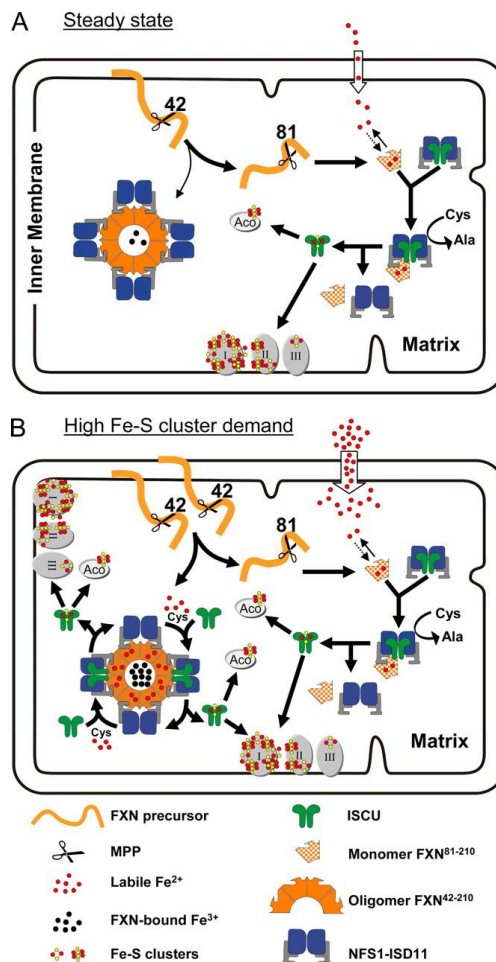
Figure 4-7. Proposed functions of FXN^{42-210} and FXN^{81-210} *in vivo*. Processing of FXN by MPP results in production of FXN^{42-210}, which can oligomerize or be processed further to produce FXN^{81-210}. (A) Under steady state conditions the majority of FXN^{42-210} is cleaved to produce FXN^{81-210} which maintains the labile iron pool and functions in Fe-S cluster biosynthesis. (B) Under high Fe-S cluster demands and increased mitochondrial iron uptake the majority of FXN^{42-210} forms oligomeric assemblies which serve a dual role in iron storage and detoxification and as a site for interaction with the components of the Fe-S cluster biosynthesis machinery (ISCU & NFS1/ISD11) for cluster synthesis. Under steady state conditions, FXN^{42-210} is cleaved to FXN^{81-210}, which interacts with NFS1/ISD11 and ISCU to facilitate Fe-S cluster assembly. However, under conditions of cell growth and global mitochondrial biogenesis a large amount of FXN^{42-210} is not processed and can assemble to produce oligomeric FXN^{42-210}. Under these conditions both the monomeric FXN^{81-210} and oligomeric FXN^{42-210} can serve to facilitate Fe-S cluster biosynthesis, with the later capable of binding iron and maintaining it in a bioavailable and nonreactive form. Reprinted with permission from *Journal of Biological Chemistry*, 285(49): 38486-38501. Copyright 2010 American Society for Biochemistry and Molecular Biology.

Despite the evidence for oligomerization both *in vitro* and *in vivo* in yeast Yfh1, *E. coli* CyaY, and human FXN^{56-210} and FXN^{42-210}, much controversy still surrounds the role of these oligomeric species *in vivo* [76, 78]. Evidence from *Craig et al* suggests that oligomerization is a dispensable function *in vivo* for yeast, as oligomerization deficient mutants of acidic patch residues do not impact the growth phenotype [76]. As this region of Yfh1 has been suggested to be important for iron binding and oligomerization, it would be expected, that if oligomerization was a vital *in vivo* function, mutation of these iron binding residues would adversely affect cell growth Additionally comparison of these mutants with wild-type revealed no difference in their ability to interact with the scaffold protein, indicating that these mutants still allow for interaction of Yfh1 with components of the Fe-S cluster biosynthesis machinery and thus presumably do not affect Fe-S cluster biosynthesis. Furthermore Lesuisse *et al* have demonstrated that the rate of cell death for ΔYfh1 cells grown under high iron concentrations is not as dramatic as expected for a protein serving an iron storage role *in vivo* [78]. Mössbauer spectroscopy of these ΔYfh1 yeast mitochondria further supports this conclusion, as the mineral core of Yfh1 has significant differences from that of ferritin.

EXPERIMENTAL PROCEDURES

Protein Preparation for FXN[56-210]. A pET11a plasmid containing a codon optimized human *FXN* gene (FXN Δ1-55), lacking the first 55 amino acids was transformed into *E. coli* BL21(DE3) competent cells and grown at 37 °C, until an OD_{600} of ~0.7 was obtained. Protein expression was then induced with 0.5 mM isopropyl β-D-1-thiogalactopyranoside (IPTG), and cells were incubated at 16 °C for 16 hours. The cells were then harvested by centrifugation and lysed by sonication (Branson Sonifier 450) in 50 mM Tris pH 7.5, 5 mM EDTA. Ammonium sulfate cuts (50%) were performed on the crude cell lysate, followed by two rounds of dialysis into 50 mM Tris pH 7.5, 5 mM EDTA to remove the ammonium sulfate. The supernatant was loaded onto an anion exchange column (26/20 POROS 60HQ, Applied Biosystems) and eluted with a linear gradient from 0 to 800 mM NaCl in 50 mM Tris pH 7.5, 5 mM EDTA. The fractions corresponding to oligomeric frataxin were collected, concentrated, and loaded onto a Sepharcyl S300 (26/60, GE Healthcare) size exclusion column equilibrated with 50 mM HEPES pH 7.5, 150 mM NaCl, 5 mM EDTA. Protein concentration was calculated using the absorbance at 280 nm with an extinction coefficient of 33,000 $M^{-1}cm^{-1}$.

Protein Preparation for FXN[42-210]. Megaprimer mutagenesis was performed on the codon optimized human *FXN* gene (FXN Δ1-55) construct to generate pET28a His-GFP-TEV and pET28a His-GST-TEV plasmids containing the codon optimized human *FXN* gene (FXN Δ1-41), lacking the first 41 amino acids. DNA sequencing by the Texas A&M University Gene Technology Laboratory confirmed the presence of the

71

FXN Δ1-41 construct. The plasmids containing each construct were transformed into *E. coli* BL21(DE3) competent cells and grown at 37 °C, until an OD_{600} of ~0.7 was obtained. Protein expression was assessed with varied concentrations of isopropyl β-D-1-thiogalactopyranoside (IPTG), and cells were incubated at 16 °C for 16 hours. The cells were then harvested by centrifugation and lyzed by sonication (Branson Sonifier 450) in 50 mM Tris pH 7.5. Protein expression levels and solubility were analyzed by 14% SDS-PAGE gel.

Cysteine Desulfurase Activity Measurements. Reactions were performed as previously described using a total volume of 800 μL [22, 109-110]. The reaction mixtures containing 0.5 μM NFS1/ISD11 (SD), 1.5 uM ISCU2, between 1.5-200 μM oligomeric FXN[56-210] (o-FXN), 10 μM pyridoxal-5'-phosphate (PLP), 2 mM dithiothreitol (DTT), 5 μM $Fe(NH_4)_2(SO_4)_2$, and 50 mM Tris, 250 mM NaCl pH 8.0 were incubated for 30 minutes in an anaerobic glovebox at ~14 °C [22]. The cysteine desulfurase reaction was initiated with the addition of 100 μM L-cysteine at 37 °C, and quenched with 100 μL each of 20 mM *N,N*-dimethyl-*p*-phenylenediamine in 7.2 N HCl and 30 mM $FeCl_3$ in 1.2 N HCl; followed by 20 minutes of incubation at 37 °C and centrifugation for 5 minutes at 12,000 rpm. The methylene blue formation was measured at 670 nm and converted to sulfide production using a Na_2S standard curve. The rate is expressed in units of mol sulfide per mol SD per minute at 37 °C.

Analytical Ultracentrifugation of FXN[56-210]. Purified oligomeric FXN[56-210] and monomeric mature FXN[81-210] were dialyzed into 50 mM potassium phosphate pH 7.5, 150 mM NaCl. Samples of each variant were prepared at optical densities (OD) of 0.3,

0.6 and 0.9, based on the UV-vis absorbance at 230 nm. Samples were flash frozen in liquid nitrogen and shipped on dry ice to the Center for Macromolecular Interactions at the University of Texas Health Science Center at San Antonio where sedimentation velocity analytical ultracentrifugation (AUC) analysis was performed. Initial scans were performed at 230 nm; however due to the high intensity of the samples, samples were run at 280 nm.

RESULTS

Soluble Protein Expression of FXN$^{42-210}$. The best recombinant expression conditions for the FXN$^{42-210}$ variant in *E. coli* were determined to occur with the His-GST-TEV pET28a vector expressed with 0.5 mM IPTG at 16 °C for 16 hours.

Oligomeric FXN$^{56-210}$ Activates the Fe-S Cluster Assembly Complex. The FXN$^{42-210}$ variant was expressed in *E. coli* and purified to about 85% homogeneity. The ability of the oligomeric variant to stimulate the cysteine desulfurase activity of the SDU complex was investigated. *In vivo* cellular concentrations of cysteine were approximated with the addition of 100 μM L-cysteine. While some activation of the cysteine desulfurase activity was observed, it was significantly lower than that seen with the mature FXN$^{81-210}$ variant (Figure 4-8).

Oligomeric FXN$^{56-210}$ is a Heterogeneous Mixture of Species. The species distribution and oligomerization properties of the FXN$^{56-120}$ and FXN$^{81-210}$ variants were analyzed (Figure 4-9). While the mature FXN$^{81-210}$ variant exhibited a single monomeric

species in solution, the FXN^{56-210} variant is a heterogeneous mixture of species with

larger oligomeric and aggregate species forming over time.
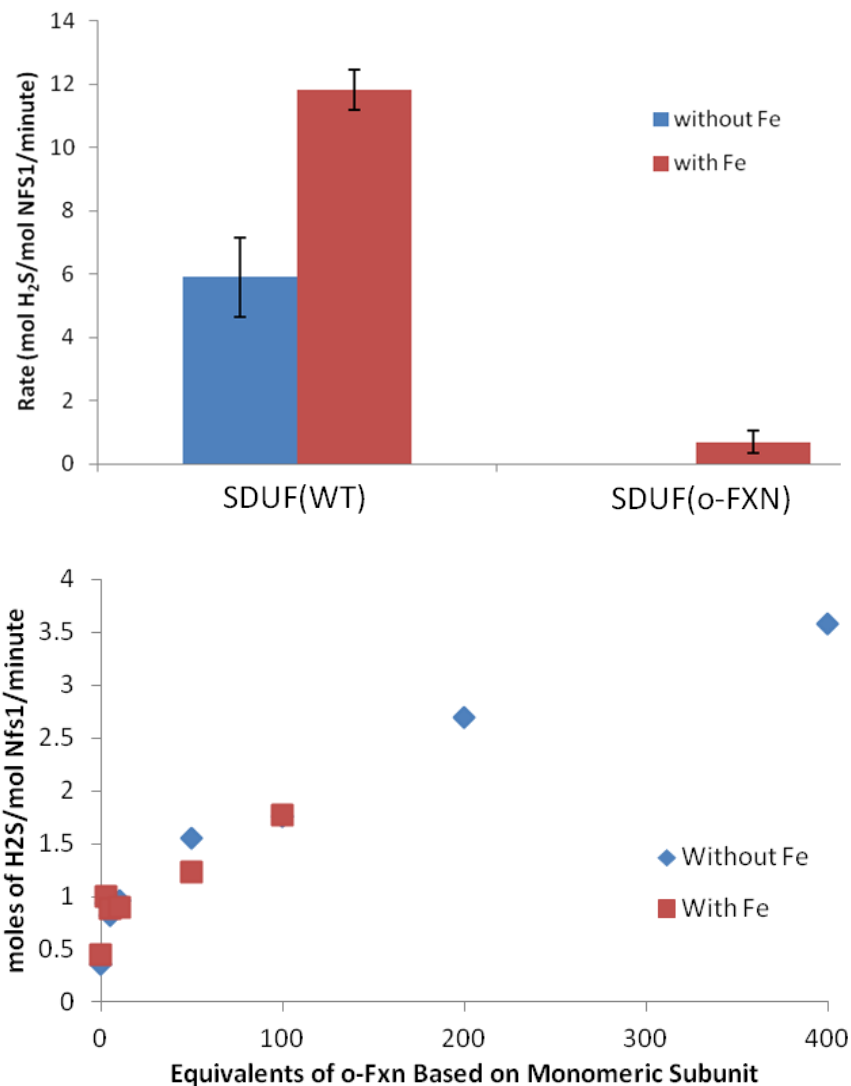
Figure 4-8. Bar chart of SDU with 3 equivalents of either mature FXN^{81-210}, SDUF(WT), or oligomeric FXN^{56-210}, SDUF(o-FXN), (top). Titration of SDU with oligomeric FXN^{56-210} (bottom). Blue bars or data points are without iron, while red bars or data points are in the presence of iron.
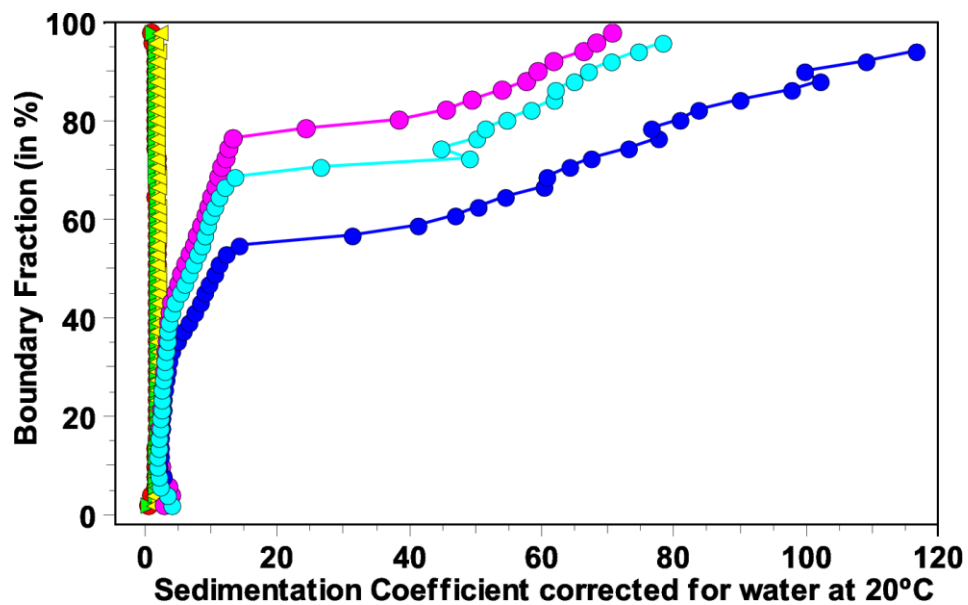
Figure 4-9. Representation of the analytical ultracentrifuge data with a van Holde-Weischet Combined Distribution plot, where a vertical line indicates homogeneous species and a parabola indicates a heterogeneous mixture of species. Samples of mature FXN[81-210] (red OD= 0.3, green OD=0.6, and yellow OD =0.9) and oligomeric FXN[56-210] (magenta OD=0.3, blue OD=0.6, and cyan OD=0.9) were analyzed at 280 nm.

DISCUSSION

Extensive investigation of the oligomeric frataxin species in the yeast, *E. coli*, and human systems has been performed by Isaya *et al*, Pastore *et al*, and others. However given the complexities and variability of these systems the studies have proven difficult, with the results often met by controversy from the Fe-S cluster biosynthesis community. Given the available data, two scenarios for the role of the oligomeric frataxin protein family are proposed: (1) frataxin proteins are iron scavengers and transporters under specific cellular conditions or (2) frataxin proteins have a role in protein-protein interactions or Fe-S cluster biosynthesis [116, 122-123]. The recent discovery of a mitochondrial ferritin protein in the human system, lends support for a role of human FXN in Fe-S cluster biosynthesis verses iron storage [70, 77]. Similarly the presences of several ferritin or ferritin-type proteins in bacteria, suggests the primary role of *E. coli* CyaY is an iron chaperone or iron sensor for Fe-S cluster biosynthesis with the iron storage and assembly properties serving as a secondary side-function of the protein [70, 135]. In contrast the yeast system lacks a mitochondrial ferritin, thus the ferroxidase activity of Yfh1 is likely an attempt to substitute for this role; ultimately supporting an iron storage role for this protein.

While the present data supports interactions between oligomeric FXN^{56-210} and the SDU complex, these findings are complicated by the presence of multiple FXN species in solution. Although activation of the cysteine desulfurase is observed with SDU in the presence of oligomeric FXN^{56-210} there does not appear to be iron dependence to this activity, as is seen with the mature FXN^{81-210} variant. This

stimulation suggests an interaction between the oligomeric FXN species and SDU, and supports the findings of Isaya *et al* showing that oligomeric yeast Yfh1 and human FXN[42-210] can interact with the SDU complex and facilitate the formation of Fe-S clusters [111, 132]. Furthermore the lack of saturation of the cysteine desulfurase activity, even after the addition of 400 monomeric equivalents would suggest that the stimulating form of the FXN oligomer has either very weak binding interacts to the SDU complex or is present in very low abundance within the sample. This is in contrast to the findings of Isaya *et al* where oligomeric FXN[42-210] was shown to have about twice the Fe-S cluster assembly rate of monomeric FXN[81-210] [111]. However it is important to note that Fe-S cluster assembly is a thermodynamically driven process and that the increased presence of iron on the oligomeric verses monomeric sample with DTT could artificially accelerated this rate. The cysteine desulfurase assay finds are complicated by the results of the AUC analysis, showing a heterogeneous distribution of FXN species in solution ranging from monomer to large aggregates above 1 MDa. The presence of a heterogeneous mixture of species within oligomeric samples of the frataxin family is well documented, although not widely highlighted in the literature, for the yeast, *E. coli*, and human systems. While an iron dependence has been shown for the oligomeric assembly in the yeast and *E. coli* systems both have been shown to contain multiple species, even under highly oligomer favoring conditions, with yeast Yfh1 retaining about 20% monomer upon assembly completion [69, 126]. Additionally, incomplete assembly has been demonstrated for human frataxin both *in vivo* and *in vitro*. Isaya *et al* has demonstrated a varied species composition for frataxin samples from mouse and human

heart; as well as in yeast yfh1Δ[FRDA] cells expressing human FXN [71, 74]. *In vitro* analysis of FXN$^{56-210}$ with electron microscopy shows assembles of oligomers ranging from single spheres to chains of spheres of varied lengths [71]. The human FXN$^{56-210}$ iron-loaded oligomer has been shown by size exclusion chromatography and Western blot analysis to contain two species, a faster moving α, which contains more individual particles and some rods, and a slower moving β, which contains mostly rod shaped particles and few individual particles. As the factors governing oligomerization in the human system are not currently known nor are procedures for isolate and stabilize of the individual species within this oligomeric sample, it is impossible at this time to identify which of the species is serving to stimulate the cysteine desulfurase activity of the SDU complex.

Given the available data, the authors propose a FXN storage function for the role of the FXN oligomer *in vivo*. In this role, FXN oligomeric species would assemble under conditions of FXN overload. These assembled FXN$^{56-210}$ oligomers could then disassemble to serve as a source of FXN during high protein demand. As the FXN$^{56-210}$ variant is known to truncate and produce the mature form of the protein, FXN$^{81-210}$, this would serve as an effective regulator mechanism within cells [57]. This role is supported by the cysteine desulfurase assay and AUC results presented here, as well as findings by Isaya *et al* that under denaturing gel conditions oligomeric FXN$^{56-210}$ contains a major 17 kDa band and a smaller amount of a 14 kDa product, which likely corresponds to the mature form of the protein [71]. Ultimately the current experimental restrains prevent assignment of the observed cysteine desulfurase activity to any specific

specie(s) within the FXN[56-210] oligomer sample, thus the following model is proposed

(Figure 4-10). Oligomer disassembly would produce species capable of interacting and

activating the SDU complex; whether this is one discrete species, multiple species,

monomeric or multi-meric species remains to be determined.
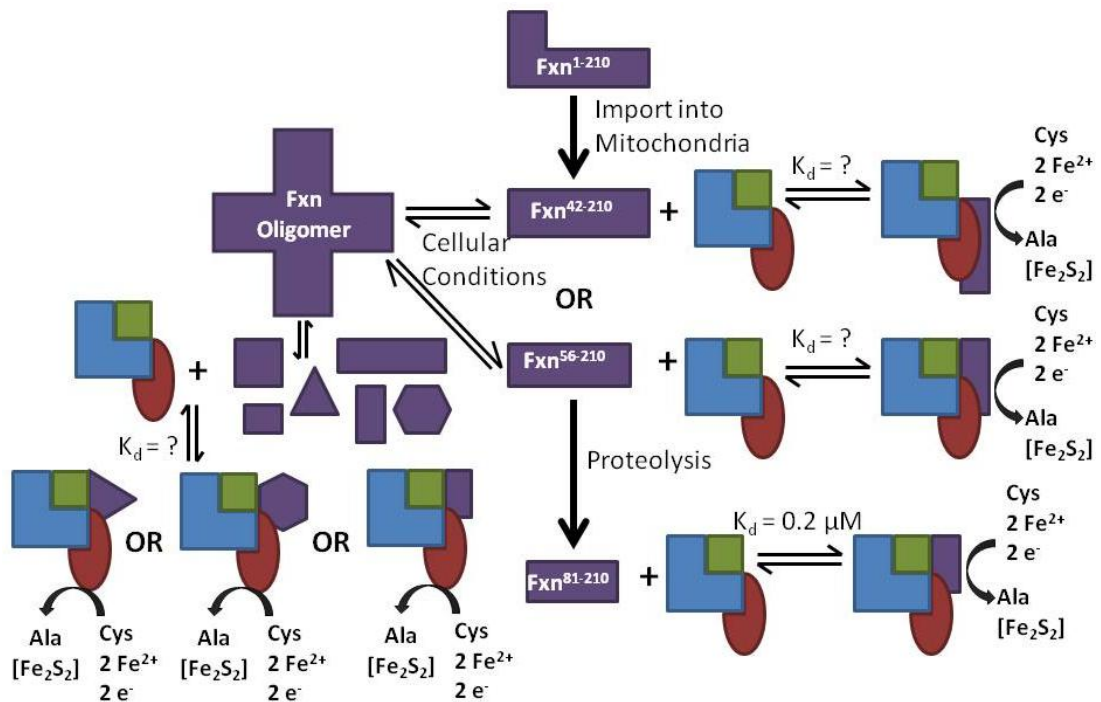
Figure 4-10. Model for the interaction of FXN variants with SDU, where blue arrowhead is NFS1, green square is ISD11, red oval is ISCU, and purple is the FXN variants.

CHAPTER V

CONCLUSION

The work presented here further supports the role of FXN as an allosteric activator of the SDU complex, and has significant implications for therapeutic applications in the treatment of Friedreich's Ataxia (FRDA). The α_2 helix FRDA mutant L182F exhibits essentially wild-type activity and kinetic parameters upon interaction with SDU. This FRDA mutant is therefore impaired in a different manner than the other FRDA β-sheet mutants (N146K, Q148R, W155R, R165C) characterized in the Barondeau lab that show defects in binding and activation of the SDU complex. Taken together three factors have been identified from *in vivo* and *in vitro* experiments that appear to contribute to FRDA pathology: impairment in binding and activation of the SDU complex, processing defects, and protein instability or misfolding. There is no evidence for a processing defect in L182F making it dissimilar to other FRDA point mutants such as G130V, I154F, L156P, and W173G. It therefore seems likely that the L182F mutant is destabilized relative to native FXN. This mutant may be analogous to the D122Y clinical mutant, which exhibits essentially wild-type kinetic behavior and decreased protein stability. Like the L182F mutant, this D122Y mutant also lies outside the conserved β-sheet region of the FXN protein. Speculating from previous results and the work presented here, it is likely that FRDA mutants located on the surface of the FXN β_4 and β_5 sheets are affected due to kinetic impairment of the interactions with SDU. Meanwhile FRDA mutants outside of this region, especially those located in the

80

protein core, are likely to impact the protein stability and/or processing. Systematic analysis of both the kinetic and stability properties of all 17 FRDA mutants is warranted to further identify the factors governing disease phenotype in each case. Additionally this analysis could provide valuable information on the factors governing the second step of the FXN truncation process, with current data hinting at protein folding as a possible factor. As FXN has also been shown to interact with several of the Fe-S cluster transfer proteins, the affect FRDA mutants have on these interactions should also be interrogated using a cluster transfer assay currently under development in our lab.

Alanine scanning mutagenesis experiments were designed to identify the contribution of specific FXN residues in the activation of the SDU complex, further test the model for FXN as an allosteric activator, and potentially lead to the development of improved therapeutics for FRDA. While a handful of FXN residues have previously been suggested as sites of interaction with SDU, to the author's knowledge, this is the first systematic investigation of interaction effects at the residue level for FXN. While the majority of the 35 point mutants studied had little impact on the kinetic parameters for the cysteine desulfurase reaction of the SDUF complex, several important differences were noted. A hotspot for SDU interaction was identified on the FXN β_4 and β_5 sheets; with residues Q153, W155, and R165 implicated as vital for SDU binding and residues N146, Q148, Q153, and W155 shown to be essential for SDU activation. The presence of FRDA mutants at many of these residues lends further support for their importance in FXN/SDU interactions. Although previous results have suggested an iron donor role for the FXN protein *in vivo* the results of the alanine scanning analysis presented here argue

strongly against this function; as acidic patch mutants have little effect on the FXN/SDU interaction. This data further supports the allosteric activator function of FXN as the correct *in vivo* role of the protein. As with the other mutants presented here analysis of the 35 alanine scanning mutants in the context of FXN interactions with cluster transfer proteins should also be studied. An allosteric regulator role implies that FXN levels are modulated by some environmental stimuli to control Fe-S cluster biosynthesis. These stimuli could control FXN levels by regulating the expression or degradation of FXN protein, by controlling the processing and oligomerization upon import into the mitochondria, or through post-translational modifications. FXN expression levels appear to be modulated by iron levels and acetylation, ubiquitination, plus nitration sites have been identified on FXN. Preliminary data presented here reveals acetylation mimics do not appear to modulate binding or activation of human FXN to the SDU complex. However differences in the placement of C-terminal lysine residues between mouse and human FXN warrants further investigation of all four C-terminal lysine residues of human FXN. Furthermore the effects of acetyl-lysine mimics should be determined in the cluster transfer process, as these modifications could mediate FXN chaperone interactions. Finally investigation of the oligomeric FXN$^{56-210}$ variant indicates that minor activation of the cysteine desulfurase activity is present; however the heterogeneous species distribution makes further interrogation of this activity difficult. As the observed activity of the oligomeric species can't be linked to any one component of the oligomeric FXN$^{56-210}$ sample, we hypothesize a possible FXN storage function for the oligomeric species *in vivo* with activation of SDU generated from only a

small subset of the disassembled oligomer species.   This role would allow for dynamic regulation of FXN concentrations *in vivo*.

FRDA therapeutics have been focused on increasing FXN protein levels and on addressing potential secondary effects of FXN depletion such as the addition of chelators to combat the iron overload in the mitochondria and antioxidants to treat the increase in oxidative stress. Results generated here suggest a couple of additional avenues to approach FRDA therapeutics. First the further support of a FXN allosteric activator role suggests a general strategy of screening small molecule libraries as a mechanism of replacing FXN function and stabilizing the active form of the SDU compex. Second, the identified FXN hotspot suggests a rational design approach encompassing small cyclic peptide mimics as potential FRDA therapeutics. Proposed cyclic peptides for investigation should include NAQAQAWA, QAWARA, WARA, NLQAQIWL. The NAQAQAWA and NLQAQIWL peptides represent the FXN residues identified as vital for SDU activation with either alanine residues or the actual FXN sequence residues used as spacers. The QAWARA peptide contains the three residues identified as vital for FXN binding to SDU. The final proposed peptide WARA contains the residues identified as the most important for activation (W155) and binding (R165), respectively. Third, the significant increase in SDU binding (~100-fold tighter) observed with the S126A mutant, while unexpected, could have relevance for therapeutic development, as only small amounts of this mutant would be required to stimulate the SDU complex. In fact, as soon as the enhanced binding of the S126A FXN mutant is confirmed, it should

be considered for substitution of the native FXN in TAT-frataxin fusion proteins that are

currently being tested as therapeutics.

REFERENCES

1.   Huber, C. and G. Wachtershauser, *Peptides by activation of amino acids with CO on (Ni,Fe)S surfaces: Implications for the origin of life.* Science, 1998. **281**(5377): p. 670-672.

2.   Beinert, H., R.H. Holm, and E. Munck, *Iron-sulfur clusters: Nature's modular, multipurpose structures.* Science, 1997. **277**(5326): p. 653-659.

3.   Fontecave, M., *Iron-sulfur clusters: ever-expanding roles.* Nature Chemical Biology, 2006. **2**(4): p. 171-174.

4.   Johnson, D.C., et al., *Structure, function, and formation of biological iron-sulfur clusters.* Annual Review of Biochemistry, 2005. p. 247-281.

5.   Lill, R., *Function and biogenesis of iron-sulphur proteins.* Nature, 2009. **460**(7257): p. 831-838.

6.   Lill, R. and U. Muhlenhoff, *Iron-sulfur protein biogenesis in eukaryotes: Components and mechanisms.* Annual Review of Cell and Developmental Biology, 2006. p. 457-486.

7.   Rouault, T.A., *Biogenesis of iron-sulfur clusters in mammalian cells: new insights and relevance to human disease.* Disease Models & Mechanisms, 2012. **5**(2): p. 155-164.

8.   Meyer, J., *Iron-sulfur protein folds, iron-sulfur chemistry, and evolution.* Journal of Biological Inorganic Chemistry, 2008. **13**(2): p. 157-170.

9.   Bandyopadhyay, S., K. Chandramouli, and M.K. Johnson, *Iron-sulfur cluster biosynthesis.* Biochemical Society Transactions, 2008. **36**: p. 1112-1119.

10.   Brzoska, K., S. Meczynska, and M. Kruszewski, *Iron-sulfur cluster proteins: electron transfer and beyond.* Acta Biochimica Polonica, 2006. **53**(4): p. 685-691.

11.   Dos Santos, P.C. and D.R. Dean, *A newly discovered role for iron-sulfur clusters.* Proceedings of the National Academy of Sciences of the United States of America, 2008. **105**(33): p. 11589-11590.

12.   Jacobson, M.R., et al., *Biochemical and genetic analysis of the nifUSVWZM cluster from Azotobacter vinelandii.* Molecular & General Genetics, 1989. **219**(1-2): p. 49-57.

13.   Takahashi, Y. and U. Tokumoto, *A third bacterial system for the assembly of iron-sulfur clusters with homologs in archaea and plastids.* Journal of Biological Chemistry, 2002. **277**(32): p. 28380-28383.

14.   Zheng, L.M., et al., *Assembly of iron-sulfur clusters - Identification of an iscSUA-hscBA-fdx gene cluster from Azotobacter vinelandii.* Journal of Biological Chemistry, 1998. **273**(21): p. 13264-13272.

15.   Fontecave, M., et al., *Mechanisms of iron-sulfur cluster assembly: the SUF machinery.* Journal of Biological Inorganic Chemistry, 2005. **10**(7): p. 713-721.

16.   Martelli, A., M. Napierala, and H. Puccio, *Understanding the genetic and molecular pathogenesis of Friedreich's ataxia through animal and cellular models.* Disease Models & Mechanisms, 2012. **5**(2): p. 165-176.

17. Rouault, T.A. and W.H. Tong, *Iron-sulfur cluster biogenesis and human disease.* Trends in Genetics, 2008. **24**(8): p. 398-407.

18. Sheftel, A., O. Stehling, and R. Lill, *Iron–sulfur proteins in health and disease.* Trends in Endocrinology & Metabolism, 2010. **21**(5): p. 302-314.

19. Shi, R., et al., *Structural Basis for Fe-S Cluster Assembly and tRNA Thiolation Mediated by IscS Protein-Protein Interactions.* Plos Biology, 2010. **8**(4).

20. Adam, A.C., et al., *The Nfs1 interacting protein Isd11 has an essential role in Fe/S cluster biogenesis in mitochondria.* Embo Journal, 2006. **25**(1): p. 174-183.

21. Shi, Y., et al., *Human ISD11 is essential for both iron–sulfur cluster assembly and maintenance of normal cellular iron homeostasis.* Human Molecular Genetics, 2009. **18**(16): p. 3014-3025.

22. Tsai, C.L. and D.P. Barondeau, *Human Frataxin Is an Allosteric Switch That Activates the Fe-S Cluster Biosynthetic Complex.* Biochemistry, 2010. **49**(43): p. 9132-9139.

23. Wiedemann, N., et al., *Essential role of Isd11 in mitochondrial iron-sulfur cluster synthesis on Isu scaffold proteins.* EMBO J, 2006. **25**(1): p. 184-195.

24. Schwartz, C.J., et al., *The cysteine desulfurase, IscS, has a major role in in vivo Fe-S cluster formation in Escherichia coli.* Proceedings of the National Academy of Sciences, 2000. **97**(16): p. 9009-9014.

25. Cupp-Vickery, J.R., H. Urbina, and L.E. Vickery, *Crystal structure of IscS, a cysteine desulfurase from Escherichia coli.* Journal of Molecular Biology, 2003. **330**(5): p. 1049-1059.

26. Turowski, V.R., M.V. Busi, and D.F. Gomez-Casati, *Structural and Functional Studies of the Mitochondrial Cysteine Desulfurase from Arabidopsis thaliana.* Molecular Plant, 2012. **5**(5): p. 1001-1010.

27. Schmucker, S., et al., *Mammalian Frataxin: An Essential Function for Cellular Viability through an Interaction with a Preformed ISCU/NFS1/ISD11 Iron-Sulfur Assembly Complex.* PLoS ONE, 2011. **6**(1): p. e16199.

28. Colin, F., et al., *Mammalian Frataxin Controls Sulfur Production and Iron Entry during de Novo Fe_4S_4 Cluster Assembly.* Journal of the American Chemical Society, 2012.

29. Zheng, L.M., et al., *Mechanism for the Desulfurization of L-Cysteine Catalyzed by the nifS Gene Product.* Biochemistry, 1994. **33**(15): p. 4714-4720.

30. Nuth, M. and J.A. Cowan, *Iron–sulfur cluster biosynthesis: characterization of IscU–IscS complex formation and a structural model for sulfide delivery to the [2Fe–2S] assembly site.* JBIC Journal of Biological Inorganic Chemistry, 2009. **14**(6): p. 829-839.

31. Smith, A.D., et al., *Sulfur transfer from IscS to IscU: The first step in iron-sulfur cluster biosynthesis.* Journal of the American Chemical Society, 2001. **123**(44): p. 11103-11104.

32. Rabb, J.D., *Frataxin (FXN) based regulation of the iron-sulfur cluster assembly complex.* 2012, Texas A&M University: United States, Texas. p. 270.

33.   Bertini, I., et al., *Thermotoga maritima IscU. Structural characterization and dynamics of a new class of metallochaperone.* Journal of Molecular Biology, 2003. **331**(4): p. 907-924.

34.   Ramelot, T.A., et al., *Solution NMR structure of the iron-sulfur cluster assembly protein U (IscU) with zinc bound at the active site.* Journal of Molecular Biology, 2004. **344**(2): p. 567-583.

35.   Liu, J.Y., et al., *Structural characterization of an iron-sulfur cluster assembly protein IscU in a zinc-bound form.* Proteins-Structure Function and Bioinformatics, 2005. **59**(4): p. 875-881.

36.   Shimomura, Y., et al., *Characterization and crystallization of an IscU-type scaffold protein with bound 2Fe-2S cluster from the hyperthermophile, Aquifex aeolicus.* Journal of Biochemistry, 2007. **142**(5): p. 577-586.

37.   Shimomura, Y., et al., *The Asymmetric Trimeric Architecture of [2Fe-2S] IscU: Implications for Its Scaffolding during Iron-Sulfur Cluster Biosynthesis.* Journal of Molecular Biology, 2008. **383**(1): p. 133-143.

38.   Kim, J.H., M. Tonelli, and J.L. Markley, *Disordered form of the scaffold protein IscU is the substrate for iron-sulfur cluster assembly on cysteine desulfurase.* Proceedings of the National Academy of Sciences, 2012. **109**(2): p. 454-459.

39.   Foster, M.W., et al., *A mutant human IscU protein contains a stable 2Fe-2S (2+) center of possible functional significance.* Journal of the American Chemical Society, 2000. **122**(28): p. 6805-6806.

40.   Huang, J. and J.A. Cowan, *Iron-sulfur cluster biosynthesis: role of a semi-conserved histidine.* Chemical Communications, 2009(21): p. 3071-3073.

41.   Agar, J.N., et al., *IscU as a scaffold for iron-sulfur cluster biosynthesis: Sequential assembly of 2Fe-2S and 4Fe-4S clusters in IscU.* Biochemistry, 2000. **39**(27): p. 7856-7862.

42.   Chandramouli, K., et al., *Formation and properties of 4Fe-4S clusters on the IscU scaffold protein.* Biochemistry, 2007. **46**(23): p. 6804-6811.

43.   Cupp-Vickery, J.R., et al., *Crystal Structure of the Molecular Chaperone HscA Substrate Binding Domain Complexed with the IscU Recognition Peptide ELPPVKIHC.* Journal of Molecular Biology, 2004. **342**(4): p. 1265-1278.

44.   Luo, W.I., et al., *Kinetic and structural characterization of human mortalin.* Protein Expression and Purification, 2010. **72**(1): p. 75-81.

45.   Shan, Y. and G. Cortopassi, *HSC20 interacts with frataxin and is involved in iron–sulfur cluster biogenesis and iron homeostasis.* Human Molecular Genetics, 2012. **21**(7): p. 1457-1469.

46.   Vickery, L.E. and J.R. Cupp-Vickery, *Molecular chaperones HscA/Ssq1 and HscB/Jac1 and their roles in iron-sulfur protein maturation.* Critical Reviews in Biochemistry and Molecular Biology, 2007. **42**(2): p. 95-111.

47.   Muhlenhoff, U., et al., *Components involved in assembly and dislocation of iron-sulfur clusters on the scaffold protein Isu1p.* Embo Journal, 2003. **22**(18): p. 4815-4825.

48.   Zhai, P., et al., *The human escort protein hep binds to the ATPase domain of mitochondrial Hsp70 and regulates ATP hydrolysis.* Journal of Biological Chemistry, 2008. **283**(38): p. 26098-26106.

49.   Chamberlain, S., et al., *Mapping of mutation causing Friedreich's ataxia to human chromosome 9.* Nature, 1988. **334**(6179): p. 248-250.

50.   Chamberlain, S., et al., *Genetic recombination events which position the Friedreich ataxia locus proximal to the D9S15/D9S5 linkage group on chromosome 9q.* American Journal of Human Genetics, 1993. **52**(1): p. 99-109.

51.   Dhe-Paganon, S., et al., *Crystal structure of human frataxin.* Journal of Biological Chemistry, 2000. **275**(40): p. 30753-30756.

52.   Nair, M., et al., *Solution structure of the bacterial frataxin ortholog, CyaY: Mapping the iron binding sites.* Structure, 2004. **12**(11): p. 2037-2048.

53.   Cho, S.J., et al., *Crystal structure of Escherichia coli CyaY protein reveals a previously unidentified fold for the evolutionarily conserved frataxin family.* Proceedings of the National Academy of Sciences of the United States of America, 2000. **97**(16): p. 8932-8937.

54.   Musco, G., et al., *Towards a structural understanding of Friedreich's ataxia: the solution structure of frataxin.* Structure, 2000. **8**(7): p. 695-707.

55.   Leidgens, S., S. De Smet, and F. Foury, *Frataxin interacts with Isu1 through a conserved tryptophan in its beta-sheet.* Human Molecular Genetics, 2010. **19**(2): p. 276-286.

56. Wang, T. and E.A. Craig, *Binding of Yeast Frataxin to the Scaffold for Fe-S Cluster Biogenesis, Isu.* Journal of Biological Chemistry, 2008. **283**(18): p. 12674-12679.

57. Cavadini, P., et al., *Two-step processing of human frataxin by mitochondrial processing peptidase - Precursor and intermediate forms are cleaved at different rates.* Journal of Biological Chemistry, 2000. **275**(52): p. 41469-41475.

58. Condo, I., et al., *In vivo maturation of human frataxin.* Human Molecular Genetics, 2007. **16**(13): p. 1534-1540.

59. Gordon, D.M., et al., *Maturation of Frataxin Within Mammalian and Yeast Mitochondria: One-Step Processing by Matrix Processing Peptidase.* Human Molecular Genetics, 1999. **8**(12): p. 2255-2262.

60. Koutnikova, H., V. Campuzano, and M. Koenig, *Maturation of Wild-Type and Mutated Frataxin by the Mitochondrial Processing Peptidase.* Human Molecular Genetics, 1998. **7**(9): p. 1485-1489.

61. Long, S., et al., *Mitochondrial localization of human frataxin is necessary but processing is not for rescuing frataxin deficiency in Trypanosoma brucei.* Proceedings of the National Academy of Sciences of the United States of America, 2008. **105**(36): p. 13468-13473.

62. Schmucker, S., et al., *The in vivo mitochondrial two-step maturation of human frataxin.* Human Molecular Genetics, 2008. **17**(22): p. 3521-3531.

63. Yoon, T., E. Dizin, and J.A. Cowan, *N-terminal iron-mediated self-cleavage of human frataxin: regulation of iron binding and complex formation with target proteins.* Journal of Biological Inorganic Chemistry, 2007. **12**(4): p. 535-542.

64. Adinolfi, S., et al., *Bacterial frataxin CyaY is the gatekeeper of iron-sulfur cluster formation catalyzed by IscS.* Nat Struct Mol Biol, 2009. **16**(4): p. 390-396.

65. Becker, E.M., et al., *Erythroid differentiation and protoporphyrin IX down-regulate frataxin expression in Friend cells: characterization of frataxin expression compared to molecules involved in iron metabolism and hemoglobinization.* Blood, 2002. **99**(10): p. 3813-3822.

66. Gakh, O., et al., *Mitochondrial iron detoxification is a primary function of frataxin that limits oxidative damage and preserves cell longevity.* Human Molecular Genetics, 2006. **15**(3): p. 467-479.

67. Lesuisse, E., et al., *Iron use for haeme synthesis is under control of the yeast frataxin homologue (Yfh1).* Human Molecular Genetics, 2003. **12**(8): p. 879-889.

68. Yoon, T. and J.A. Cowan, *Iron-sulfur cluster biosynthesis. Characterization of frataxin as an iron donor for assembly of 2Fe-2S clusters in ISU-type proteins.* Journal of the American Chemical Society, 2003. **125**(20): p. 6078-6084.

69. Adamec, J., et al., *Iron-dependent self assembly of recombinant yeast frataxin: Implications for Friedreich ataxia.* American Journal of Human Genetics, 2000. **67**(3): p. 549-562.

70. Bou-Abdallah, F., et al., *Iron Binding and Oxidation Kinetics in Frataxin CyaY of Escherichia coli.* Journal of Molecular Biology, 2004. **341**(2): p. 605-615.

71. Cavadini, P., et al., *Assembly and iron-binding properties of human frataxin, the protein deficient in Friedreich ataxia.* Human Molecular Genetics, 2002. **11**(3): p. 217-227.

72. Cook, J.D., et al., *Monomeric yeast frataxin is an iron-binding protein.* Biochemistry, 2006. **45**(25): p. 7767-7777.

73. Nichol, H., et al., *Structure of frataxin iron cores: An X-ray absorption spectroscopic study.* Biochemistry, 2003. **42**(20): p. 5971-5976.

74. O'Neill, H.A., et al., *Assembly of human frataxin is a mechanism for detoxifying redox-active iron.* Biochemistry, 2005. **44**(2): p. 537-545.

75. Park, S., et al., *The ferroxidase activity of yeast frataxin.* Journal of Biological Chemistry, 2002. **277**(41): p. 38589-38595.

76. Aloria, K., et al., *Iron-induced oligomerization of yeast frataxin homologue Yfh1 is dispensable in vivo.* EMBO Rep, 2004. **5**(11): p. 1096-1101.

77. Levi, S., et al., *A human mitochondrial ferritin encoded by an intronless gene.* Journal of Biological Chemistry, 2001. **276**(27): p. 24437-24440.

78. Seguin, A., et al., *Evidence that yeast frataxin is not an iron storage protein in vivo.* Biochimica Et Biophysica Acta-Molecular Basis of Disease, 2010. **1802**(6): p. 531-538.

79.   Cavadini, P., et al., *Human frataxin maintains mitochondrial iron homeostasis in Saccharomyces cerevisiae.* Human Molecular Genetics, 2000. **9**(17): p. 2523-2530.

80.   Foury, F. and D. Talibi, *Mitochondrial Control of Iron Homeostasis: A GENOME WIDE ANALYSIS OF GENE EXPRESSION IN A YEAST FRATAXIN-DEFICIENT STRAIN.* Journal of Biological Chemistry, 2001. **276**(11): p. 7762-7768.

81.   Radisky, D.C., M.C. Babcock, and J. Kaplan, *The Yeast Frataxin Homologue Mediates Mitochondrial Iron Efflux: EVIDENCE FOR A MITOCHONDRIAL IRON CYCLE.* Journal of Biological Chemistry, 1999. **274**(8): p. 4497-4499.

82.   Bridwell-Rabb, J., et al., *Effector Role Reversal during Evolution: The Case of Frataxin in Fe-S Cluster Biosynthesis.* Biochemistry, 2012. **51**(12): p. 2506-2514.

83.   Lill, R. and U. Mühlenhoff, *Maturation of Iron-Sulfur Proteins in Eukaryotes: Mechanisms, Connected Processes, and Diseases.* Annual Review of Biochemistry, 2008. **77**(1): p. 669-700.

84.   Campuzano, V., et al., *Friedreich's Ataxia: Autosomal Recessive Disease Caused by an Intronic GAA Triplet Repeat Expansion.* Science, 1996. **271**(5254): p. 1423-1427.

85.   Dürr, A., et al., *Clinical and Genetic Abnormalities in Patients with Friedreich's Ataxia.* New England Journal of Medicine, 1996. **335**(16): p. 1169-1175.

86.   Santos, R., et al., *Friedreich Ataxia: Molecular Mechanisms, Redox Considerations, and Therapeutic Opportunities.* Antioxidants & Redox Signaling, 2010. **13**(5): p. 651-690.

87.   Cossée, M., et al., *Friedreich's ataxia: Point mutations and clinical presentation of compound heterozygotes.* Annals of Neurology, 1999. **45**(2): p. 200-206.

88.   Zuhlke, C.H., et al., *Extension of the mutation spectrum in Friedreich's ataxia: detection of an exon deletion and novel missense mutations.* Eur J Hum Genet, 2004. **12**(11): p. 979-982.

89.   Schmucker, S. and H. Puccio, *Understanding the molecular mechanisms of Friedreich's ataxia to develop therapeutic approaches.* Human Molecular Genetics, 2010. **19**(R1): p. R103-R110.

90.   De Michele, G., et al., *Atypical Friedreich ataxia phenotype associated with a novel missense mutation in the X25 gene.* Neurology, 2000. **54**(2): p. 496-499.

91.   Bartolo, C., J.R. Mendell, and T.W. Prior, *Identification of a missense mutation in a Friedreich's ataxia patient: Implications for diagnosis and carrier studies.* American Journal of Medical Genetics, 1998. **79**(5): p. 396-399.

92.   Bridwell-Rabb, J., A.M. Winn, and D.P. Barondeau, *Structure-Function Analysis of Friedreich's Ataxia Mutants Reveals Determinants of Frataxin Binding and Activation of the Fe-S Assembly Complex.* Biochemistry, 2011. **50**(33): p. 7265-7274.

93.   Correia, A.R., et al., *Conformational stability of human frataxin and effect of Friedreich's ataxia-related mutations on protein folding.* Biochem J, 2006. **398**(3): p. 605-611.

94.   Correia, A.R., et al., *Dynamics, stability and iron-binding activity of frataxin clinical mutants.* FEBS Journal, 2008. **275**(14): p. 3680-3690.

95.   Diehl, B., et al., *Atypical, perhaps under-recognized? An unusual phenotype of Friedreich ataxia.* neurogenetics, 2010. **11**(2): p. 261-265.

96.   Forrest, S.M., et al., *The correlation of clinical phenotype in Friedreich ataxia with the site of point mutations in the FRDA gene.* neurogenetics, 1998. **1**(4): p. 253-257.

97.   Gellera, C., et al., *Frataxin gene point mutations in Italian Friedreich ataxia patients.* Neurogenetics, 2007. **8**(4): p. 289-299.

98.   McCormack, M.L., et al., *Frataxin point mutations in two patients with Friedreich's ataxia and unusual clinical features.* Journal of Neurology, Neurosurgery & Psychiatry, 2000. **68**(5): p. 661-664.

99.   Tsai, C.L., J. Bridwell-Rabb, and D.P. Barondeau, *Friedreich's Ataxia Variants I154F and W155R Diminish Frataxin-Based Activation of the Iron-Sulfur Cluster Assembly Complex.* Biochemistry, 2011. **50**(29): p. 6478-6487.

100.   Van Driest, S.L., et al., *Molecular and functional characterization of a human frataxin mutation found in hypertrophic cardiomyopathy.* Molecular Genetics and Metabolism, 2005. **85**(4): p. 280-285.

101. Roman, E.A., et al., *Protein Stability and Dynamics Modulation: The Case of Human Frataxin.* PLoS ONE, 2012. **7**(9).

102. Deutsch, E.C., et al., *A rapid, noninvasive immunoassay for frataxin: Utility in assessment of Friedreich ataxia.* Molecular Genetics and Metabolism, 2010. **101**(2-3): p. 238-245.

103. Correia, A.R., et al., *The conserved Trp155 in human frataxin as a hotspot for oxidative stress related chemical modifications.* Biochemical and Biophysical Research Communications, 2009. **390**(3): p. 1007-1011.

104. Hebert, Alexander S., et al., *Calorie Restriction and SIRT3 Trigger Global Reprogramming of the Mitochondrial Protein Acetylome.* Molecular cell, 2013. **49**(1): p. 186-199.

105. Rufini, A., et al., *Preventing the ubiquitin/proteasome-dependent degradation of frataxin, the protein defective in Friedreich's Ataxia.* Human Molecular Genetics, 2011.

106. Wagner, G.R., et al., *Friedreich's ataxia reveals a mechanism for coordinate regulation of oxidative metabolism via feedback inhibition of the SIRT3 deacetylase.* Human Molecular Genetics, 2012. **21**(12): p. 2688-2697.

107. Palmer, I. and P.T. Wingfield, *Preparation and Extraction of Insoluble (Inclusion-Body) Proteins from Escherichia coli*, *Current Protocols in Protein Science*. 2001, John Wiley & Sons, Inc.

108. Gill, S.C. and P.H. von Hippel, *Calculation of protein extinction coefficients from amino acid sequence data.* Analytical Biochemistry, 1989. **182**(2): p. 319-326.

109. Marelja, Z., et al., *A Novel Role for Human Nfs1 in the Cytoplasm: Nfs1 ACTS AS A SULFUR DONOR FOR MOCS3, A PROTEIN INVOLVED IN MOLYBDENUM COFACTOR BIOSYNTHESIS.* Journal of Biological Chemistry, 2008. **283**(37): p. 25178-25185.

110. Siegel, L.M., *A direct microdetermination for sulfide.* Analytical Biochemistry, 1965. **11**(1): p. 126-132.

111. Gakh, O., et al., *Normal and Friedreich ataxia cells express different isoforms of frataxin with complementary roles in iron-sulfur cluster assembly.* Journal of Biological Chemistry, 2010. **285**(49): p. 38486-38501.

112. Huang, R., et al., *Site-Specific Introduction of an Acetyl-Lysine Mimic into Peptides and Proteins by Cysteine Alkylation.* Journal of the American Chemical Society, 2010. **132**(29): p. 9986-9987.

113. Nagahara, N., et al., *Protein cysteine modifications: (1) medicinal chemistry for proteomics.* Current Medicinal Chemistry, 2009. **16**(33): p. 4419-4444.

114. Li, F.P., et al., *A Direct Method for Site-Specific Protein Acetylation.* Angewandte Chemie-International Edition, 2011. **50**(41): p. 9611-9614.

115. Yang, Y.Y. and H.C. Hang, *Chemical Approaches for the Detection and Synthesis of Acetylated Proteins.* Chembiochem, 2011. **12**(2): p. 314-322.

116.   Lane, D.J.R. and D.R. Richardson, *Frataxin, a molecule of mystery: trading stability for function in its iron-binding site.* Biochemical Journal, 2010. **426**(2): p. e1-e3.

117.   Shan, Y., E. Napoli, and G. Cortopassi, *Mitochondrial frataxin interacts with ISD11 of the NFS1/ISCU complex and multiple mitochondrial chaperones.* Human Molecular Genetics, 2007. **16**(8): p. 929-941.

118.   Gerber, J., U. Muhlenhoff, and R. Lill, *An interaction between frataxin and Isu1/Nfs1 that is crucial for Fe/S cluster synthesis on Isu1.* Embo Reports, 2003. **4**(9): p. 906-911.

119.   Prischi, F., et al., *Structural bases for the interaction of frataxin with the central components of iron-sulphur cluster assembly.* Nature Communications, 2010. **1**(7): p. 95-95.

120.   Cook, J.D., et al., *Molecular Details of the Yeast Frataxin−Isu1 Interaction during Mitochondrial Fe−S Cluster Assembly.* Biochemistry, 2010. **49**(40): p. 8756-8765.

121.   Prischi, F., et al., *Of the vulnerability of orphan complex proteins: The case study of the E. coli IscU and IscS proteins.* Protein Expression and Purification, 2010. **73**(2): p. 161-166.

122.   Vaubel, R.A. and G. Isaya, *Iron–sulfur cluster synthesis, iron homeostasis and oxidative stress in Friedreich ataxia.* Molecular and Cellular Neuroscience, (0).

123. Adinolfi, S., et al., *A structural approach to understanding the iron-binding properties of phylogenetically different frataxins.* Human Molecular Genetics, 2002. **11**(16): p. 1865-1877.

124. Harrison, P.M. and P. Arosio, *Ferritins: Molecular properties, iron storage function and cellular regulation.* Biochimica Et Biophysica Acta-Bioenergetics, 1996. **1275**(3): p. 161-203.

125. Söderberg, C.A.G., et al., *Oligomerization Propensity and Flexibility of Yeast Frataxin Studied by X-ray Crystallography and Small-Angle X-ray Scattering.* Journal of Molecular Biology, 2011. **414**(5): p. 783-797.

126. Gakh, O., et al., *Physical evidence that yeast frataxin is an iron storage protein.* Biochemistry, 2002. **41**(21): p. 6798-6804.

127. Gakh, O., D.Y. Smith, and G. Isaya, *Assembly of the iron-binding protein frataxin in Saccharomyces cerevisiae responds to dynamic changes in mitochondrial iron influx and stress level.* Journal of Biological Chemistry, 2008. **283**(46): p. 31500-31510.

128. Karlberg, T., et al., *The structures of frataxin oligomers reveal the mechanism for the delivery and detoxification of iron.* Structure, 2006. **14**(10): p. 1535-1546.

129. Park, S., et al., *Yeast frataxin sequentially chaperones and stores iron by coupling protein assembly with iron oxidation.* Journal of Biological Chemistry, 2003. **278**(33): p. 31340-31351.

130. Schagerlof, U., et al., *Structural basis of the iron storage function of frataxin from single-particle reconstruction of the iron-loaded oligomer.* Biochemistry, 2008. **47**(17): p. 4948-4954.

131. Soderberg, C.A.G., et al., *The molecular basis of iron-induced oligomerization of frataxin and the role of the ferroxidation reaction in oligomerization.* Journal of Biological Chemistry, 2013.

132. Li, H.Q., et al., *Oligomeric Yeast Frataxin Drives Assembly of Core Machinery for Mitochondrial Iron-Sulfur Cluster Synthesis.* Journal of Biological Chemistry, 2009. **284**(33): p. 21971-21980.

133. Layer, G., et al., *Iron-sulfur cluster biosynthesis - Characterization of Escherichia coli CyaY as an iron donor for the assembly of 2Fe-2S clusters in the scaffold IscU.* Journal of Biological Chemistry, 2006. **281**(24): p. 16256-16263.

134. Pastore, C., et al., *Understanding the binding properties of an unusual metal-binding protein - a study of bacterial frataxin.* FEBS Journal, 2007. **274**(16): p. 4199-4210.

135. Bedekovics, T., et al., *Partial conservation of functions between eukaryotic frataxin and the Escherichia coli frataxin homolog CyaY.* FEMS Yeast Research, 2007. **7**(8): p. 1276-1284.

136. O'Neill, H.A., O. Gakh, and G. Isaya, *Supramolecular assemblies of human frataxin are formed via subunit-subunit interactions mediated by a non-*

conserved amino-terminal region. Journal of Molecular Biology, 2005. **345**(3): p. 433-439.

APPENDIX A

TWO AZIDO-BRIDGED COPPER(II) COORDINATION POLYMERS WITH ISONICOTINATE-*N*-OXIDE AND PICOLINATE-*N*-OXIDE ACTING AS CO-LIGANDS,

ABSTRACT

Two one-dimensional coordination polymers $[Cu_{1.5}(\mathbf{L_1})(N_3)_2(H_2O)]_n$ (**1**) and $[Cu_{1.5}(\mathbf{L_2})(N_3)_2]_n$ (**2**) were synthesized by hydrothermal reactions of Cu(II) salt with NaN_3 in the presence of two secondary ligands, isonicotinate-N-oxide (**L₁**) and its isomer, picolinate-N-oxide (**L₂**). Single-crystal X-ray diffraction studies reveal that azide anions adopt a μ-1,1 bridging coordination mode linking the metal ions by both double and single azide bridges in **1**, but they adopt both μ-1,1 and μ-1,1,1 bridging modes in **2**. The magnetic measurements showed strong ferromagnetic coupling and the onset of magnetic ordering in **1** (a metamagnet with a small glass behaviour), but antiferromagnetic interactions between the ferromagnetic trimers in **2**. This result indicates that the judicious selection of co-ligands can effectively tune the formation of metal-azide coordination polymers and thereby, their magnetic properties.

INTRODUCTION

Molecule-based magnetic materials have been actively investigated in the past two decades due to their unique physical characteristics, such as slow relaxation and large hysteresis of magnetic properties [137-142]. These materials show great promise for potential applications in information storage, quantum computation, and so on [143-145]. Coordination chemistry provides a promising approach to design and prepare these materials by combining first-row transition metal ions with suitable ligands to form coordination polymers [146-152]. This method has been used to create various magnetic materials, such as single-molecule magnets (SMMs) and single-chain magnets (SCMs) [153-157]. Obviously, using short bridging ligands, like N_3^-, CN^-, $C_2H_3O_2^-$, $C_6H_5O^-$, and OH^-, allows for the mediation of the near-neighbour magnetic interaction, while the bridging or chelating co-ligands (secondary ligands) are able to tune structures and bulk magnetic properties [138, 158-163].

Among all these bridging entities, azide plays an important role as a mediator for magnetic exchange interaction between metal centers. The reasons are dual: (i) the remarkable ability of the azide ligand to transmit large ferro- or anti-ferromagnetic interaction when adopting the μ-1,1 end-on (EO) and μ-1,3 end-to-end (EE) bridging modes [164-165] and (ii) although it is rare, an azide anion can also link metal ions through triply bridging (μ_3-1,1,1 and μ_3-1,1,3) and quadruply bridging (μ_4-1,1,1,1, μ_4-1,1,1,3 and μ_4-1,1,3,3) modes to give unexpected magnetic behaviors [158, 166-169]. First-row transition metals have been combined with pyridine carboxylate N-oxide secondary ligand and azide anion to form 2D and 3D magnetic architectures [170-171].

The varied structures observed in these materials are due to the diverse coordination modes of azide anion, a fact which can further be exploited to create new compounds [172-173]. In this work the iso-nicotinate-N-oxide (**L₁**) and its isomeric compound, picolinate-N-oxide (**L₂**), were employed in the metal-azide system. Herein, we report the synthesis, structure, and magnetic properties of two new Cu(II)-azide coordination polymers $[Cu_{1.5}(\mathbf{L_1})(N_3)_2(H_2O)]_n$ (**1**) and $[Cu_{1.5}(\mathbf{L_2})(N_3)_2]_n$ (**2**) with the two structurally related anionic compounds as co-ligands, respectively.

EXPERIMENTAL SECTION

Materials and measurements

All the chemicals used for synthesis are of analytical grade and are commercially available. Elemental analyses (C, H, and N) were performed on a Heraeus CHN-Rapid elemental analyzer. FT-IR spectra (KBr pellet) were obtained on an FT-IR 170 SX (Nicolet) spectrometer with KBr pellets. XRPD patterns were obtained on a Scintag X1 powder diffractometer system using Cu-K$_\alpha$ radiation with a variable divergent slit, solid-state detector, and a routine power of 1400 W (40 kV and 35 mA). Simulation of the XRPD spectrum was carried out by the single-crystal data and diffraction-crystal module of the Mercury program which is available free of charge via the internet at http://www.iucr.org. Magnetic data were collected using crushed crystals of the sample on a Quantum Design PPMS-9T magnetometer. The data were corrected using Pascal's constants to calculate the diamagnetic susceptibility. During the magnetic measurement,

the powder sample was enwrap by a film, then fixed in the tube for measurement and the background of the film was corrected.

Crystallography

The single crystal X-ray diffraction measurement was carried out on a Bruker Smart 1000 CCD area detector. Intensities of reflections were measured using graphite-monochromatized Mo-K$_\alpha$ radiation (λ = 0.71073 Å) with ω scan mode at 293(2) K in the range of 2.07 < θ < 27.94° for **1** and 3.79 < θ < 27.46° for **2**, respectively. Unit cell dimensions were obtained with least-squares refinements and semi-empirical absorption corrections were applied using SADABS program.(ref 10) The structure was solved by the direct method (ref 11) and non-hydrogen atoms were obtained in successive difference Fourier syntheses. Hydrogen atoms of C were included in calculated positions and refined with fixed thermal parameters riding on their parent atoms. Hydrogen of water were located on difference Fourier maps and refined isotropically with $U_{iso}(H)$ = 1.2U_{eq}. The crystallographic data for **1** and **2** are listed in Table 1.

Synthesis of [Cu$_{1.5}$(L$_1$)(N$_3$)$_2$(H$_2$O)]$_n$ (1)

A mixture of Cu(NO$_3$)$_2$·3H$_2$O, NaN$_3$, HL$_1$, and H$_2$O at a mole ratio of 4 : 2 : 3 : 1000 was sealed in a Teflon-lined autoclave, heated to 140 °C for 3 days, and cooled to 100 °C at a rate of 10 °C h^{-1}; at this temperature the system was held for an additional 12 hours, and then cooled to room temperature naturally. The dark-green crystals were collected in *ca.* 20% yield based on copper. FT-IR (KBr pellet, cm^{-1}): 3322s, 3115m,

2551m, 2471m, 2351w, 2101s, 2083s, 1684w, 1628s, 1554s, 1415s, 1295m, 1221m, 1147m, 1092w, 1026w, 870m, 813w, 783m, 693m, 647m, 573w, 508m. Anal. Calcd for $C_{12}H_{12}Cu_3N_{14}O_8$: C, 21.48; H, 1.80; N, 29.23. Found: C, 21.33; H, 1.75; N, 29.55.

Synthesis of $[Cu_{1.5}(L_2)(N_3)_2]_n$ (2)

Compound **2** was synthesized in the same manner as described for **1**. The dark-green crystals collected in *ca.* 32% yield based on copper. FT-IR (KBr pellet, cm^{-1}): 3450m, 3330m, 3123m, 3091m, 2567w, 2384w, 2102s, 2090s, 1624s, 1605s, 1446s, 1350s, 1271s, 1208m, 1159m, 1096w, 1049w, 985w, 866m, 810m, 762s, 715m, 675m, 611m, 508m. Anal. Calcd for $C_{12}H_8Cu_3N_{14}O_6$: C, 22.70; H, 1.27; N, 30.88. Found: C, 22.63; H, 1.32; N, 31.22.

Table 1 Crystallographic data for **1** and **2**

	1	2
Empirical formula	$Cu_3N_{14}O_8C_{12}H_{12}$	$Cu_3N_{14}O_6C_{12}H_8$
Fw	670.98	634.94
Crystal system	Triclinic	Triclinic
Space group	$P\bar{1}$	$P\bar{1}$
T/K	293	293
a/Å	6.5724(15)	5.2676(11)
b/Å	8.922(2)	10.446(2)
c/Å	10.621(4)	10.739(2)
α/°	108.461(5)	116.41(3)
β/°	94.233(5)	103.82(3)
γ/°	110.179(3)	92.64(3)
V/Å^3	542.6(3)	506.0(18)
Z	1	1
D_{calcd}/g cm^{-3}	2.053	2.098
μ/mm^{-1}	2.989	6.218
Independent reflections	3349	2307
R_{int}	0.0104	0.0212
$R[I/\sigma(I) > 2]$	0.0242	0.0269
$R_w[I/\sigma(I) > 2]$	0.0667	0.0761
Goodness-of-fit on F^2	1.079	1.164
No. of reflections used	2421	2307
No. of parameters refined	177	160
$\Delta\rho_{max}$/e Å^{-3}	0.345	0.323
$\Delta\rho_{min}$/e Å^{-3}	−0.562	−0.384

RESULTS AND DISCUSSION

Synthesis and general characterization

The two compounds were prepared by the hydrothermal reaction under autogenous pressure. The IR spectra of **1** and **2** display characteristic absorption peaks in the range of 2102–2089 cm^{-1} for the coordinated azides. The middle strong broad peaks centred at *ca.* 3322 and 3450 cm^{-1} indicate O–H stretching of aqua molecules. The strong peaks at 1684 and 1624 cm^{-1} can be assigned to the C=O stretching of –COO^{-} groups; the peaks at 1628 and 1605 cm^{-1} belong to the N=O stretching of *N*-oxide groups; and the absorption bands resulting from skeletal vibrations of the aromatic ring appear in the 1554–1415 cm^{-1} region. XRPD patterns show that most of the peaks in **1** and **2** are matched with the simulation spectrum. However, the slight differences between simulation spectrum and measurement data indicate that the minor impurity happened in these two complexes (ESI, Fig. S1 and S2†).

Crystal structure of 1 and 2

Complex **1** crystallized in the triclinic space group $P\bar{1}$. A perspective view of a trinuclear fragment of the chain is shown in Fig. 1a and the selected bond lengths and angles are listed in Table 2. The common structural feature of **1** is a one-dimensional (1D) Cu–N$_3^{-}$/COO^{-} chain composed of metal ions linked by double EO azide bridges and single EO azide with one syn–syn carboxylate bridges alternatively. To our knowledge, this kind of linkage has scarcely been reported before [171, 174].
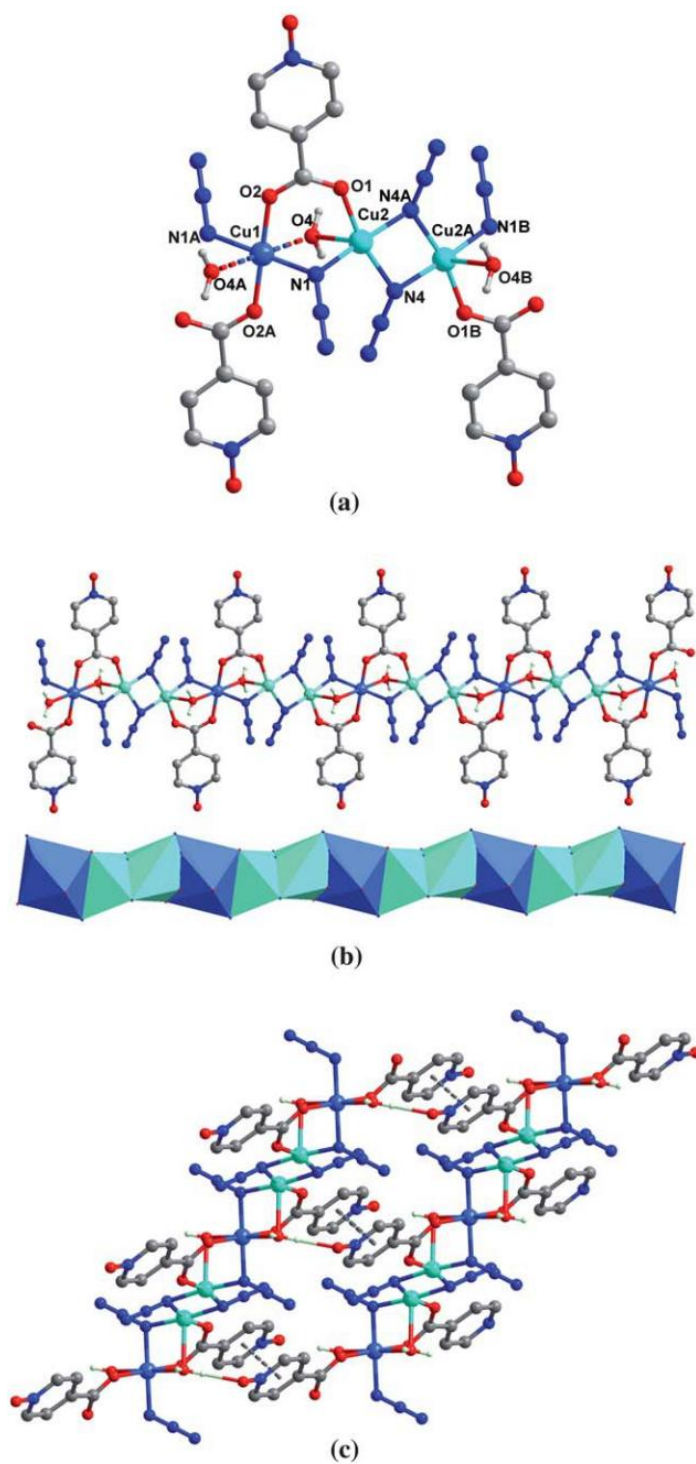
Fig. 1 (a) View of the trinuclear unit in **1** (highlighting the coordination environment of Cu(II) atom); (b) view of 1D chain in **1**; (c) view of 2D layer showing the π-π interactions between adjacent chains.

110

Table 2 Selected bond distances (Å) and angles (°) in **1**[a]

Cu(1)–O(2)[a]	1.9616(16)	Cu(1)–O(2)	1.9616(16)
Cu(1)–N(1)[a]	2.0081(17)	Cu(1)–N(1)	2.0081(17)
Cu(1)–O(4)	2.500(2)	Cu(1)–Cu(2)	3.114(2)
Cu(2)–O(1)	1.9485(15)	Cu(2)–N(1)	1.9749(17)
Cu(2)–N(4)	1.9817(18)	Cu(2)–N(4)[b]	2.0043(18)
Cu(2)–O(4)	2.3757(18)	Cu(2)–Cu(2)[b]	3.0404(8)
N(4)–Cu(2)[b]	2.0043(17)		
O(2)[a]–Cu(1)–O(2)	180	O(2)[a]–Cu(1)–N(1)[a]	91.33(7)
O(2)–Cu(1)–N(1)[a]	88.67(7)	O(2)[a]–Cu(1)–N(1)	88.67(7)
O(2)–Cu(1)–N(1)	91.33(7)	N(1)[a]–Cu(1)–N(1)	180.000(1)
Cu(1)–O(4)–Cu(2)	79.333	O(1)–Cu(2)–N(1)	91.88(7)
O(1)–Cu(2)–N(4)	166.48(7)	N(1)–Cu(2)–N(4)	97.52(7)
O(1)–Cu(2)–N(4)[b]	89.14(7)	N(1)–Cu(2)–N(4)[b]	174.39(8)
N(4)–Cu(2)–N(4)[b]	80.58(8)	O(1)–Cu(2)–O(4)	92.19(6)
N(1)–Cu(2)–O(4)	86.74(7)	N(4)–Cu(2)–O(4)	98.02(7)
N(4)[b]–Cu(2)–O(4)	98.74(7)	O(1)–Cu(2)–Cu(2)[b]	128.60(5)
N(1)–Cu(2)–Cu(2)[b]	137.84(5)	N(4)–Cu(2)–Cu(2)[b]	40.57(5)
N(4)[b]–Cu(2)–Cu(2)[b]	40.02(5)	O(4)–Cu(2)–Cu(2)[b]	101.01(4)
Cu(2)–N(4)–Cu(2)[b]	99.42(8)	Cu(2)–N(4)[b]–Cu(2)[b]	99.42(8)

[a] Symmetry operators: [a] $= -x + 1, -y + 1, -z + 1$; [b] $= -x + 1, -y + 2, -z + 1$.

There are two crystallographically independent Cu(II) ions, Cu1 and Cu2 in the crystal asymmetric unit. The Cu1 ion (light blue in Fig. 1a) is located at an inversion center, and its coordination environment is an elongated octahedron in which the equatorial plane is made up of two carboxylate oxygen atoms from two isonicotiniate-*N*-oxide and two nitrogen atoms from two azide anions and the axial sites are occupied by two oxygen atoms from coordinated water molecules. The equatorial Cu1–N/O distances of 2.0081(17) and 1.9616(16) Å are significantly shorter than the axial Cu1–O distances of 2.500 Å, but match those observed in related compounds [170, 175-176]. Except the EO azide anions and the *syn–syn* carboxylate bridges, one oxygen atom from

the coordinated water molecule links the adjacent Cu1 and Cu2 ions additionally with the angles of Cu1–N2–Cu2 and Cu1–O4–Cu2 being 102.85° and 79.333°, respectively, and the distance between Cu1 and Cu2 is 3.114 Å.

Cu2 (cyan in Fig. 1a) is coordinated by three nitrogen atoms from three azide anions, one oxygen atom from the carboxylate moiety, and one oxygen atom from a coordinated water molecule. The distances of Cu2–N are slightly different: 1.9749 Å for Cu2–N1, 1.9817 Å for Cu2–N4 and 2.0043 Å for Cu2–N4A, which match other Cu–N_3 systems [177-179]. The distance of Cu2–O4 and Cu2–O2 is 2.3757 and 1.9485 Å, respectively. The adjacent Cu2 ions were joined by the double EO azide bridges with the same Cu2–N4–Cu2A and Cu2–N4A–Cu2A angles of 99.42°. The distance between Cu2 and Cu2A is 3.0404 Å. The feature of the chains along the crystallographic axis *b* is exhibited as helices as shown in Fig. 1b. The shortest Cu(II) ions separation within the chains is 9.718 Å, with additional weak interactions presenting between the adjacent chains (Fig. 1c) [180-181]. The pyridine rings in adjacent chains are aligned in an off-set fashion, lying approximately parallel to each other with a center–center distance of *ca*. 4.205 Å, indicating the presence of face-to-face π/π stacking [182-183]. Hydrogen bonding of O–H··O is observed between the hydrogen of the coordinated water molecule and the *N*-oxide group of isonicotinate-*N*-oxide. The hydrogen bond parameters are presented in Table 3. These weak interactions extend the 1D chain structure of **1** to a two-dimensional (2D) supramolecular network layer.

Table 3 O–H···O hydrogen bond parameters in **1**[a]

D–H···A	D–H/Å	H···A/Å	D···A/Å	<D–H···A/°
O(4)–H(4B)···O(3)[c]	0.848(10)	1.985(17)	2.768(2)	153(3)
O(4)–H(4C)···O(3)[d]	0.842(10)	1.878(12)	2.706(2)	167(3)

[a] Symmetry operators: [c] = $x + 1$, $y + 1$, $z + 1$; [d] = $-x + 1$, $-y + 1$, $-z$.

2 crystallized in the triclinic space group $P1\bar{}$ and the common structural feature of **2** is also a 1D Cu–N_3^-/COO$^-$ chain composed of metal ions linked by both EO (μ-1,1) and the μ-1,1,1 bridging azides, and one *syn–syn* carboxylate bridges, but structurally is different from that of **1**. The selected bond lengths and angles are listed in Table 4. As shown in Fig. 2a, **2** consists of two Cu(II) ions Cu1 and Cu2. Each Cu1 (light blue in Fig. 2a) having a distorted octahedral coordination environment is coordinated by three nitrogen atoms from three azide anions, two carboxylate oxygen atoms from two picolinate-*N*-oxide co-ligands and one oxygen from the *N*-oxide group of picolinate-*N*-oxide ligand. Comparing the Cu1–N2 (1.987 Å) and Cu1–N5 (2.016 Å) bond distances with that of the axial Cu1–N5A (2.657 Å), it is clear that there is a distinct difference for the equatorial *vs*. the axial Cu–N bonds of the structure. These bond distances are consistent with the previously reported value [184]. Cu2 (cyan in Fig. 2a) also has an octahedral coordination environment with the four nitrogen atoms from four azide anions in the equatorial plane and two carboxylate oxygen atoms from two picolinate-*N*-oxide ligands in the axial positions. The angle of Cu1–N(N3$^-$)–Cu2 is 97.22(10)° for Cu1–N2–Cu2 and 96.05(9)° for Cu1–N5–Cu2. Thus the 1D chain of **2**

can be described as two double azide anions bridge of Cu_3 trimers linked by the weakly coordinated bonds in the axial positions. Each Cu(II) atom in the trimer, Cu1, Cu2, and Cu1A, is ranged in a line; and two Cu1 ions and one Cu2 ion exhibit an alternating pattern to form a 1D rhombic chain (Fig. 2b).
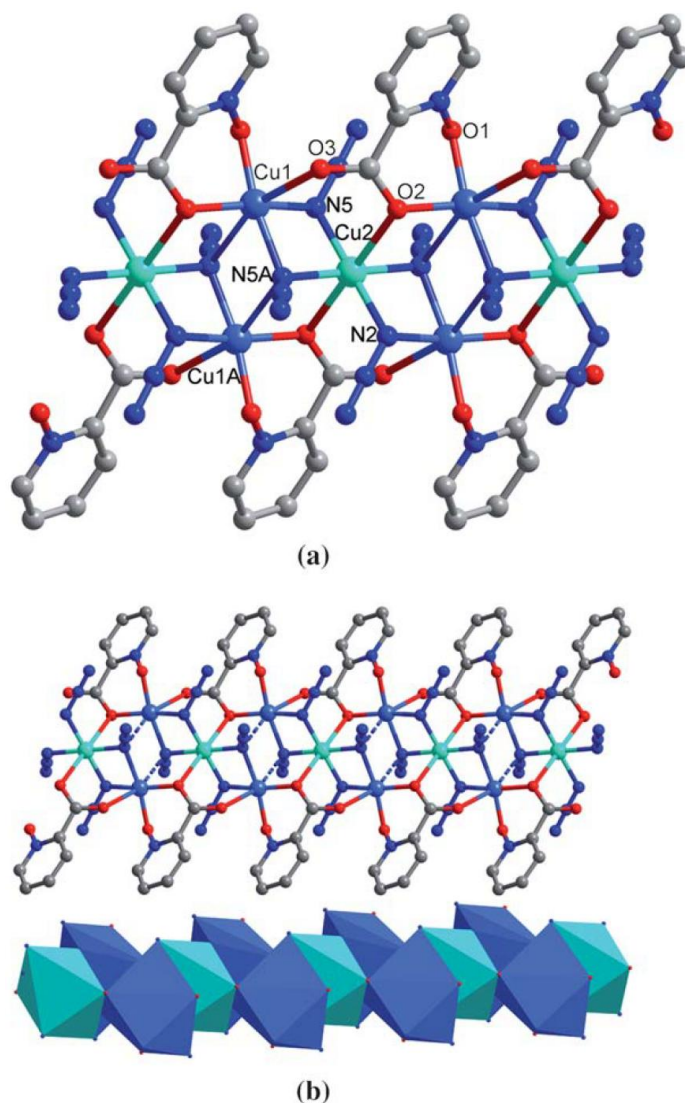

(a)

(b)

Fig. 2 (a) View of structural unit showing the coordination environment of Cu(II) in **2**; (b) view of 1D chain in **2**.

Table 4 Selected bond distances (Å) and angles (°) in **2**[a]

Cu(1)–O(1)	1.9205(18)	Cu(1)–O(2)	1.9498(19)
Cu(1)–N(2)	1.987(2)	Cu(1)–N(5)	2.016(2)
Cu(1)–Cu(2)	2.9832(13)	Cu(2)–N(1)	1.9749(17)
Cu(2)–N(2)	1.989(2)	Cu(2)–N(5)	1.996(2)
O(1)–Cu(1)–O(2)	89.74(8)	O(1)–Cu(1)–N(2)	92.45(9)
O(2)–Cu(1)–N(2)	166.27(8)	O(1)–Cu(1)–N(5)	170.74(8)
O(2)–Cu(1)–N(5)	97.48(8)	N(2)–Cu(1)–N(5)	81.91(9)
O(1)–Cu(1)–Cu(2)	130.99(6)	O(2)–Cu(1)–Cu(2)	139.17(6)
N(2)–Cu(1)–Cu(2)	41.42(7)	N(5)–Cu(1)–Cu(2)	41.72(6)
N(2)[a]–Cu(2)–N(2)	180 (1)	N(2)[a]–Cu(2)–N(5)	97.63(9)
N(2)–Cu(2)–N(5)	82.37(9)	N(2)[a]–Cu(2)–Cu(1)	138.63(6)
N(2)–Cu(2)–Cu(1)	41.37(6)	N(5)–Cu(2)–Cu(1)	42.23(6)
Cu(1)–Cu(2)–Cu(1)[a]	180(1)		

[a] Symmetry operator: [a] = −x, −y, −z + 1.

Magnetic properties of 1 and 2

Magnetic measurements were carried out on crystalline samples of **1** from 2 to 300 K. A plot of $\chi_m T$ *vs.* T for **1** is shown in Fig. 3, where χ_m is the magnetic susceptibility for three Cu(II) ions. At 300 K the $\chi_m T$ value is 1.35 cm^3 K mol^{-1}, larger than the predicted 1.05 cm^3 K mol^{-1} for three isolated Cu(II) ions ($S = 1/2$) with $g = 2.0$. As temperature decreases, $\chi_m T$ increases smoothly reaching a maximum value of 15.30 cm^3 K mol^{-1} at 4 K and then decreases to 10.69 cm^3 K mol^{-1}. This kind of curve is a typical signature of a strongly coupled ferromagnetic system, with antiferromagnetic coupling between the chains, noticeable only at very low temperatures that are identical with the similar complexes with the same chain structure but with different carboxylate [174]. The rapid increase of the curve at low field indicates strong ferromagnetic coupling and the onset of magnetic ordering (Fig. 4).
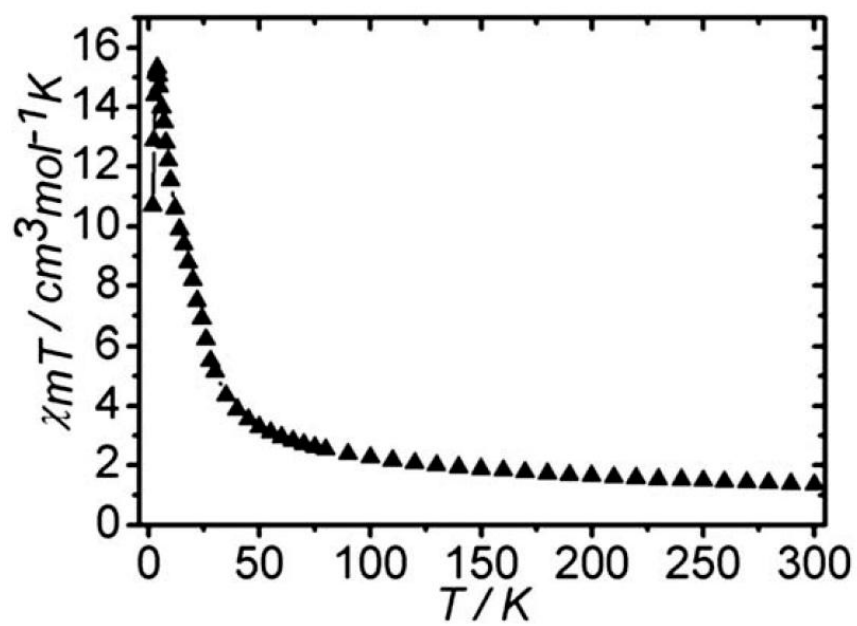
Fig. 3 Thermal variation of $\chi_m T$ of **1** at 2 kOe.
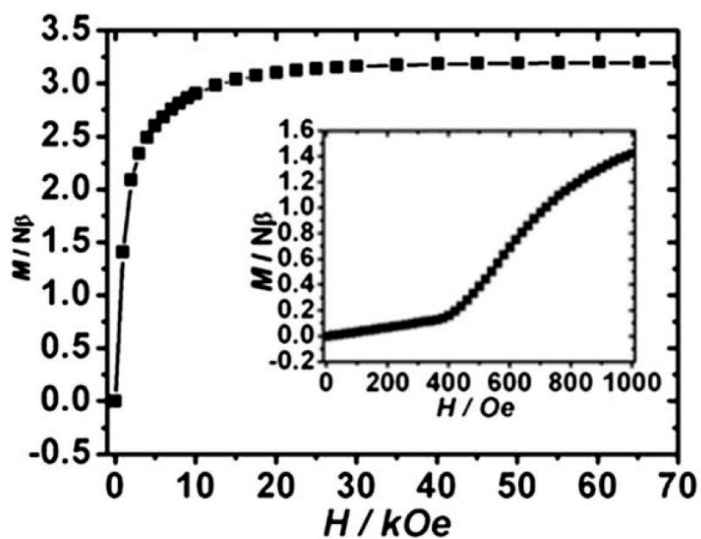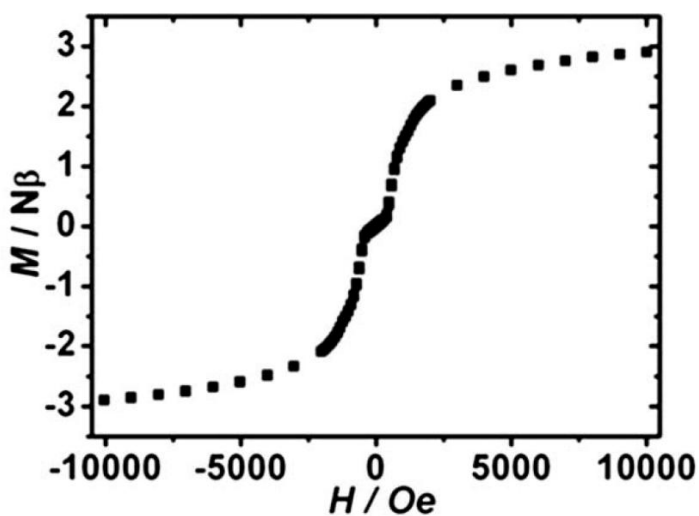
Fig. 4 (a) The magnetization *vs.* field plot of **1** at 2.0 K. (b) Hysteresis loop of **1** at 2 K.

The isothermal field dependent magnetizations $M(H)$ at 2 K and fields up to 70 kOe were measured for **1**. The field dependence of the magnetization does not follow a Brillouin curve. As shown in Fig. 4a, the curves rise sharply to the saturation value of 3.2 Nβ for **1** in agreement with three Cu(II) ions. However at low field a sigmoidal-

shaped curve is observed with a critical field of 400 Oe. This indicates that the coupling between the chains is antiferromagnetic and **1** is a metamagnet. In addition, no obvious hysteresis loop was observed (Fig. 4b).

The ac susceptibilities in a field of 5 Oe oscillating at 1–1000 Hz (Fig. 5) show a peak around 3 K in the in-phase curves without the corresponding peak in out-of-phase ones, indicating a zero ground state spin in **1**. Namely, **1** is antiferromagnetic under this measuring condition, which is consistent with the variable-field magnetization. At low temperature below 2.5 K, a weak frequency dependence of out-of-phase χ_m" is observed. The shift of the peak temperature (T_p) of χ_m" characterized by a parameter (φ) {(φ) = $\Delta T_p/[T_p\Delta(\log f)]$} is about 0.07, indicating a canonical spin glass in **1**. It is suggested that the frequency-dependent behaviour probably results from the magnetic properties of the chain. This similar situation has been observed in other chain coordination polymers [185-187]. In complex **1** the inphase and out-of-phase peaks do not appear at an exact temperature which may be due to the moving of the domain wall that is familiar in some low dimensional complexes. It is more likely that in the complex the moments within the chain order first and then the 3D ordering takes place. A plot of χ_mT *vs.* T and χ_m *vs.* T for **2** is shown in Fig. 6, where χ_m is the magnetic susceptibility for the three Cu(II) ions. At 300 K the χ_mT value is 1.53 cm^3 K mol^{-1}, much larger than the predicted 1.05 cm^3 K mol^{-1} for three isolated Cu(II) ions (S = 1/2) with g = 2.0, suggesting the ferromagnetic coupling between Cu(II) ions in the trimer [188-190]. With the decrease of temperature, χ_mT increases to 1.68 cm^3 K mol^{-1} at about 25 K then drops to 0.75 cm^3 K mol^{-1} at 2 K which may indicate an antiferromagnetic coupling between the trimers. **2**

is a 1D structure in which neighbour azide bridged trimers were linked by the weakly

coordinated bonds in the axial positions of each Cu(II) ion. And the magnetic behaviour

is mainly the characteristic of the trimer, for the inter-trimer coupling is weak and is only

significant at very low temperature. Thus the ferromagnetic magnetic orbital

interactions between the Cu(II) ions in the trimer should be mainly conducted by the

double μ-1,1-azido anions with Cu–N– Cu angles near 98 [191-194]. In order to

evaluate the magnitude of the interactions conducted by each bridge, a simulation of the

magnetic data was carried out with a trimer mode based on the Hamiltonian $\mathbf{H}$ = -

$2J(\mathbf{S}_{Cu1}\mathbf{S}_{Cu2} + \mathbf{S}_{Cu2}\mathbf{S}_{Cu1B})$, and the interactions between the trimers transferred by weakly

coordinated carboxylate groups and azide ions in axial positions of Cu(II) atoms were

taken into account by the molecular field approximation: [195]

$$\chi_M = \frac{\chi_{trimer}}{1 - \left(2zj'/Ng^2\beta^2\right)\chi_{trimer}}$$

The best fitting parameter above 25 K gives J_I = 21.78 cm^{-1}, zJ' = -2.61 cm^{-1}, g = 2.28

and R = 1.2 x 10^{-5} (R = [$(\chi_m T)_{obs}$ - $(\chi_m T)_{calc}$]^2/[$(\chi_m T)_{obs}$]^2). Those values are consistent

with the structure character of **2** and indicate that the cooperativity of the weakly

coordinated carboxylate groups and azide ions results in the antiferromagnetic coupling

between the trimers. Below 25 K the magnetic data show that this mode for the

interactions conducted by the weakly coordinated bonds is significant at low temperature

and **2** behaves as a magnetic chain. The magnetization at 2 K that increases linearly with

the field and reaches saturation of 3 Nβ at 50 KOe (Fig. 7) also confirms the antiferromagnetic interaction between the ferromagnetic trimers in **2**.

In summary, we have synthesized two new Cu(II)-azide 1D coordination polymers with different structures, which are tuned by different co-ligands. **1** features a μ-1,1 azide coordination mode to link the Cu(II) atoms by both double EO and single EO azide bridges. **2** has a μ-1,1 and μ-1,1,1 mixed bridging mode of azide anions. The magnetic measurements show that **1** has strong ferromagnetic coupling and the onset of magnetic ordering, while **2** presented antiferromagnetic coupling between the ferromagnetic Cu(II) trimers. This result indicates that the judicious selection of co-ligands can effectively tune the formation of metal-azide coordination polymers and thereby, their magnetic properties.
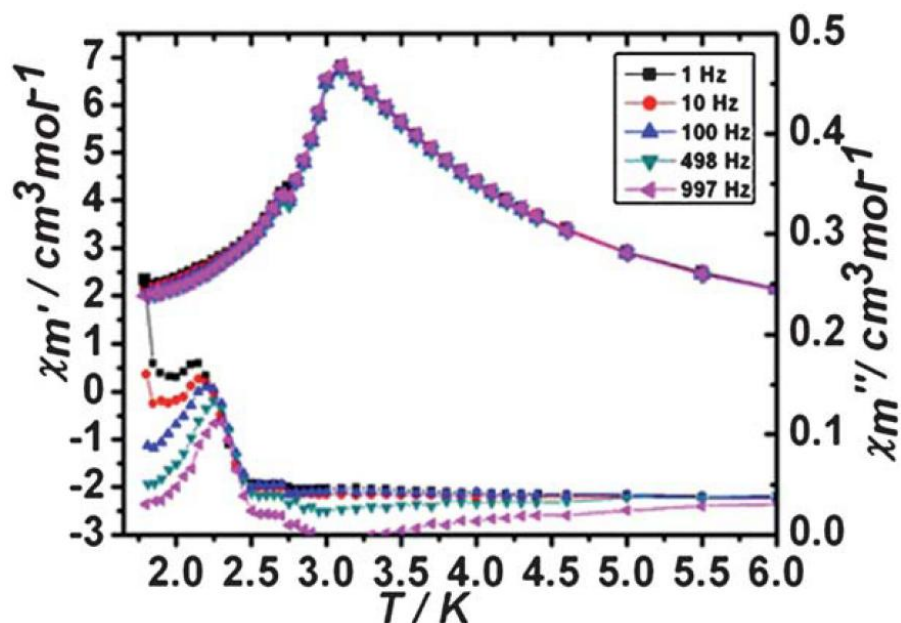
Fig. 5 The ac magnetic susceptibility at different frequencies for **1**.
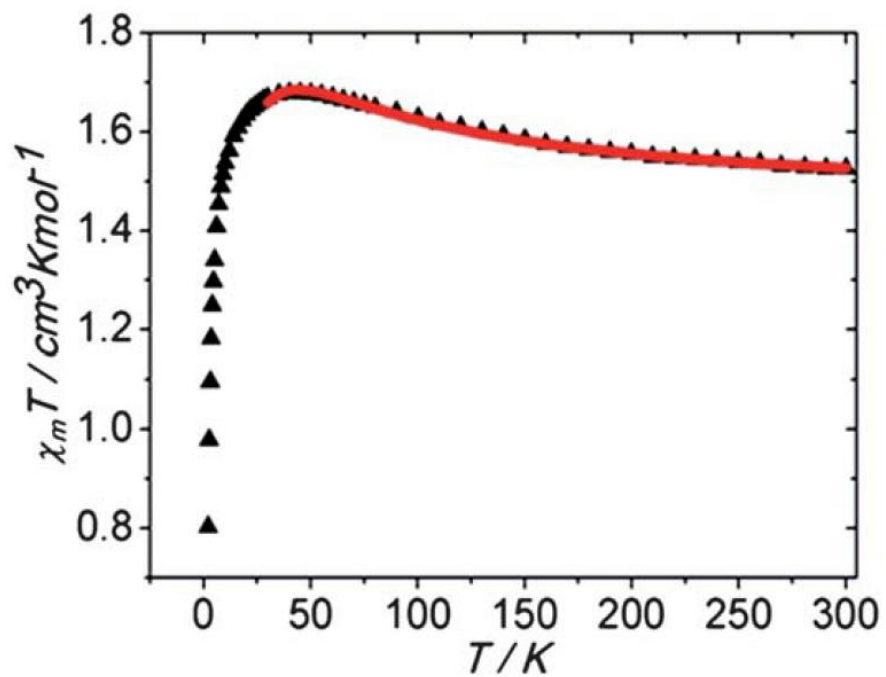
Fig. 6 Thermal variation of $\chi_m T$ at 1 kOe for **2** (red line represents the fitting result of the data).
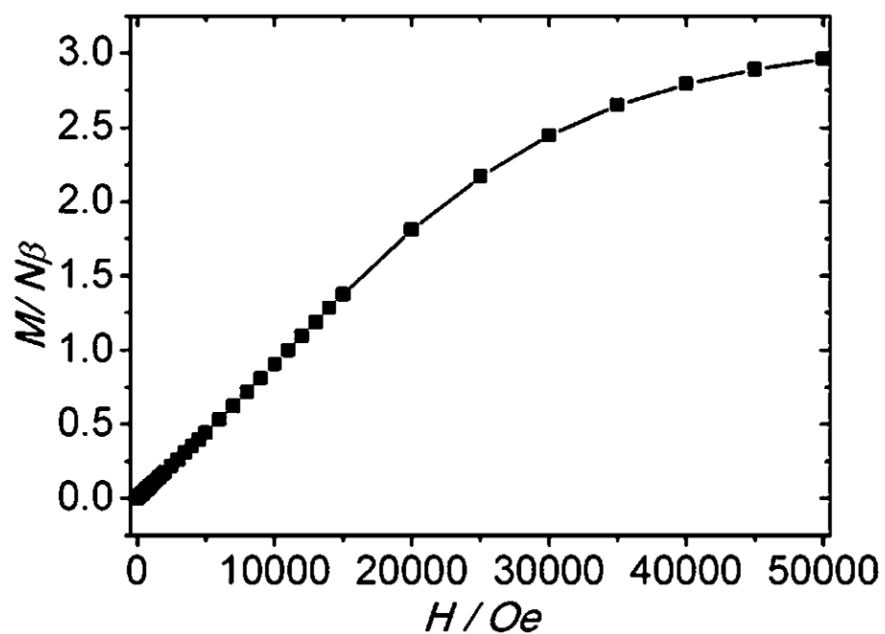
Fig. 7 The magnetization *vs.* field plot of **2** at 2.0 K.

SUPPORTING INFORMATION

XRPD results of **1** and **2** are shown below. The slight difference between simulation spectrum and measurement data indicate the minor impurity happened in these two compounds.

ESI-figure 1. The XRPD result of **1**.

ESI-figure 2. The XRPD result of **2**.

REFERENCES

137.   Bogani, L., et al., *Molecular engineering for single-chain-magnet behavior in a one-dimensional dysprosium-nitronyl nitroxide compound.* Angewandte Chemie-International Edition, 2005. **44**(36): p. 5817-5821.

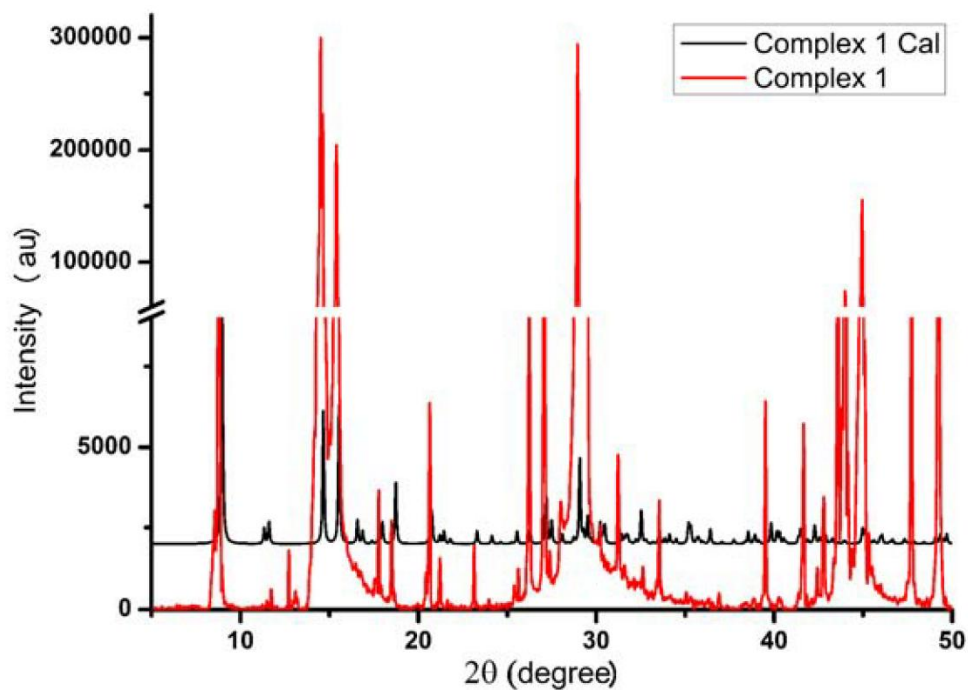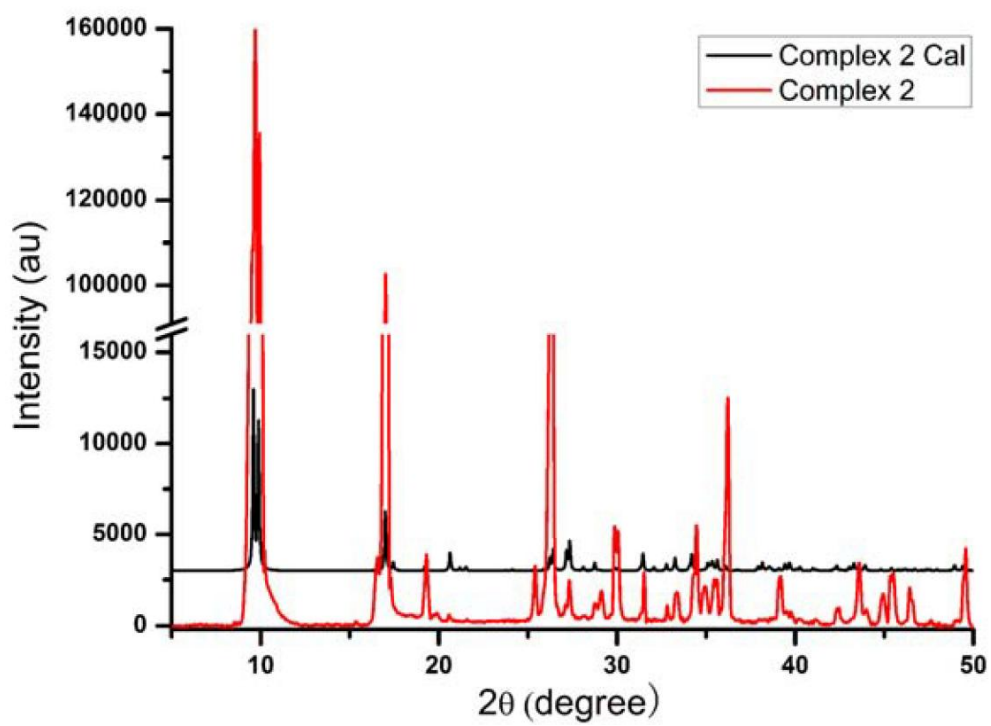138.   Ferbinteanu, M., et al., *Single-chain magnet (NEt4) Mn-2(5-MeOsalen)(2)Fe(CN)(6) made of Mn-III-Fe-III-Mn-III trinuclear single-molecule magnet with an ST = (9)/(2) spin ground state.* Journal of the American Chemical Society, 2005. **127**(9): p. 3090-3099.

139.   Kajiwara, T., et al., *A single-chain magnet formed by a twisted arrangement of ions with easy-plane magnetic anisotropy.* Journal of the American Chemical Society, 2005. **127**(29): p. 10150-10151.

140.   Ribas, J., et al., *Polynuclear Ni-II and Mn-II azido bridging complexes. Structural trends and magnetic behavior.* Coordination Chemistry Reviews, 1999. **193-5**: p. 1027-1068.

141.   Sessoli, R. and A.K. Powell, *Strategies towards single molecule magnets based on lanthanide ions.* Coordination Chemistry Reviews, 2009. **253**(19-20): p. 2328-2341.

142.   Zeng, M.H., et al., *A Unique Cobalt(II)-Based Molecular Magnet Constructed of Hydroxyl/Carboxylate Bridges with a 3D Pillared-Layer Motif.* Inorganic Chemistry, 2010. **49**(14): p. 6436-6442.

143.   Clerac, R., et al., *Evidence for single-chain magnet behavior in a Mn-III-Ni-II chain designed with high spin magnetic units: A route to high temperature*

metastable magnets. Journal of the American Chemical Society, 2002. **124**(43): p. 12837-12844.

144.   Leuenberger, M.N. and D. Loss, *Quantum computing in molecular magnets.* Nature, 2001. **410**(6830): p. 789-793.

145.   Liu, T.F., et al., *An azide-bridged homospin single-chain magnet: Co(2,2'-bithiazoline)(N-3)(2) (n).* Journal of the American Chemical Society, 2003. **125**(46): p. 13976-13977.

146.   Coulon, C., H. Miyasaka, and R. Clerac, *Single-chain magnets: Theoretical approach and experimental systems*, in *Single-Molecule Magnets and Related Phenomena*, R. Winpenny, Editor. 2006. p. 163-206.

147.   Dai, F., et al., *Self-assembly of a novel metal-organic coordination cage (MOCC) based on a new flexible dicarboxylate ligand: synthesis, crystal structure and magnetic property.* Crystengcomm, 2009. **11**(1): p. 47-49.

148.   Hilfiger, M.G., et al., *An Unprecedented Charge Transfer Induced Spin Transition in an Fe-Os Cluster.* Angewandte Chemie-International Edition, 2010. **49**(8): p. 1410-1413.

149.   Li, J.R., et al., *An azido-Cu-II-triazolate complex with utp-type topological network, showing spin-canted antiferromagnetism.* Chemical Communications, 2007(25): p. 2602-2604.

150.   Li, J.R., et al., *Magnetic canting or not? Two isomorphous 3D Co-II and Ni-II coordination polymers with the rare non-interpenetrated (10,3)-d topological*

network, showing spin-canted antiferromagnetism only in the Co-II system. Chemical Communications, 2007(22): p. 2290-2292.

151. Miyasaka, H., et al., *Single-chain magnet behavior in an alternated one-dimensional assembly of a Mn-III Schiff-base complex and a TCNQ radical.* Chemistry-a European Journal, 2006. **12**(27): p. 7029-7040.

152. Xu, H.-B., et al., *Stringing Oxo-Centered Trinuclear [MnIII3O] Units into Single-Chain Magnets with Formate or Azide Linkers.* Angewandte Chemie International Edition, 2007. **46**(39): p. 7388-7392.

153. Chen, Q., et al., *Hydrogen-Bonded Dicubane Co-7(II) Single-Molecule-Magnet Coordinated by in Situ Solvothermally Generated 1,2-Bis(8-hydroxyquinolin-2-yl)-ethane-1,2-diol Arranged in a Trefoil.* Chemistry of Materials, 2010. **22**(6): p. 2114-2119.

154. Jeon, I.R., et al., *Two-dimensional assembly of (Mn2Mn2II)-Mn-III single-molecule magnets and Cu(pic)(2) linking units (Hpic = picolinic acid).* Dalton Transactions, 2010. **39**(20): p. 4744-4746.

155. Miyasaka, H., et al., *Slow Dynamics of the Magnetization in One-Dimensional Coordination Polymers: Single-Chain Magnets.* Inorganic Chemistry, 2009. **48**(8): p. 3420-3437.

156. Miyasaka, H., et al., *Three-Dimensional Antiferromagnetic Order of Single-Chain Magnets: A New Approach to Design Molecule-Based Magnets.* Chemistry-a European Journal, 2010. **16**(12): p. 3656-3662.

157. Murrie, M., *Cobalt(II) single-molecule magnets.* Chemical Society Reviews, 2010. **39**(6): p. 1986-1995.

158. Escuer, A. and G. Aromi, *Azide as a bridging ligand and magnetic coupler in transition metal clusters.* European Journal of Inorganic Chemistry, 2006(23): p. 4721-4736.

159. Ma, Y., et al., *Mixed azide-carboxylate bridged tri- and tetranuclear Mn-II clusters in coordination polymers derived from a zwitterionic dicarboxylate ligand: structures and magnetism.* Dalton Transactions, 2010. **39**(33): p. 7714-7722.

160. Massoud, S.S., et al., *Dinuclear and polynuclear bridged azido-nickel(II) complexes: Synthesis, structure determination, and magnetic properties.* European Journal of Inorganic Chemistry, 2007(8): p. 1091-1102.

161. Tasiopoulos, A.J., et al., *Giant single-molecule magnets: A {Mn-84} torus and its supramolecular nanotubes.* Angewandte Chemie-International Edition, 2004. **43**(16): p. 2117-2121.

162. Tian, C.B., et al., *Cluster-Based Cu-II-Azide Polymers: Synthesis, Structure, Magnetic Properties, and Effect of Polyamines on Crystal Structures.* European Journal of Inorganic Chemistry, 2010(3): p. 427-437.

163. Wilson, D.C., et al., *Water-Free Rare Earth-Prussian Blue Type Analogues: Synthesis, Structure, Computational Analysis, and Magnetic Data of {Ln(III)(DMF)(6)Fe-III(CN)(6)}(infinity) (Ln = Rare Earths Excluding Pm).* Inorganic Chemistry, 2009. **48**(13): p. 5725-5735.

164.	Song, X.Y., et al., *One-dimensional copper(II) complex containing alternate single and double end-on azide ligands: Crystal structure and magnetic characterization.* Inorganic Chemistry Communications, 2007. **10**(5): p. 567-570.

165.	Stamatatos, T.C., et al., *Ferromagnetic coupling in a 1D coordination polymer containing a symmetric Cu (mu(1,1)-N-3)(2)Cu(mu(1,1)-N-3)(2)Cu (2+) core and based on an organic ligand obtained from the solid state.* Inorganic Chemistry, 2007. **46**(21): p. 8843-8850.

166.	Roy, P., et al., *A copper(II) complex with rare mu(1,1,1)-azide ligand: Active catalyst for heterogeneous olefin epoxidation.* Inorganic Chemistry Communications, 2008. **11**(3): p. 265-269.

167.	Zhang, L., et al., *Ferromagnetic coupling in a one-dimensional molecular railroad copper(II) azido compound containing a defective double cubane motif.* Inorganic Chemistry, 2001. **40**(14): p. 3619-3622.

168.	Zhang, X.M., et al., *Syntheses and structures of metal tetrazole coordination polymers.* Dalton Transactions, 2006(26): p. 3170-3178.

169.	Zhao, J.P., et al., *Tuning the Structure and Magnetism of Azido-Mediated Cu-II Systems by Coligand Modifications.* Inorganic Chemistry, 2009. **48**(6): p. 2482-2489.

170.	He, Z., et al., *Coordination polymers with end-on azido and pyridine carboxylate N-oxide bridges displaying long-range magnetic ordering with low dimensional character.* Inorganic Chemistry, 2006. **45**(17): p. 6694-6705.

171. Liu, F.C., et al., *Novel heterometallic 3d-4f metal-azido complex of mixed ligands with unprecedented structure type: Synthesis, structure, and magnetic properties.* Inorganic Chemistry, 2006. **45**(16): p. 6129-6131.

172. Liu, F.C., et al., *An unusual 3-D asymmetric mixed valence copper-azido complex with pyrazinecarboxylate as co-ligand showing rare net topology: Hydrothermal synthesis, structure and magnetic properties.* Inorganic Chemistry Communications, 2007. **10**(2): p. 129-132.

173. Wang, Y.Q., et al., *Diverse Manganese(II) Coordination Polymers with Mixed Azide and Zwitterionic Dicarboxylate Ligands: Structure and Magnetic Properties.* Inorganic Chemistry, 2010. **49**(4): p. 1551-1560.

174. Zeng, Y.F., et al., *Structures with tunable strong ferromagnetic coupling: from unordered (1D) to ordered (discrete).* Chemistry-a European Journal, 2007. **13**(35): p. 9924-9930.

175. Graham, B., et al., *Syntheses, crystal structures, magnetic properties, and EPR spectra of tetranuclear copper(II) complexes featuring pairs of "Roof-Shaped" Cu2X2 dimers with hydroxide, methoxide and azide bridges.* Inorganic Chemistry, 2001. **40**(7): p. 1536-1543.

176. Mukherjee, P.S., et al., *The first structurally alternating copper(II) chain with alternate single end-on and end-to-end azido bridging: A synthesis, crystal structure, and low-temperature magnetic study.* Inorganic Chemistry, 2000. **39**(22): p. 5147-5150.

177.   Gao, E.Q., et al., *Structural and magnetic properties of three one-dimensional azido-bridged copper(II) and manganese(II) coordination polymers.* Inorganic Chemistry, 2003. **42**(25): p. 8456-8464.

178.   Wen, H.R., et al., *Syntheses, structure and properties of chiral copper(II) complexes with end-on azide bridge and chiral-bipyridine ligand.* Inorganica Chimica Acta, 2005. **358**(8): p. 2565-2570.

179.   Youngme, S., et al., *Copper(II) azide complexes of Cu(acac)(N-3)(dpyam) and Cu(mu-N-3-kappa(N1))(C2N3-kappa(N1))(dpyam) (2): Synthesis, crystal structure and magnetism.* Inorganic Chemistry Communications, 2007. **10**(7): p. 843-848.

180.   Hong, C.S., et al., *Unusual ferromagnetic couplings in single end-to-end azide-bridged cobalt(II) and nickel(II) chain systems.* Chemistry-a European Journal, 2001. **7**(19): p. 4243-4252.

181.   Liu, F.C., et al., *Two new copper azido polymorphs: Structures, magnetic properties, and effects of "Noninnocent" reagents in hydrothermal methods.* Inorganic Chemistry, 2007. **46**(19): p. 7698-7700.

182.   D ez, A.l., et al., *Structural and Luminescence Studies on π···π and Pt···Pt Interactions in Mixed Chloro-Isocyanide Cyclometalated Platinum(II) Complexes†.* Inorganic Chemistry, 2010. **49**(7): p. 3239-3251.

183.   Dong, L.N., et al., *3-D frameworks assembled by lanthanide dimers with 1,4-cyclohexanedicarboxylic acid and 1,10-phenanthroline via hydrogen bonds and -*

stacking interactions. Journal of Coordination Chemistry, 2010. **63**(12): p. 2088-2096.

184. Kostakis, G.E., et al., *Cu(N-3)(p-CPA) (n): a two dimensional network exhibiting spin reorientation.* Crystengcomm, 2009. **11**(10): p. 2084-2088.

185. Liu, F.C., et al., *Two Cobalt Compounds Based on Azide/Methoxy and Isonicotinate N-Oxide Ligands Exhibiting Ferromagnetic and Antiferromagnetic Interactions.* European Journal of Inorganic Chemistry, 2010(28): p. 4444-4449.

186. Liu, W., et al., *Structural and magnetic studies on cyano-bridged rectangular Fe2M2 (M = Cu, Ni) clusters.* Inorganic Chemistry, 2006. **45**(25): p. 10058-10065.

187. Zhao, J.P., et al., *One Pot Synthesis of Heterometallic 3d-3d Azide Coordination Architectures: Effect of the Single-Ion Anisotropy.* Inorganic Chemistry, 2010. **49**(24): p. 11325-11332.

188. Gu, Z.G., J.L. Zuo, and X.Z. You, *A three-dimensional ferromagnet based on linked copper-azido clusters.* Dalton Transactions, 2007(36): p. 4067-4072.

189. Zeng, Y.F., et al., *An azido-metal-isonicotinate complex showing long-range ordered ferromagnetic interaction: synthesis, structure and magnetic properties.* Chemical Communications, 2006(21): p. 2227-2229.

190. Zhao, J.P., et al., *Structure and magnetism of carboxylate/EO-azido-mixed-ligands bridged Cu-II systems.* Chinese Science Bulletin, 2009. **54**(23): p. 4303-4308.

191. Comarmond, J., et al., *DINUCLEAR COPPER(II) CRYPTATES OF MACROCYCLIC LIGANDS - SYNTHESIS, CRYSTAL-STRUCTURE, AND MAGNETIC-PROPERTIES - MECHANISM OF THE EXCHANGE INTERACTION THROUGH BRIDGING AZIDO LIGANDS.* Journal of the American Chemical Society, 1982. **104**(23): p. 6330-6340.

192. Escuer, A., et al., *Structure and magnetic behavior of a new 1-D compound with simultaneous end-on azido and carboxylato bridges. Unexpected strong ferromagnetic coupling for a Cu-N-Cu bond angle of 111.9 degrees as a consequence of ligand HOMOs countercomplementarity.* Inorganic Chemistry, 1997. **36**(6): p. 1233-1236.

193. Kahn, O., et al., *CRYSTAL-STRUCTURE AND MAGNETIC-PROPERTIES OF (MU-AZIDO) (MU-HYDROXO)BIS (N,N,N',N'-TETRAMETHYLETHYLENEDIAMINE)COPPER(II) PERCHLORATE, A COPPER(II) DINUCLEAR COMPLEX WITH A LARGE FERROMAGNETIC INTERACTION.* Inorganic Chemistry, 1983. **22**(20): p. 2877-2883.

194. Thompson, L.K., et al., *An azide-bridged copper(II) ferromagnetic chain compound exhibiting metamagnetic behavior.* Inorganic Chemistry, 1997. **36**(15): p. 3301-3306.

195. Myers, B.E., L. Berger, and Friedber.Sa, LOW-TEMPERATURE MAGNETIZATION OF CU(NO3)2.2.5H2O. Journal of Applied Physics, 1969. 40(3): p. 1149-&.